MODELING TIME-DEPENDENT RESPONSES OF PIEZOELECTRIC FIBER COMPOSITE

A Thesis

by

KUO-AN LI

Submitted to the Office of Graduate Studies of
Texas A&M University
in partial fulfillment of the requirements for the degree of

MASTER OF SCIENCE

December 2009

Major Subject: Mechanical Engineering

MODELING TIME-DEPENDENT RESPONSES OF PIEZOELECTRIC FIBER COMPOSITE

A Thesis

by

KUO-AN LI

Submitted to the Office of Graduate Studies of
Texas A&M University
in partial fulfillment of the requirements for the degree of

MASTER OF SCIENCE

Approved by:

Chair of Committee, Anastasia Muliana
Committee Members, Harry Hogan
Zoubedia Ounaies
Head of Department, Dennis O'Neal

December 2009

Major Subject: Mechanical Engineering

ABSTRACT

Modeling Time-Dependent Responses of Piezoelectric Fiber Composite.

(December 2009)

Kuo-An Li, B.E., National Taiwan University

Chair of Advisory Committee: Dr. Anastasia Muliana

The existence of polymer constituent in piezoelectric fiber composites (PFCs) could lead to significant viscoelastic behaviors, affecting overall performance of PFCs. High mechanical and electrical stimuli often generate significant amount of heat, increasing temperatures of the PFCs. At elevated temperatures, most materials, especially polymers show pronounced time-dependent behaviors. Predicting time-dependent responses of the PFCs becomes important to improve reliability in using PFCs. We study overall performance of PFCs having unidirectional piezoceramic fibers, such as PZT fibers, dispersed in viscoelastic polymer matrix. Two types of PFCs are studied, which are active fiber composites (AFCs) and macro fiber composites (MFCs). AFCs and MFCs consist of unidirectional PZT fibers dispersed in epoxy placed between two interdigitated electrode and kapton layers. The AFCs have a circular fiber cross-section while the MFCs have a square fiber cross-section. Finite element (FE) models of representative volume elements (RVEs) of active PFCs, having square and circular fiber cross-sections, are generated for composites with 20, 40, and 60% fiber contents. Two FE micromechanical models having one fiber embedded in epoxy matrix and five fibers placed in epoxy matrix are considered. A continuum 3D piezoelectric element in

ABAQUS FE is used. A general time-integral function is applied for the mechanical, electrical, and piezoelectric properties in order to incorporate the time-dependent effect and histories of loadings. The effective properties of PZT-5A/epoxy and PZT-7A/LaRC-SI piezocomposites determined from the FE micromechanical models are compared to available experimental data and analytical solutions in the literature. Furthermore, the effect of viscoelastic behaviors of the LaRC-SI matrix at an elevated temperature on the overall electro-mechanical and piezoelectric constants are examined.

ACKNOWLEDGEMENTS

I want to thank my advisor, Dr. Anastasia Muliana for her patience in teaching and guidance. I could not finish the thesis successfully without her suggestions and instructions. Next, I want to thank my girl friend, Yi-Ting Huang. With her careful checking and correcting my grammar and structure errors, I could complete my thesis faster and more correctly. Finally, I want to thank my parents. Without their support and encouragement, I could not finish my master degree in America.

TABLE OF CONTENTS

Page

Page

LIST OF FIGURES

Page

Page

Page

Page

Page

Page

LIST OF TABLES

Page

CHAPTER I
INTRODUCTION

Piezoelectric materials are being used as sensors and actuators due to their mechanical and electrical transforming ability. In 1880, Pierre and Jacques Curie published a paper on piezoelectric phenomena on a stressed crystal. They conducted experiments measuring surface charges of several stressed crystals, such as tourmaline, quartz, topaz, cane sugar and Rochelle salt. This study is believed to be the first record of piezoelectricity. In 1917, French physicist, Paul Langevin and his co-worker placed a quartz crystal based transducer, comprising of a quartz crystal sandwiched between two metals, on sonar. The quartz was used to convert the electric energy into vibration and generate ultrasonic wave for underwater sound transmission in submarine.

Between 1920 and 1940, piezoelectric based engineering components like microphones, accelerometer and ultrasonic transducers were developed. In these applications, the mechanical forces are converted into electrical potential. Performances of these piezoelectric devices were generally restricted by the limitation of the material properties, i.e., relatively low piezoelectric characteristics of the natural crystals. The piezoelectric properties of natural crystals are 0.01 to 0.1 times of those of the current piezoelectric ceramics like PZT. For example, the piezoelectric constant d of quartz is about 2.3 (10^{-12}C/V) and d_{333} of PZT-7A is 153 (10^{-12}C/V). Since the development of

---

This thesis follows the style of Composite Science and Technology.

ferroelectric materials, scientists discovered that ferroelectric materials have dielectric constants up to 100 times higher than the common crystals. After being polarized, these ferroelectric materials showed significant improvements in piezoelectric properties.

There are several types of piezoelectric materials including natural materials and man-made materials. Natural crystals are berlinite ($AlPO_4$), can sugar, quartz, topaz and tourmaline-group minerals. Examples of man-made crystals: gallium orthophosphate ($GaPO_4$) and Langasite ($La_3Ga_5SiO_{14}$). Man-made ceramics are barium titanate ($BaTiO_3$), lead titanate ($PbTiO_3$), lead zirconate titanate ($Pb[Zr_xTi_{1-x}]O_3$ $0<x<1$), potassium niobate ($KNbO_3$), lithium niobate ($LiNbO_3$), lithium tantalite ($LiTaO_3$), and many others. There are some lead-free piezoceramics such as sodium potassium niobate (KNN) and bismuth ferrite ($BiFeO_3$). Moreover, some polymers such as polyvinylidene fluoride (PVDF) and polyimide are also piezoelectric materials. The piezoelectric constant *d* of PVDF varies between 1.5 to 32pC/N, which is much smaller than those of piezoelectric ceramics and the stiffness of PVDF is generally small, making it rather daunting for providing large actuation. PVDF is often used as sensor in smart composite. [1]

The widely used piezoelectric ceramics are lead zirconate titanate (PZT), lead titanate (PT) and barium titanate (BT). The electro-mechanical properties of PZT, PT, and BT are given in Table 1.1. PZT has relatively high compliance and high piezoelectric properties, making them suitable as actuators.

Table 1.1 Properties of Piezoelectric ceramics(Morgan Ceramics Co.)

	PZT(PZT701)	PT(PT1)	BT(BT301)
Relative Permittivity $\varepsilon_{r\ 33}^{T}/\varepsilon_o$	425	210	1140
Piezoelectric Constant $d_{333}\times10^{-9}$C/V	153	68	127
Compliance $S^{E}_{3333}\times10^{-12}$m^2/N	13.9	8.6	8.1
Curie Temperature ℃	350	255	130

Traditional piezoelectric ceramics are brittle and easy to break during handling and service. Piezoelectric Fiber Composite (PFC) was developed to improve the fault of piezoelectric ceramics. It is formed by combining piezoelectric ceramic fibers and epoxy matrix sandwiched between two electrode layers. PFC has the following features [2]:

1. They have high stiffness and large bandwidth, making it possible to use a wide range of signals in actuator applications.

2. They have better strength and conformability than PZTs, creating more flexible and pliable structure and improving resistant to brittle damage.

3. They can be integrated into laminated composite structures or other host structures and used for health monitoring, energy harvesting, and controlling shape changes.

This study investigates coupled electro-mechanical and time dependent behaviors of two kinds of PFCs, active fiber composite (AFC) and macro fiber composite (MFC).

Active fiber composite (AFC) was developed by Bent and Hagood[2] at Massachusetts Institute of Technology and macro fiber composite (MFC) was developed at NASA Langley Research Center. These two active composites do not have significant differences in their overall structures, but only in the types and shapes of the fibers. The AFC uses fibers with a circular cross-section and MFC has fiber with a rectangular cross-section. The overall performance of the PFC is driven by the behaviors and microstructural arrangements of the constituents. The use of polymer matrix constituents, while known for their viscoelastic behavior, could result in the overall time-dependent behaviors of the PFC. Time-dependent effect is even more significant at elevated temperatures and high stress levels. This study deals with understanding coupled electro-mechanical and viscoelastic effects, of the PZT fibers and epoxy polymer, on the effective properties of AFC and MFC. Finite element (FE) method is used to generate simplified microstructures of AFC and MFC. The simplified microstructures consist of unidirectional fibers embedded in epoxy polymers and the existence of electrode layers is neglected. It is assumed that electric fields continuously flow along the axial fiber direction. The overall electro-mechanical responses obtained using the FE models are compared to experimental data and analytical solutions available in the literature. This chapter presents literature studies on the performance of AFC and MFC and micromechanical modeling approaches of piezoelectric composites. The second part of this chapter discusses research objectives.

1.1 STATE OF THE ART KNOWLEDGE IN UNDERSTANDING PERFORMANCE OF PIEZOCOMPOSITES AND THEIR APPLICATIONS

1.1.1 ACTIVE FIBER COMPOSITE

In order to improve performance of sensor and actuator for aerospace applications, Bent and Hagood [2] developed an active fiber composite (AFC) which was composed of piezoelectric fibers, epoxy matrix and interdigital electrodes (IDE). The AFC overcomes some disadvantages of the traditional PZT wafer. AFC inherits high stiffness and wide bandwidth of the PZT. Traditional piezoelectric ceramics have high stiffness but have low robustness to brittle damage. AFC prevents catastrophic failure due to fiber breakage as the epoxy can still transfer some of the load when the fiber breaks. Moreover, AFC enhances performance of actuator since it is flexible and can undergo large out of plane deformation. Nelson et al. [3] measured electrical and mechanical properties of 1-3 piezo composites at different fiber volume fractions and compared these experimental measurements to analytical solutions. They also compared properties of several piezoelectric fibers manufactured by Extrusion, Sol-Gel, Viscous Plastic Processing (VPP) and Viscous Suspension Spinning Process (VSSP). They found that the fibers produced by the VPP have the highest piezoelectric constants and dielectric constants than the ones obtained from other manufacturing processes. Wickramasinghe and Hagood [4] used AFC as an actuator system on Boeing active material rotor (AMR) blade, a helicopter blade application. The AFC system was integrated into the blade laminate forming an integrated structure and control unit. In order to integrate the AFC and AMR successfully, they conducted nominal actuation performance tests which measure longitudinal and transverse actuation strains of AFC integrated to E-Glass

woven fabric (E120) laminated systems. They also measured performance of the AFC itself. Different ranges of excitation voltages were applied to determine the optimum voltage cycle to be used in the AMR blade. They also conducted stress-strain tests and monitored the actuation performance under tensile loads on the AFC and AMR integrated systems. The average nominal actuation strain measured on the actuators was 1200 με at 1 Hz for 3000 Vpp with 0 Vdc, the optimum voltage cycle selected for the blade operation. The undamaged AFC longitudinal and transverse moduli were 39.1 and 14.5 GPa. The tested AFC recovered approximately 100%, 90%, 80% of actuation after completely unloading from 2000, 4000 and 6000με load levels. These test data help install the AFC actuator system on the AMR optimally. Wickramasinghe and Hagood [5] used the AFC actuator system on the AMR blade and performed long-term durability characterization tests. The tests included electrical and mechanical fatigue tests to examine the durability of the AFC actuator system. The results showed no degradation in strains up to 20 million cycles of the electrical fatigue test. The microscopic inspection showed that the electrode fingers burned under the test, but none of these burns were large enough to cause electrical failure. The mechanical fatigue test showed no significant deterioration in the modulus or actuation capability up to 10 million cycles. The actuator that is used in the AMR blade retained the stiffness and performance properties. It even retained its stiffness properties and actuation performance after 10 million cycles at a load level that is 50% higher than the original fatigue load level. Melnykowycz et al. [6] used two sizes of AFCs to perform several mechanical tests. The long type of AFC is 150 mm × 20 mm, and the short type is 33 mm × 40 mm. The long AFC was used for tensile test. The short AFC was integrated with glass fiber

reinforced plastic (GFRP) laminate and used for the mechanical oscillation test, surface bonded fragmentation test and Acoustic emission (AE) monitoring. The results showed that the average stress at failure was 47 MPa and Young's modulus was 29 GPa. They also showed that the performance of AFC sensor was linear and stable up to a strain of 0.2%. A degradation behavior was seen between 0.2% and 0.4% strain and was attributed to the fragmentation in the PZT fibers, which saturated beyond 0.45% strain. The AE monitoring technique detected damage in the laminates during testing and found that the damage was due to micro-crack.

1.1.2 MACRO FIBER COMPOSITE

Macro Fiber Composites (MFCs) were established by NASA Langley Research Center. While fibers in the AFCs have a circular cross-section, MFCs have a rectangular fiber cross-section, which make manufacturing of MFC easier than the AFC. In addition, MFC results in larger fiber volume contents than the AFC. The maximum fiber volume content of AFC is less than 0.785 because of the restriction in the fiber geometry. The fiber volume content of MFC could reach up to 0.824 [7]. High fiber volume content enhances the performance of the composite and improves the stiffness and strength of the composites. Azzouz et al. [8] used MIN6 element to establish a FE model for piezoelectric fiber actuators. MIN6 is a three-node shell element. They modeled the MFC bonded to rectangular and triangular cantilever beams and compared the results with the ones having traditional PZT-5A actuator. The twisting amplitudes of the MFC were better than that of PZT-5A actuator. Sodano [9] used a MFC as self-sensing actuator. He

designed a circuit to sense and control vibration in an aluminum beam. The results showed that the MFC actuator successfully suppressed 90% vibration of the aluminum beam. Moreover, he used multiple MFCs as sensors and actuators on an inflatable structure to control the vibration in the structure. He took an inflated torus as inflatable structure and put 4 MFCs on four sides as sensors and actuators. The inflatable structure was disturbed. The results showed that MFC was effective in attenuating the vibration in the first mode of vibration but ineffective for the second mode of vibration due to the location of sensors and actuators. Finally, he tested the electrical converting ability of MFC and designed a power harvesting device. The results showed that the MFC produced lower current than PZT and was not suitable to charge the battery.

Williams et al. [7] derived non-linear models for coefficient of thermal expansion (CTE) of MFC. Temperature dependent CTE of each constituent in the MFC, i.e., Kapton, acrylic, copper, epoxy and PZT, was incorporated. They used ANSYS to establish a quarter unit cell FE model of an MFC actuator. The predictions of the effective CTE obtained from the theoretical results were compared to the FE modeling results. Williams et al. [10] measured four independent linear elastic engineering constants E1, E2, v12 and G12 of the orthotropic MFC actuator. They used non-linear constitutive relations including Elastic-linear hardening, Ramberg-Osgood, Quadratic Least-Squares methods to fit the experimental data. Williams et al. [11] derived a non-linear constitutive model from the Gibbs thermodynamic potential function for a piezoelectric continuum. They applied the non-linear model for MFC and measured the piezoelectric coefficient of MFC under mechanical and electrical loadings. The studied electrical loading is illustrated in Fig. 1.1. The DC offset voltage means the sinusoidal

signal offset from zero. Figure 1.1 illustrates 0 VDC offset, 250 VDC offset and 500 VDC offset input. They found that the absolute values of d_{31} and d_{33} increase under higher DC offset voltage and the strain-field behaviors of the MFC become more linear under higher DC offset voltages. The induced DC offset strains were nearly a linear function of DC biasing voltage.

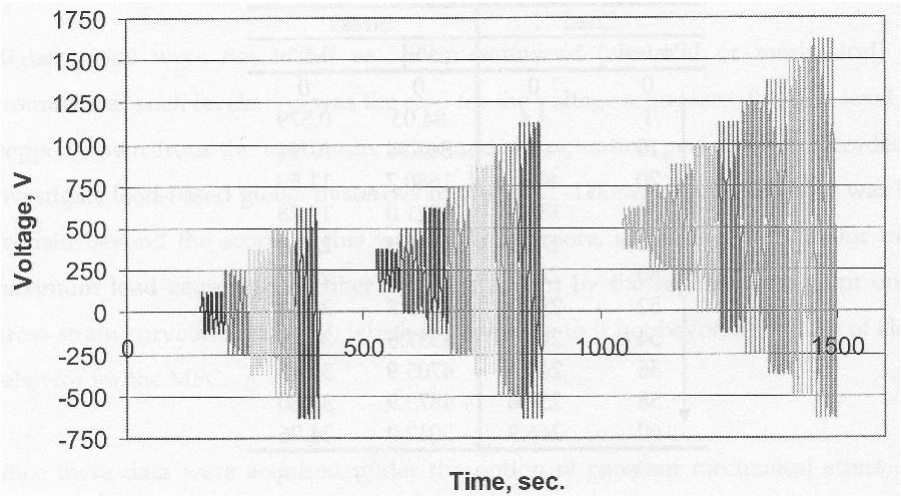

Fig. 1.1 Sinusoidal loading

Dano and Julliere [12] investigated behaviors of a smart cantilever beam having two MFC actuators which were used to control deformations due to temperature changes. They developed a FE model of the system and subjected the beam to a thermal stimulus. They applied electrical field to the MFC actuator in the FE model to compensate the deflection. The input value from the given function was $E^{(k)} = E^{(k-1)} + G * \Delta U_z^{(k-1)}$, where E is the electrical field, G is the control gain parameter and ΔU is the incremental displacement. The model successfully compensated the deformation. They also

conducted experiment to verify their model. They used a PID (proportional, integral, derivative) feedback controller to actively control the deformation. The measured voltage is 13% higher than the voltage predicted by the numerical simulation. Dano et al. [13] established FE models of two active beams. The first beam was a cantilever plate with one MFC actuator, and the other was a cantilever plate with two MFC actuators. They tested the two cantilever beams in an environmental chamber subject to temperature changes and the thermal deflections were monitored. They applied an electrical field to the actuator to control the deflection. Finally, they compared the experimental data to the FE results. The FE model can accurately predict the thermal deflections and the MFC compensations.

1.1.3 MICROMECHANICAL MODELS

Micromechanical models enable us to integrate different material properties of constituents to predict effective responses of composites. This study classifies the micromechanical models into two categories. The first category uses simplified microstructures of composites to obtain the effective behaviors. The composites are treated as a fictitiously homogeneous body and an assumption on simple (unit-cell) microstructures is made to reduce complexity in analyzing overall responses of composites. The second category generates detailed microstructures of composites, which can include variations and nonuniformities in constituents and geometries of the microstructures. FE method is commonly used to create microstructural details of composites and boundary value problems (BVP) are solved on the selected

heterogeneous microstructures of composites. This approach allows determining local field variables, but increases complexity and computational cost.

Dunn and Taya [14] compared four micromechanical models based on simplified microstructural geometries: the dilute distribution, self-consistent, Mori-Tanaka and differential models to predict linear piezoelectric constants for several piezoelectric composites with different volume fractions. They compared the numerical results to experimental data available in the literature. The results showed that the dilute distribution model over-predicts the e_{311} values when the PZT fiber content is higher than 0.1. The self-consistent method could not simulate effective properties over an entire range of volume fractions when the elastic and piezoelectric moduli of the reinforcing phase vanish. The Mori-Tanaka model coincides with the upper and lower bounds for the uncoupled electro-mechanical behavior of composites reinforced with ellipsoidal inclusions. Tan and Tong [15] established a rectangle model (R model) and a rectangle-cylinder model (RCR model) for piezoelectric-fiber-reinforced composites to predict mechanical and piezoelectric properties of composites at several fiber volume contents. They compared the predictions of the effective properties to the ones obtained from the FE model of detailed composite microstructures and existing experimental data. Odegard [16] established a homogenization model to calculate overall properties of four piezoelectric composites: graphite/PVDF fiber composite, SiC/PVDF particulate composite, PZT-7A/LaRC-SI fiber composite, and PZT-7A/LaRC-SI particulate composite. Responses generated from this micromodel are compared to the results of the Mori-Tanaka, self-consistent and FE models of the unit cells of the composites. The results showed that the proposed micromechanical model gives better predictions than the

Mori-Tanaka and self-consistent models at 90% volume fraction for the E_{11} and E_{22} in PZT-7A/ LaRC-SI fiber composite. The proposed model also showed better predictions for the E_{11}, E_{22} and E_{33}, at 60 % volume fraction for e_{15}, $e_{31}=e_{32,}$ $\kappa_1/\kappa_o=\kappa_2/\kappa_{o,}$ and above 40% volume fraction for $e_{31}=e_{32}$ in PZT-7A / LaRC-SI particle composite.

Lee et al. [17] established a micromechanical model based on a representative volume element to simulate two-phase and three-phase electro-magneto-elastic composites. The two-phase model contains piezomagnetic matrix with a piezoelectric fiber. The three-phase model contains piezoelectric fiber, piezomagnetic fiber and epoxy matrix. They implemented their model by using FE method and compared the FE results with the ones from the Mori-Tanaka method. The results showed that the FE data are well matched with the Mori-Tanaka prediction for the effective stiffness, piezoelectric constants, dielectric permeability, piezomagnetic constants, magnetic permeability and magnetoelectric constants. Aboudi [18] used a high fidelity asymptotic homogenization approach with nonlinear constitutive relations for ferroelectric composites and implemented it for piezoelectric fiber composites. He examined the hysteresis behavior of piezoelectric fiber composites. The nonlinear hysteresis behavior is strongly dependent on the applied electric field and mechanical stress. Lin and Sodano [19] suggested a new piezoelectric composite called active structure fiber (ASF). The ASF structure consisted of a circular carbon fiber as the core covered by layers of piezoelectric material and electrode. They established a theoretical model to predict the piezoelectric constant d_{31} of the ASF and used FE method to implement it. The result showed that the piezoelectric coupling coefficients of the ASF could reach up to 65-70% of the piezoelectric ceramics as the ratio of the piezoelectric material thickness(t) to the fiber radius(r_o) reaches 0.85.

Therefore, the material is good for damping, power harvesting, and structural health monitoring. Dunn and Wienecke [20] used Eshelby's method to analyze responses of piezoelectric materials having inclusions and inhomogeneitites. The closed-form expressions were formulated using four Eshelby tensors for spherical inclusions in transversely isotropic piezoelectric materials.

Liu et al. [21] developed a micromechanical model to study the interaction between fiber deformations, pull-out stress and corresponding electrical field for AFC. The model consists of a single fiber surrounded by matrix. One part of the fiber was not bonded to the matrix and the other part was bonded to the matrix called a bridging area. The bridging fiber experienced elastic deformation, debonding from the surround matrix, and frictional pull out crack growth, which is called "fiber pull-out." The result showed that both pull-out stress and electrical field changed with the pull-out displacement. Moreover, changes in the electric field can influence the pull-out stress and fiber displacement. From this study, they concluded the possibility to monitor and control the fracture behaviors electrically. Beckert and Kreher [22] established two micromechanical models for analyzing bulk film Interdigitaded Electrode (IDE)-actuator and composite IDE-actuator. For the bulk film, the FE model consists of 2D IDE containing electrode, isolator coating, and piezoelectric materials. For the composite model, they generated FE having 3D IDE containing isolator coating, electrode layer, dielectric interlayer, polymer matrix, homogenized composite layer and piezo-fiber. The results suggested that for a piezoelectric layer with thickness of 200μm, the electrode width should be 300μm and the space between the electrodes should be 1000μm. The results also suggested that reducing the thickness of the dielectric interlayer or enhancing the dielectric constant of

the layer can improve the overall performance. Nelson et al. [3] used a representative volume element (RVE) model generated using FE to study responses of an IDE on a bulk PZT substrate. The model was used to optimize the IDE design. They observed that an optimal actuation occurred at electrode widths equal to half of the substrate thickness. For thin substrates, the electrode spacing can be reduced to enable lower driving voltages.

1.2 RESEARCH OBJECTIVE

This study investigates the effects of fiber geometries and constituent's properties on the overall electro-mechanical performance of piezoelectric fiber composites (PFC) which is composed of unidirectional PZT fibers and epoxy matrix. FE models are used to generate simplified microstructures of PFC. One fiber and five fiber micromechanical models are considered for the PFCs. Two kinds of PFCs are studied, which are AFC and MFC. AFC has a circular fiber while MFC has a square fiber. The effects of viscoelastic behaviors of the polymer matrix which is pronounced at elevated temperatures on the overall electro-mechanical response of composites are also examined. Responses of PFC are compared to theoretical and experimental data available in the literature. This thesis consists of the following major components:

Chapter II presents a general constitutive material model of piezoelectric materials that include time-dependent effect. Gibbs energy functions were used to derive coupled electro-mechanical relations with several independent field variables. A general time-integral function is applied for the mechanical, electrical, and piezoelectric relations. Parametric studies on the effects of applied field variables, i.e., stress and electric field,

on the overall time-dependent behavior are presented.

Chapter III presents micromechanical models using FE for AFC and MFC at three different fiber volume contents. Micromechanical models with a single fiber and five fibers dispersed in epoxy matrix are generated. The effective material properties obtained from the FE micromodels are compared to the analytical solutions and experimental data available in the literatures. Furthermore, we investigate the effect of the viscoelastic behavior of polymer matrix, i.e., LaRC-SI, at high temperature on the overall electro-mechanical properties of AFC and MFC. PZT fibers are considered for the AFC and MFC. Due to limited experimental data available for PZT properties at high temperatures, we made two assumptions during the modeling. First, only certain PZT properties that are available in the literature vary with temperatures while other PZT properties are kept constant at room temperature. Second, all PZT properties vary with temperatures following the available data. Finally, the effect of time-dependent piezoelectric constants of PZT combined with viscoelastic matrix on the long-term electro-mechanical responses of AFC and MFC is examined.

Chapter IV presents conclusion and future work.

CHAPTER II
LINEARIZED PIEZOELECTRIC RESPONSES WITH A TIME-DEPENDENT EFFECT

PFC is a smart composite combining piezoelectric ceramics fibers and epoxy matrix. At room temperature, piezoelectric ceramics show mild time-dependent mechanical responses, while at high temperatures ceramics would experience significant creep. Heiling and Hardtl [23] showed that surface charges of piezoelectric ceramics under constant stress increase with time. Dielectric properties of most materials including piezoelectric ceramics are dependent on frequency and loading rates. Moreover, epoxy matrix has significant viscoelastic characteristics. Thus, overall electro-mechanical responses of PFCs can exhibit time-dependent behaviors, which become more pronounced at elevated temperatures.

In this chapter, we examine time-dependent responses of piezoelectric materials. The first section of this chapter presents a general constitutive material model of linear piezoelectric materials under a constant temperature. The second section presents a general time-dependent relation for coupled electro-mechanical responses. Time-dependent responses of piezoelectric materials subject to various loading histories are then examined, which are discussed in section 2.3.

2.1 GENERAL PIEZOELECTRIC EQUATIONS

A general constitutive model for linear piezoelectric materials has been formulated, e.g., Damjanovic [24], Lines and Glass [25]. The constitutive model is derived by satisfying conservation of energy and balance of linear and angular momentum. The energy equation is described as in Eq. (2.1). Where G is the Gibbs free energy, U is the internal energy, T is the temperature and S is the entropy. The variable σ_{ij} is the scalar component of the stress tensor, ε_{ij} is the scalar component of the strain tensor, E_i is the scalar component of the electric field and D_i is the scalar component of the electrical displacement.

$$G = U - TS - \sigma_{ij}\varepsilon_{ij} - E_i D_i \tag{2.1}$$

Differentiating Eq. (2.1) with respect to each independent variable, we obtain relations in Eq. (2.2).

$$dG = dU - TdS - SdT - \sigma_{ij}d\varepsilon_{ij} - \varepsilon_{ij}d\sigma_{ij} - E_i dD_i - D_i\, dE_i \tag{2.2}$$

From the first law of thermodynamics, the change of the internal energy dU can be converted into heat dQ and work dW. The heat change dQ is equal to TdS. In piezoelectric material, the work done on a system is described by the mechanical work $\sigma_{ij}d\varepsilon_{ij}$ and electrical energy $E_i dD_i$. The change of the internal energy is written as:

$$dU = TdS + \sigma_{ij}d\varepsilon_{ij} + E_i dD_i \tag{2.3}$$

Substituting dU in Eq. (2.3) into Eq. (2.2) gives:

$$dG = -SdT - \varepsilon_{ij}d\sigma_{ij} - D_i\, dE_i \tag{2.4}$$

In this study, we focus on responses of materials under a constant temperature, which eliminates the temperature change dT. We can rewrite Eq. (2.4) as:

$$dG = -\varepsilon_{ij} d\sigma_{ij} - D_i \, dE_i \tag{2.5}$$

By taking σ_{ij} and E_i as independent variables, strain and electric displacement are expressed as:

$$\varepsilon_{ij} = -\left(\frac{\partial G}{\partial \sigma_{ij}}\right)_E \tag{2.6}$$

$$D_i = -\left(\frac{\partial G}{\partial E_i}\right)_\sigma \tag{2.7}$$

The strain ε_{ij} is equal to the partial derivation of the Gibbs free energy w. r. t. the stress σ_{ij} at a constant electrical field **E** and the electrical displacement D_i is determined by differentiating the Gibbs free energy w. r. t. the electrical field E_i at a constant stress **σ**.

$$d\varepsilon_{ij} = \left(\frac{\partial \varepsilon_{ij}}{\partial \sigma_{kl}}\right)_E \partial \sigma_{kl} + \left(\frac{\partial \varepsilon_{ij}}{\partial E_k}\right)_\sigma \partial E_k \tag{2.8}$$

$$dD_i = \left(\frac{\partial D_i}{\partial \sigma_{jk}}\right)_E \partial \sigma_{jk} + \left(\frac{\partial D_i}{\partial E_j}\right)_\sigma \partial E_j \tag{2.9}$$

Equations (2.8) and (2.9) represent total derivative of the strain and electrical displacement fields. The coefficients of Eq. (2.8) and Eq. (2.9) are the first derivative functions under a constant electrical field or a constant stress. The electro-mechanical properties are defined as:

$$\left(\frac{\partial \varepsilon_{ij}}{\partial \sigma_{kl}}\right)_E = S^E_{ijkl} \tag{2.10}$$

$$\left(\frac{\partial \varepsilon_{ij}}{\partial E_k}\right)_{\sigma} = \left(\frac{\partial D_i}{\partial \sigma_{jk}}\right)_{E} = d_{ijk} \tag{2.11}$$

$$\left(\frac{\partial D_i}{\partial E_j}\right)_{\sigma} = \kappa_{ij}^{\sigma} \tag{2.12}$$

Where S_{ijkl}^{E} is the scalar component of the elastic compliance, which relates a mechanical stress to strain under a constant electrical field; d_{ijk} is the scalar component of the piezoelectric constant that measures the amount of strain generated by an applied electric field at zero (constant) stress or the amount of electric displacement due to an applied stress at zero (constant) electric field; κ_{ij}^{σ} is the scalar component of the dielectric permittivity, which relates an electric field to an electric displacement under zero (constant) stress.

For a linearized piezoelectric relation, the above material parameters are constant, which are independent on field variables. Figure 2.1 illustrates a linear modulus as compared to a nonlinear (stress or strain dependent) modulus. Linearized piezoelectric relation gives reasonable predictions of electro-mechanical responses when prescribed loadings are sufficiently small.

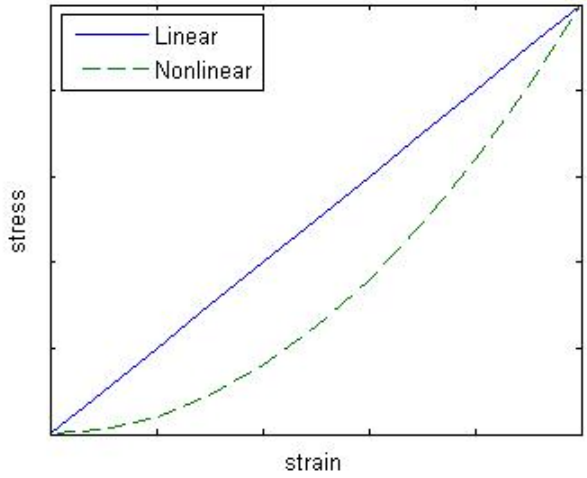

Fig. 2.1 Linear and nonlinear modulus

Substituting the material parameters in Eqs. (2.10)-(2.12) into Eq. (2.8) and Eq. (2.9), the linearized piezoelectric constitutive models are written as:

$$\varepsilon_{ij} = S^{E}_{ijkl}\sigma_{kl} + d_{kij}E_k \tag{2.13}$$

$$D_i = d_{ijk}\sigma_{jk} + \kappa^{\sigma}_{ij}E_j \tag{2.14}$$

Different constitutive relations can be obtained by choosing different independent variables as discussed in Damjanovic [24]. The relations are listed in Eq. (2.15) to Eq. (2.20).

$$\sigma_{ij} = C^{E}_{ijkl}\varepsilon_{kl} - e_{kij}E_k \tag{2.15}$$

$$D_i = e_{ijk}\varepsilon_{jk} + \kappa^{\varepsilon}_{ij}E_j \tag{2.16}$$

$$\varepsilon_{ij} = S^{D}_{ijkl}\sigma_{kl} + g_{kij}D_k \tag{2.17}$$

$$E_i = -g_{ijk}\sigma_{jk} + \beta^{\sigma}_{ij}D_j \tag{2.18}$$

$$\sigma_{ij} = C_{ijkl}^{D}\varepsilon_{kl} - h_{kij}D_k \tag{2.19}$$

$$E_i = -h_{ijk}\varepsilon_k + \beta_{ij}^{\varepsilon}D_j \tag{2.20}$$

Where C_{ijkl}^{E} is the scalar component of the elastic stiffness under a constant electrical field. Variables e_{ijk}, g_{ijk} and h_{ijk} are the scalar components of the piezoelectric constants; $\kappa_{ij}^{\varepsilon}$ is the scalar component of the dielectric permittivity under a constant strain; S_{ijkl}^{D} is scalar component of the compliance under a constant electrical displacement; β_{ij}^{σ} is the inverse of dielectric susceptibility under a constant stress; C_{ijkl}^{D} is the scalar component of the elastic stiffness under a constant electrical displacement; β_{ij}^{ε} is the inverse of dielectric susceptibility under a constant strain. The relations among these material constants are summarized as follows:

$$C_{ijkl}^{E} = \left(\frac{\partial\sigma_{ij}}{\partial\varepsilon_{kl}}\right)_{E} \tag{2.21}$$

$$e_{ijk} = \left(\frac{\partial D_i}{\partial\varepsilon_{jk}}\right)_{E} = -\left(\frac{\partial\sigma_{ij}}{\partial E_k}\right)_{\varepsilon} \tag{2.22}$$

$$\kappa_{ij}^{\varepsilon} = \left(\frac{\partial D_i}{\partial E_j}\right)_{\varepsilon} \tag{2.23}$$

$$S_{ijkl}^{D} = \left(\frac{\partial\varepsilon_{ij}}{\partial\sigma_{kl}}\right)_{D} \tag{2.24}$$

$$g_{ijk} = \left(\frac{\partial\varepsilon_{ij}}{\partial D_k}\right)_{\sigma} = -\left(\frac{\partial E_i}{\partial\sigma_{jk}}\right)_{D} \tag{2.25}$$

$$\beta_{ij}^{\sigma} = \left(\frac{\partial E_i}{\partial D_j}\right)_{\sigma} \tag{2.26}$$

$$C_{ijkl}^{D} = \left(\frac{\partial\sigma_{ij}}{\partial\varepsilon_{kl}}\right)_{D} \tag{2.27}$$

$$h_{ijk} = \left(\frac{\partial E_i}{\partial \varepsilon_{jk}}\right)_D = -\left(\frac{\partial \sigma_{ij}}{\partial D_k}\right)_\varepsilon \tag{2.28}$$

$$\beta_{ij}^{\varepsilon} = \left(\frac{\partial E_i}{\partial D_j}\right)_\varepsilon \tag{2.29}$$

The mutual relations among all piezoelectric constants are shown in Eq. (2.30) to Eq. (2.33).

$$d_{kij} = e_{kmn} S_{mnij}^{E} = \kappa_{km}^{\sigma} g_{mij} \tag{2.30}$$

$$e_{kij} = d_{kmn} C_{mnij}^{E} = \kappa_{km}^{\varepsilon} h_{mij} \tag{2.31}$$

$$g_{kij} = h_{kmn} S_{mnij}^{D} = \beta_{km}^{\sigma} d_{mij} \tag{2.32}$$

$$h_{kij} = g_{kmn} C_{mnij}^{D} = \beta_{km}^{\varepsilon} e_{mij} \tag{2.33}$$

There are coupling between the properties determined at constant ε or σ and at constant D or E. Different loading conditions can result in different stiffness, compliance and dielectric constants of piezoelectric materials. For example, in absence of the mechanical strain, stress in Eq. 2.15 is written as:

$$\sigma_{ij} = -e_{kij} E_k \tag{2.34}$$

Substituting Eq. (2.31) into Eq. (2.34), the stress is given as:

$$\sigma_{ij} = -d_{kmn} C_{mnij}^{E} E_k \tag{2.35}$$

Using σ_{ij} in Eq. (2.35), the electric displacement in Eq. 2.14 is rewritten as:

$$D_i = -d_{ipq} d_{jmn} C_{mnpq}^{E} E_j + \kappa_{ij}^{\sigma} E_j \tag{2.36}$$

Furthermore, in absence of the mechanical strain, the electric displacement in Eq. 2.16 is given as:

$$D_i = \kappa_{ij}^{\varepsilon} E_j \tag{2.37}$$

Comparing the electric displacement in Eq. 2.36 and 2.37, we obtain the following relation:

$$\kappa_{ij}^{\varepsilon} E_j = -d_{ipq} d_{jmn} C_{mnpq}^{E} E_j + \kappa_{ij}^{\sigma} E_j = \left(\kappa_{ij}^{\sigma} - d_{ipq} d_{jmn} C_{mnpq}^{E}\right) E_j \tag{2.38}$$

Thus, the relation between the dielectric constants determined at zero (constant) strain to the one at zero (constant) stress is given as:

$$\kappa_{ij}^{\varepsilon} = \kappa_{ij}^{\sigma} - d_{ipq} d_{jmn} C_{mnpq}^{E} = \kappa_{ij}^{\sigma} \left(1 - \frac{d_{ipq} d_{jmn} C_{mnpq}^{E}}{\kappa_{ij}^{\sigma}}\right) = \kappa_{ij}^{\sigma} (1 - k^2) \tag{2.39}$$

where k is the coupling coefficient.

Following the similar procedure as above, we also can relate S_{mnjk}^{E} to S_{mnjk}^{D}, which is given as:

$$S_{mnpq}^{D} = S_{mnpq}^{E} \left(1 - \frac{d_{ipq} d_{jmn} C_{mnpq}^{E}}{\kappa_{ij}^{\sigma}}\right) = S_{mnpq}^{E} (1 - k^2) \tag{2.40}$$

The coupling coefficient is given as:

$$k^2 = \frac{d_{ipq} d_{jmn}}{\kappa_{ij}^{\sigma}} \; C_{mnpq}^{E} \tag{2.41}$$

2.2 TIME-DEPENDENT PIEZOELECTRIC EQUATIONS

Responses of viscoelestic materials depend not only on the current loadings, but also histories of loadings. Examples of viscoelastic phenomena are creep and relaxation. Creep is increase in the deformation of materials under a constant stress. Relaxation is when a material is subject to a constant strain, the stress continuously decreases with time.

This section adopts and extends the concept of linear viscoelastic materials for determining time-dependent responses of linear piezoelectric materials. There are several common linear viscoelastic material models, such as the Maxwell, Kelvin-Voigt (KV) and Standard Linear Solid (SLS) models. Spring-dashpot mechanical analogs are commonly used to describe behaviors of the above viscoelastic models.

The mechanical analogy of the Maxwell model is shown in Fig. 2.2. It is a spring and a dashpot arranged in series. Suppose F(t) is the applied uniaxial force, Y is the spring constant, μ is the dashpot constant, $\Delta_S(t)$ is the elongation of the spring, $\Delta_D(t)$ is the elongation of the dashpot, and $\Delta(t)$ is the total elongation due to the applied force. Satisfying compatibility and equilibrium relations and using constitutive models for the spring and dashpot lead to:

$$\Delta(t) = \Delta_S(t) + \Delta_D(t) \tag{2.42}$$

$$F(t) = E\Delta_S(t) \tag{2.43}$$

$$F(t) = \mu\dot{\Delta}_D(t) = \mu\frac{d}{dt}\Delta_D(t) \tag{2.44}$$

Taking time derivative of Eq. (2.42) gives

$$\dot{\Delta}(t) = \dot{\Delta}_S(t) + \dot{\Delta}_D(t) \tag{2.45}$$

Substituting the constitutive models for the spring and dashpot to Eq. 2.45 leads to

$$\frac{\dot{F}}{Y} + \frac{F}{\mu} = \dot{\Delta}_S(t) + \dot{\Delta}_D(t) = \dot{\Delta}(t) \tag{2.46}$$

Associating the elongation $\Delta(t)$ to the strain ε(t) and the force F(t) to the stress σ(t), we obtain the governing equation for the Maxwell model.

$$\dot{\varepsilon} = \frac{\dot{\sigma}}{Y} + \frac{\sigma}{\mu} \tag{2.47}$$

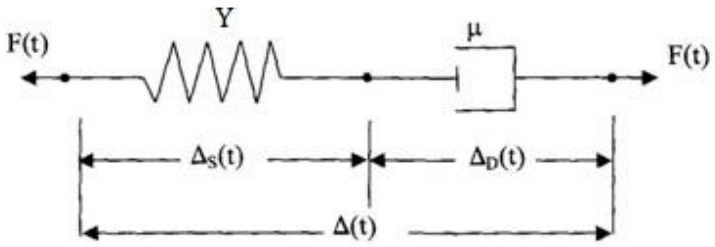

Fig. 2.2 Maxwell model[26]

When a constant strain is applied, the solution to the governing equation in Eq. (2.47) gives a relaxation modulus Y(t) in Eq. (2.48); where τ_R is called the relaxation time. When a constant stress is prescribed, we obtain a creep compliance J(t) in Eq. (2.49). The relaxation stress and creep strain for the Maxwell model are illustrated in Fig. 2.3 and Fig. 2.4, respectively.

$$Y(t) = Ye^{-\left(\frac{Y}{\mu}\right)t} = Ye^{-\frac{t}{\tau_R}} \tag{2.48}$$

$$J(t) = \frac{1}{Y}\left(1 + \frac{t}{\mu}\right) \tag{2.49}$$

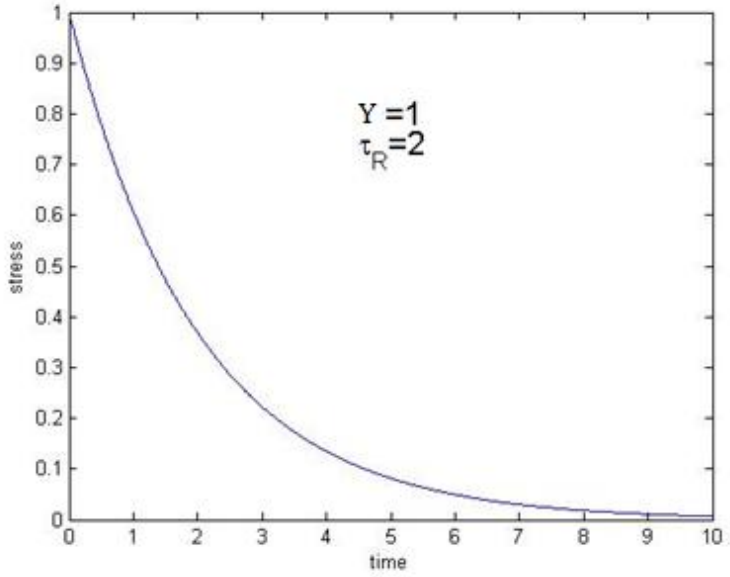

Fig. 2.3 Relaxation stress of the Maxwell model

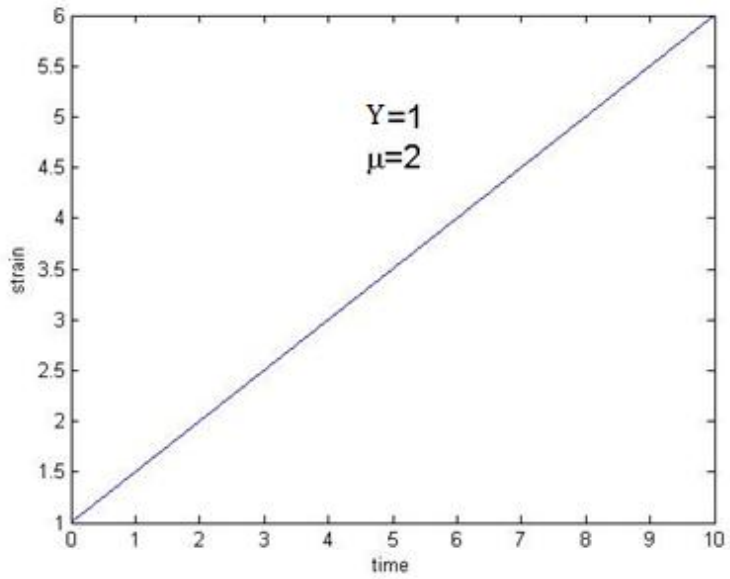

Fig. 2.4 Creep strain of the Maxwell model

It is seen that the stress relaxes to zero in the Maxwell model. The creep strain of the Maxwell model linearly increases with time. The Maxwell model is suitable to simulate responses of viscoelastic fluid-like materials.

The mechanical analog for the KV model is shown in Fig. 2.5. It has a spring and a dashpot arranged in parallel. Following a procedure as in the Maxwell model, we can form the governing equation of the KV model in Eq. (2.50). Applying a constant strain, the relaxation modulus Y(t) of the KV model is obtained as given in Eq. (2.51) where $\delta(t)$ is the Dirac delta function. Applying a constant stress to the governing equation, we obtain the creep compliance J(t) of the KV model, which is given in Eq. (2.52). The relaxation stress and creep strain of the KV model are illustrated in Fig. 2.6 and Fig. 2.7.

$$\sigma = Y\varepsilon + \mu\dot{\varepsilon} \tag{2.50}$$

$$Y(t) = \mu\delta(t) + Y \tag{2.51}$$

$$J(t) = \frac{1}{Y}(1 - e^{-\left(\frac{Y}{\mu}\right)t}) \tag{2.52}$$

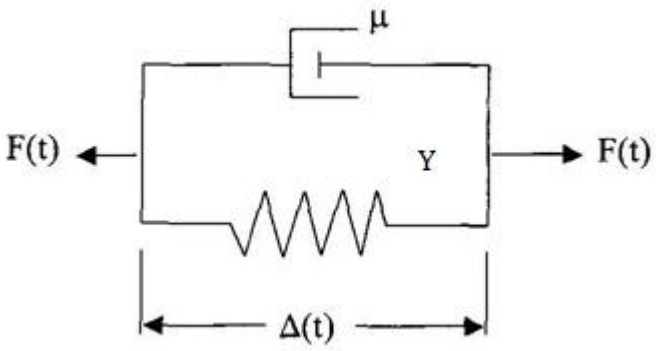

Fig. 2.5 Kelvin-Voigt model[26]

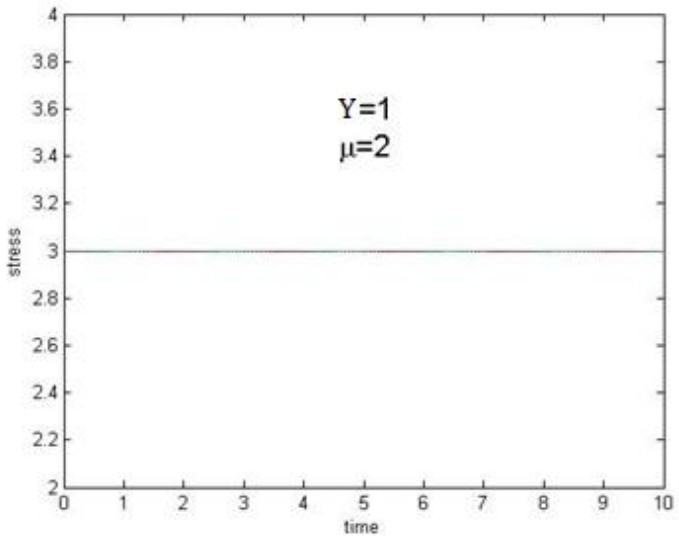

Fig. 2.6 Relaxation stress of the KV model

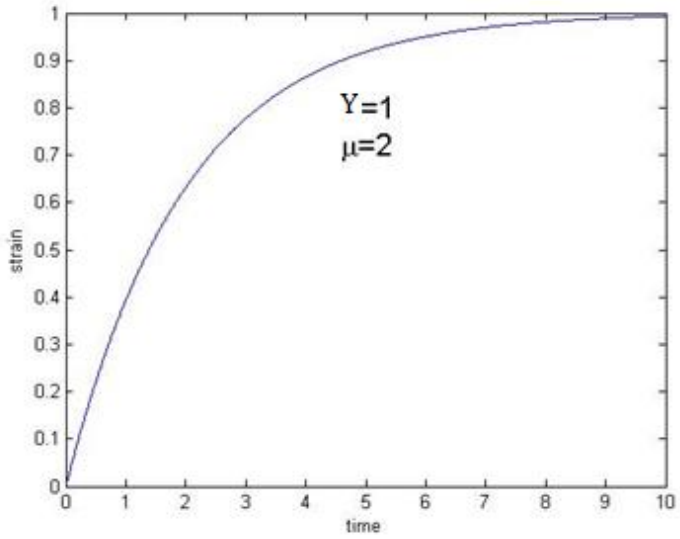

Fig. 2.7 Creep strain of the KV model

The relaxation stress in the KV model is immediately reached to a constant value. Thus, the KV model is not suitable to simulate relaxation of viscoelastic materials. Creep strain shows a gradual increase with time, approaching an asymthotic value, but it is unable to incorporate the elastic (instantaneous) response due to a sudden applied stress.

Both Maxwell and KV models are not suitable for viscoelastic solid-like materials. A mechanical analog model that is suitable for viscoelastic solid-like material is the SLS model, which is shown in Fig. 2.8. The SLS model combines a spring and a Maxwell model in parallel or a spring and a KV model in series. The governing equation of the SLS model is shown in Eq. (2.53). Applying a constant strain, we obtain a relaxation modulus Y(t) of the SLS model which is given as Eq. (2.54). Applying a

constant stress, we determine a creep compliance J(t) of the SLS model as shown in Eq. (2.55). The relaxation time is defined as $\tau_R = \frac{Y}{\mu}$, while the creep time is given as $\tau_C = \frac{Y+Y_1}{YY_1}\mu$. The relaxation stress and creep strain of the SLS model is illustrated in Fig. 2.9 and Fig. 2.10.

$$\frac{\sigma}{\mu} + \frac{\dot{\sigma}}{Y} = \frac{Y_1}{\mu}\varepsilon + [1 + \frac{Y_1}{Y}]\dot{\varepsilon} \tag{2.53}$$

$$Y(t) = Ye^{-\frac{t}{\tau_R}} + Y_1 \tag{2.54}$$

$$J(t) = \frac{1}{Y_1}(1 - \frac{Y}{Y_1+Y}e^{-\frac{t}{\tau_C}}) \tag{2.55}$$

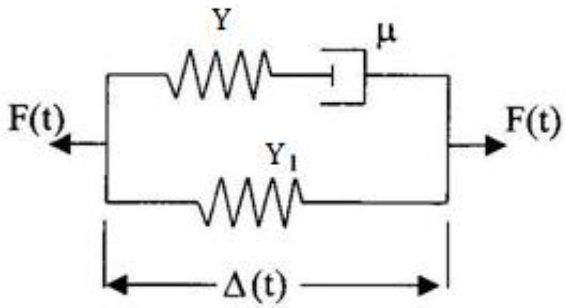

Fig. 2.8 Standard Linear Solid model[26]

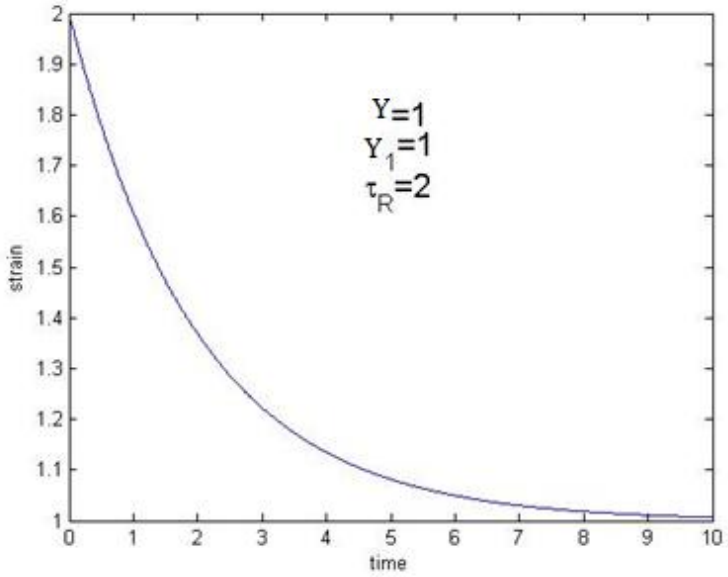

Fig. 2.9 Stress relaxation of SLS model

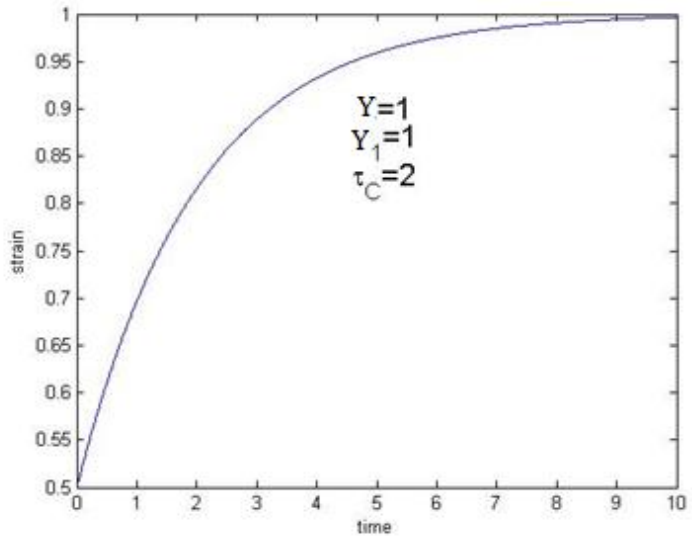

Fig. 2.10 Strain creep of SLS model

The relaxation stress shows a gradual decrease to a constant value and the creep strain exhibits a gradual increase to a constant value. Under both prescribed boundary conditions, the SLS model is capable of incorporating the elastic (instantaneous) responses. Thus, the SLS model is suitable to represent a viscoelastic solid.

The above expressions for the creep compliance and relaxation modulus are valid under a constant stress and a constant strain, respectively. For a general loading condition, the constitutive relations for linear viscoelastic materials can be derived by adopting principles of superposition and proportionality. Due to a step stress input applied at time=0, illustrated in Fig. 2.11, the strain response is written in Eq. (2.56), which is illustrated in Fig. 2.12.

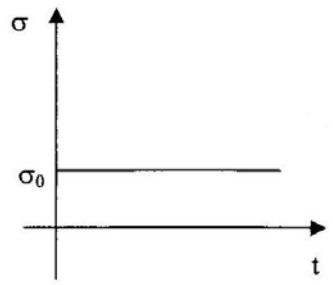

Fig. 2.11 A step stress input

$$\varepsilon(t) = \sigma_o J(t) \tag{2.56}$$

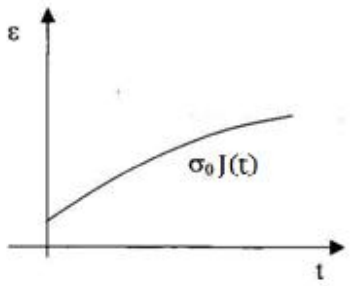

Fig. 2.12 Strain response[26]

Figure 2.13 shows a constant stress that is applied for a finite time and at time t_1, the stress is removed. We use the superposition principle to determine the strain responses due to the above prescribed stress history. The first load starts at time=0 with a magnitude $\sigma_o$and this load is held constant. The second load is applied at t_1 with a magnitude of $-\sigma_o$. The strain response at time t after t_1 is written in Eq.(2.57) and illustrated in Fig. 2.14.

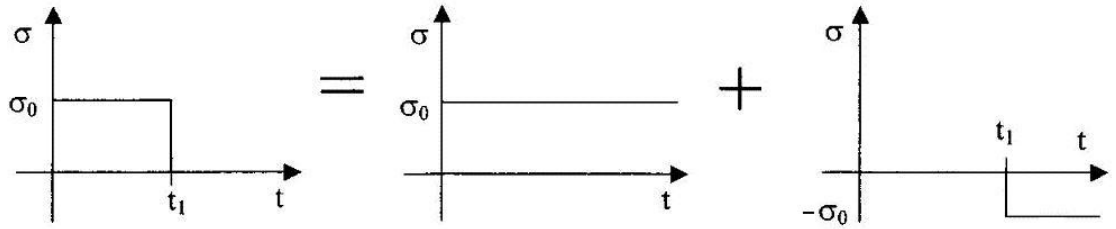

Fig. 2.13 Load and unload stress for superposition[26]

$$\varepsilon(t) = \sigma_o J(t) - \sigma_o J(t - t_1) \tag{2.57}$$

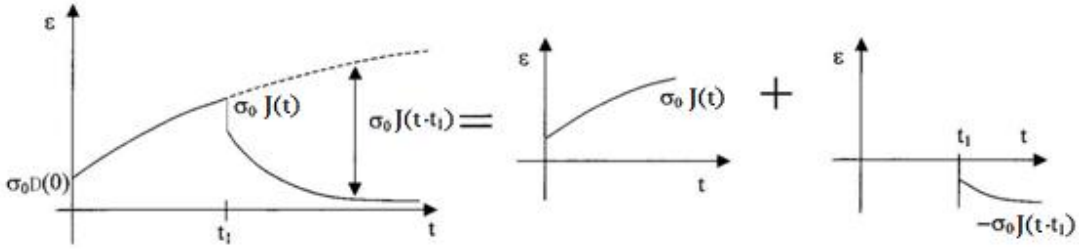

Fig. 2.14 Two step response use superposition[26]

For an arbitrary stress input in Fig. 2.15, we can use the superposition principle by considering the arbitrary input as multiple step inputs applied at different times. The arbitrary stress input is written in Eq. (2.58) where $\tilde{\sigma}$ is an approximate value of σ and 1(t) represents a unit step function. The strain response is the sum of each strain due to the multiple step stresses, which is given in Eq. (2.59).

$$\tilde{\sigma}(s) = \sigma(0)1(s) + [\sigma(t_1) - \sigma(0)]1(s - t_1) + \cdots + [\sigma(t_{k+1}) - \sigma(t_k)]1(s - t_{k+1}) + \cdots + [\sigma(t_n) - \sigma(t_{n-1})]1(s - t_n) \quad (2.58)$$

$$\tilde{\varepsilon}(t) = \sigma(0)J(t) + [\sigma(t_1)J(t - t_1) - \sigma(0)J(t - t_1)] + \cdots + [\sigma(t_n)J(t - t_n) - \sigma(t_{n-1})J(t - t_n)]$$

$$= \sum_{k=0}^{n-1} J(t - t_k)[\sigma(t_k) - \sigma(t_{k-1})] + \sigma(0)J(t) \quad (2.59)$$

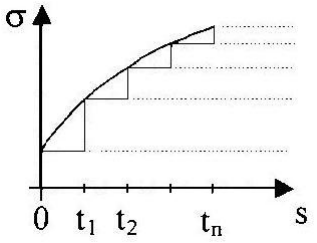

Fig. 2.15 Approximation of a stress input by a superposition of step stress[25]

In Eq. (2.59), $\tilde{\varepsilon}(t)$ denotes an approximate value of strain. We both multiply and divide $\sum_{k=0}^{n-1} J(t-t_k)[\sigma(t_k)-\sigma(t_{k-1})]$ by $(t_k - t_{k-1})$ in Eq. (2.59). We could rewrite it as:

$$\tilde{\varepsilon}(t) = \sigma(0)J(t) + \sum_{k=0}^{n-1} J(t-t_k)\frac{[\sigma(t_k)-\sigma(t_{k-1})]}{(t_k-t_{k-1})}(t_k - t_{k-1}) \qquad (2.60)$$

As the number of steps approaches infinite and $t_k - t_{k-1}$ approaches zero, $\tilde{\sigma}(t)$ approaches $\sigma(t)$ and $\tilde{\varepsilon}(t)$ approaches $\varepsilon(t)$. Equation (2.60) is rewritten as

$$\varepsilon(t) = \sigma(0)J(t) + \int_0^t J(t-s)\frac{d\sigma(t)}{ds}ds$$

$$= \sigma(0)J(t) + \int_0^t J(t-s)\dot{\sigma}(s)ds \qquad (2.61)$$

Alternative superposition method can be used to express a strain response due to an arbitrary stress input, as illustrated in Fig. 2.16. The arbitrary input is regarded as multiple impulse loadings. The approximated stress function is given in Eq. (2.62) and the approximated strain response is written in Eq. (2.63).

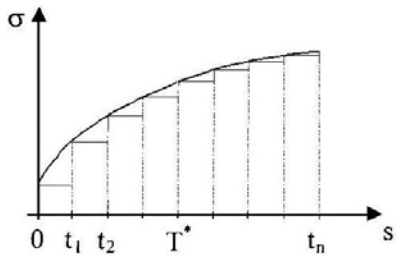

Fig. 2.16 Approximation of a stress history by pulses[26]

$$\tilde{\sigma}(s) = \sigma(0)[1(s) - 1(s - t_1)] + \cdots + \sigma(t_k)[1(s - t_k) - 1(s - t_{k+1})] + \cdots + \sigma(t_n)1(s - t_n) \quad (2.62)$$

$$\tilde{\varepsilon}(t) = \sigma(0)[J(t) - J(t - t_1)] + \sigma(t_1)[J(t - t_1) - J(t - t_2)] \ldots + \sigma(t_{k+1})[J(t - t_{k+1}) - J(t - t_{k+2})] + \cdots + \sigma(t_n)J(0)$$

$$= \sum_{k=0}^{n-1} \sigma(t_k)[J(t - t_k) - J(t - t_{k+1})] + \sigma(t_n)J(0) \quad (2.63)$$

By multiplying and dividing $\sum_{k=0}^{n-1} \sigma(t_k)[J(t - t_k) - J(t - t_{k+1})]$ in Eq. (2.63) by $(t_{k+1} - t_k)$ the strain is rewritten as:

$$\tilde{\varepsilon}(t) = \sigma(t_n)J(0) - \sum_{k=0}^{n-1} \sigma(t_k) \frac{[J(t - t_{k+1}) - J(t - t_k)]}{t_{k+1} - t_k} (t_{k+1} - t_k) \quad (2.64)$$

As the number of pulses approaches infinite and limit of $t_{k+1} - t_k$ goes to zero, $\tilde{\sigma}(s)$ will approach $\sigma(s)$ and $\tilde{\varepsilon}(s)$ will approach $\varepsilon(s)$. The strain at time t is given as:

$$\varepsilon(t) = \sigma(t)J(0) - \int_0^t \sigma(s) \frac{dJ(t - s)}{ds} ds$$

$$= \sigma(t)J(0) + \int_0^t \sigma(s)\dot{J}(t - s)ds \quad (2.65)$$

Using similar procedures, the relaxation function is written as:

$$\sigma(t) = \varepsilon(t)Y(0) + \int_0^t Y(t-s)\dot{\varepsilon}(s)ds \tag{2.66}$$

$$\sigma(t) = \varepsilon(t)Y(0) + \int_0^t \varepsilon(s)\dot{Y}(t-s)ds \tag{2.67}$$

The above relations express time-dependent mechanical behaviors which are generalized for determining time-dependent electro-mechanical behaviors for piezoelectric material, written as:

$$\varepsilon_{ij}(t) = \int_0^t S^E_{ijkl}(t-s)\frac{d\sigma_{kl}}{ds}ds + \int_0^t d_{kij}(t-s)\frac{dE_k}{ds}ds \tag{2.68}$$

$$D_i(t) = \int_0^t d_{ijk}(t-s)\frac{d\sigma_{jk}}{ds}ds + \int_0^t \kappa^{\sigma}_{ij}(t-s)\frac{dE_j}{ds}ds \tag{2.69}$$

It is also possible to form time-dependent integral models for other piezoelectric relations in Eqs. (2.15)-(2.20).

2.3 PARAMETRIC STUDIES

In this section, we examine the time-dependent piezoelectric responses in Eq.(2.68) and Eq.(2.69) subject to various electro-mechanical loadings. Most materials exhibit time-dependent responses. Depending on the loading and environmental conditions, the time-dependent effects could be negligible. In some cases, the time-dependent effect is pronounced in that it is necessary to incorporate its effect on the overall performance of materials. Polyvinylidene fluoride (PVDF) is a thermoplastic

polymer which has piezoelectric properties. It has significant time-dependent mechanical behaviors such as creep and relaxation [27] [28] even at room temperature. Like most polymers, dielectric properties of PVDF also relax with time. Fett and Thun [29] conducted creep tests at room temperature and various stresses on poled and unpoled PZTs for 30000 seconds. Significant time-dependent behaviors are observed for both poled and unpoled PZTs. Heiling and Hardtl [23] discussed an experimental observation on time-dependent surface charge of PZT. A soft PZT ceramic is tested under various constant stresses at zero electric field during 100 seconds and the charge responses are monitored. The recorded charges at several constant stresses are shown in Fig. 2.17 and the charge function of time is given in Eq. (2.70). Where Q_i is the instantaneous charge. The value of α is from 0.0498 to 0.0442 for stresses below 80MPa and $t_o = 1$, Q_o=1μC.

$$Q(t) = Q_i + Q_o\left(\frac{t}{t_o}\right)^{\alpha} \tag{2.70}$$

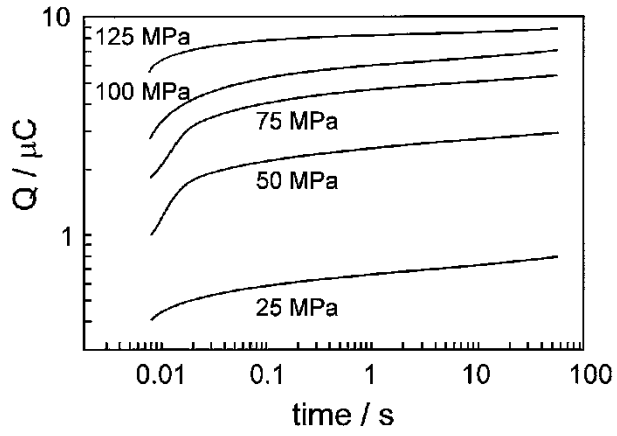

Fig. 2.17 The charge response of PZT ceramic under constant stress[30]

Where Q divided by a surface area, having a unit normal vector n_i, is the electrical displacement D_i. The time-dependent response of the electrical displacement is expressed as:

$$D_i = d_{ijk}(t)\sigma_{jk}$$

$$\sigma_{jk} = \sigma_o \tag{2.71}$$

σ_o is the constant stress. We take the piezoelectric constant d_{ijk} as:

$$d_{ijk}(t) = di_{ijk} + do_{ijk}(t)^{\alpha} \tag{2.72}$$

Where di_{ijk} is the scalar component of the instantaneous charge response and do_{ijk} is the scalar component of the transient charge response.

Fett and Thun [29] showed that the PZT strain increases by 100% under 15.4 MPa in 100 seconds. To simulate the creep data, we use exponential functions to express the time-dependent compliance. The function is given in Eq. (2.73). The corresponding linear elastic Poisson's ratios ν_{ij} are assumed to be constant.

$$S^E_{ijkl}(t) = So_{ijkl}(C_1 - C_2 e^{-Bt}) \tag{2.73}$$

The time-dependent dielectric constants of the above PZT samples are not available in the literatures. However, the dielectric constant relaxes with time under applied electrical fields as discussed by Hall [30]. The dielectric constant decreases about 10% in 100 seconds [30]. To simulate the available data, we use an exponential function of time:

$$\kappa_{ij}^{\sigma}(t) = \kappa o_{ij}^{\sigma}(C_3 + C_4 e^{-Bt}) \tag{2.74}$$

In this study, we take properties of PZT5J1 to examine the time-dependent behaviors. The x_3 axis is the polarization axis. The following values are used at initial time (constant values): $\frac{\kappa_{33}^{\sigma}}{\kappa_o} = 2600, \kappa_o = 8.854 \times 10^{-12}\,\frac{F}{m}$, $S_{3333}^{E} = 22.7 \times 10^{-12} m^2/$, $d_{333} = 500 \times 10^{-12} C/N$. Referring to Fig 2.17, we use a stress of 50 MPa and take α to be 0.0498. The value of $Q_i = Q_o = 1\mu C$ for 50 MPa stress, which results in $di_{333} = do_{333} = 500 \times 10^{-12} C/N$. The piezoelectric constant is given in Eq. (2.75). Moreover, we assumed that the compliance increases by 100% after 100 seconds, so we take $C_1 = 2$ and $C_2 = 1$. We assumed that the dielectric constant relax by 10% after 100 seconds so we take $C_3 = 1, C_4 = 0.1$, and B=0.05. The compliance and permittivity functions are given in Eq.(2.76) and Eq.(2.77).

$$d_{333}(t) = (500 + 500(t)^{0.0498}) \times 10^{-12} C/N \tag{2.75}$$

$$S_{3333}^{E}(t) = 22.7(2 - 1e^{-0.05t}) \times 10^{-12} GPa^{-1} \tag{2.76}$$

$$\kappa_{33}^{\sigma}(t) = 2600(1 + 0.1e^{-0.05t}) \times 8.854 \times 10^{-12}\,\frac{F}{m} \tag{2.77}$$

Here, we investigate time-dependent responses of piezoelectric materials subject to various boundary conditions. We applied the same scale of stress as in the literature [30] which is 50 MPa and we choose the electrical field $10^6 V/m$ to have comparable strain responses as the mechanical strains. The following case studies are considered.

Case 1: Response due to a constant stress $\sigma_{33} = \sigma_o = 50\text{MPa}$ and zero electric field.

The mechanical and electrical responses are shown in Eq. (2.78). Figure 2.18 illustrates the creep strain response under the constant stress. Figure 2.19 represents the electrical displacement response under the constant stress. The strain creeps 100% during 100 seconds and the electrical displacement creeps 15% during 100 seconds. In this case, the time-dependent responses mainly depend on the material properties.

$$\varepsilon_{33}(t) = S^E_{3333}(t)\sigma_o$$

$$D_3(t) = d_{333}(t)\sigma_o \tag{2.78}$$

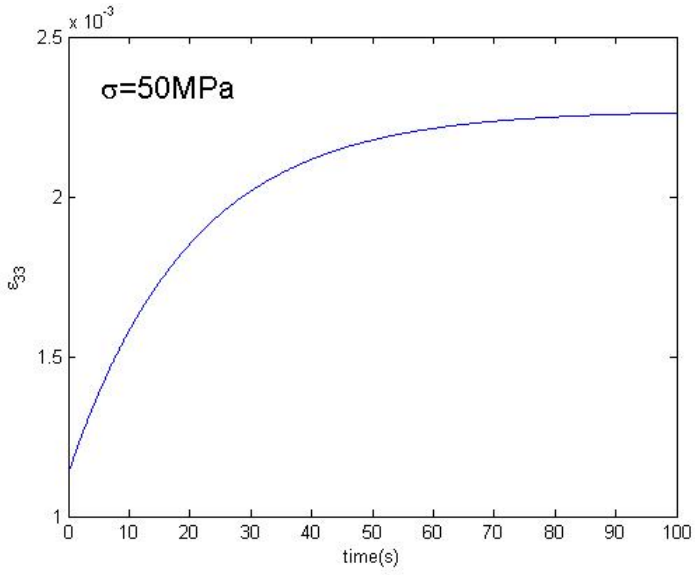

Fig. 2.18 Strain response under constant stress

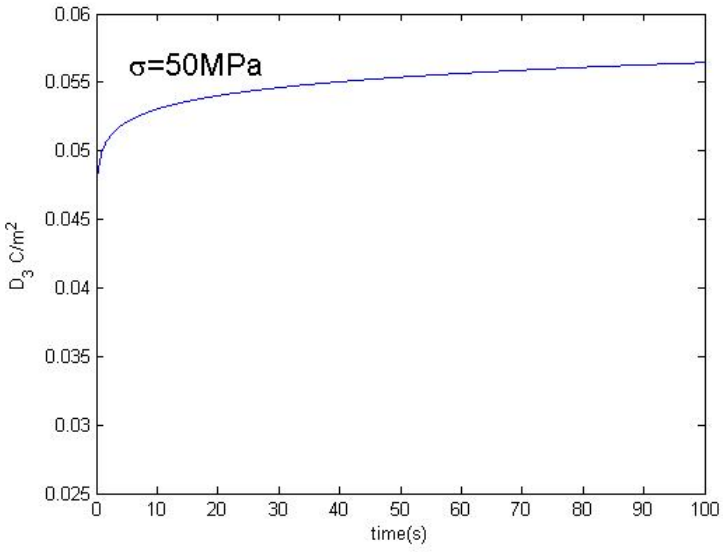

Fig. 2.19 Electrical displacement response under constant stress

Case 2: Response due to constant electrical field $E_3 = E_o = 10^6 V/m$ and zero stress.

The strain and electric displacement are given in Eq. (2.79). Figure 2.20 shows the strain response under the constant electrical field. The strain creeps 15% during 100 seconds. Figure 2.21 shows the electrical displacement response under the constant electrical field. The electrical displacement relaxes 10% under constant electrical field. The above two cases present significant time-dependent responses due to the significant time-dependent piezoelectric and dielectric constants.

$$\varepsilon_{33}(t) = d_{333}(t)E_3$$

$$D_3(t) = \kappa_{33}^{\sigma}(t)E_3 \qquad (2.79)$$

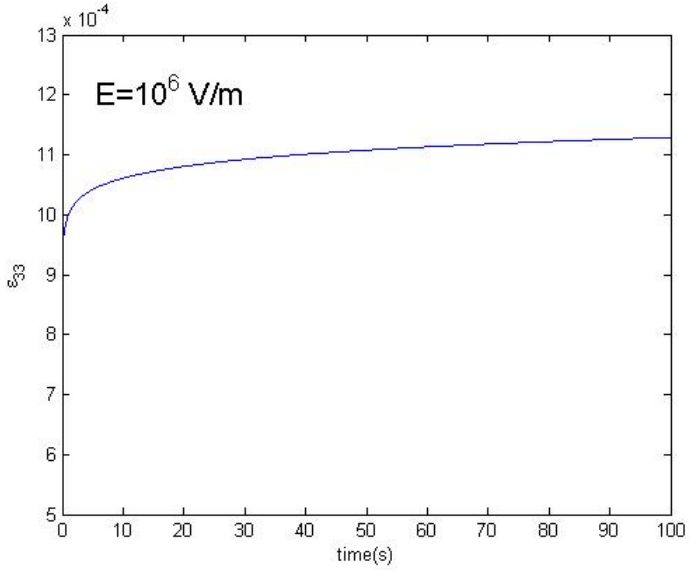

Fig. 2.20 Strain response under constant electrical field

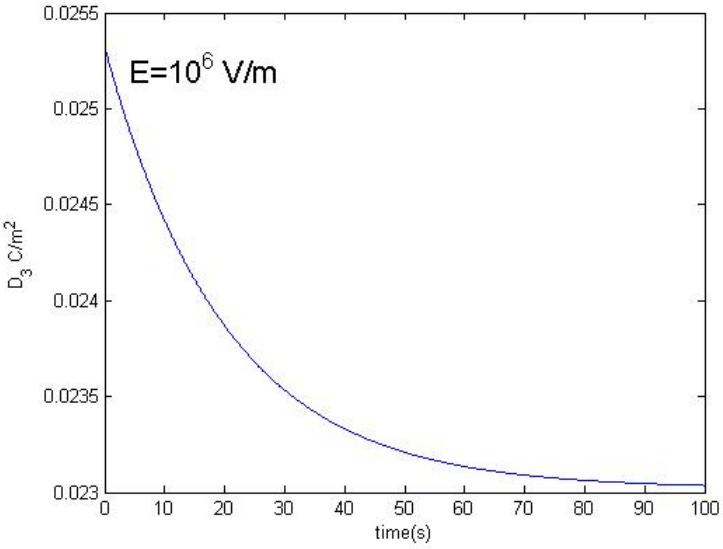

Fig. 2.21 Electrical displacement response under constant electrical field

Case 3: Response due to a ramp stress $\sigma_{33} = \beta t = 0.5t$ MPa and zero electrical field

The expressions for the mechanical and electrical responses are given in Eq. (2.80). Figure 2.22 shows the strain response with the time-dependent compliance, which is compared to the response with constant (time-independent) compliance. The strain with the time-dependent compliance rises from 0 to 0.002 which is higher than the response with the constant compliance. The strains also show some nonlinearity with time, which is due to the accumulated responses from previous loading histories. Figure 2.23 shows the electrical displacement response due to the ramp stress. The electrical displacement rises from zero to 0.055 with the time-dependent piezoelectric constant and is higher than the response with the constant piezoelectric constant, which is expected.

$$\varepsilon_{33}(t) = \beta \int_0^t S^E_{3333}(t-s)ds$$

$$D_3(t) = \beta \int_0^t d_{333}(t-s)ds \tag{2.80}$$

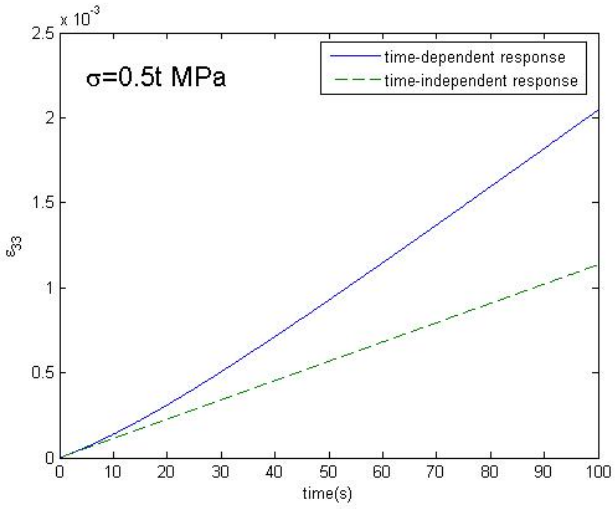

Fig. 2.22 Strain response under time-dependent stress

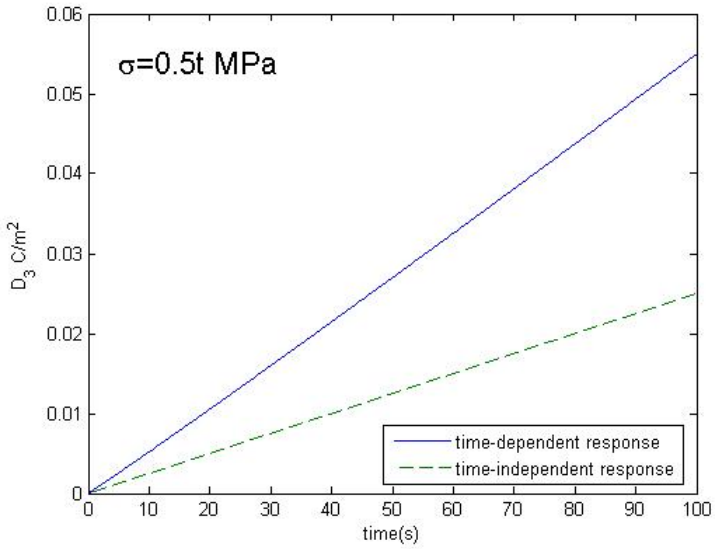

Fig. 2.23 Electrical displacement response under time-dependent stress

Case 4: Response due to a ramp electrical field $E_3 = \alpha t = 10^4 t\,V/m$

The mechanical and electrical responses are expressed in Eq. (2.81). Figure 2.24 shows the strain responses due to the above electric field. The strain with the time-dependent piezoelectric constant is much more significant than the one with a constant material property. The strain rises from 0 to 1.1×10^{-3} and the response is less than response under a constant load in Fig. 2.18. Figure 2.25 shows the electrical displacement responses. We found that the time-dependent response shows less electrical displacement due to the relaxation permittivity.

$$\varepsilon_{33}(t) = \alpha \int_0^t d_{333}(t-s)ds$$

$$D_3(t) = \alpha \int_0^t \kappa_{33}^{\sigma}(t-s)\,ds \qquad (2.81)$$

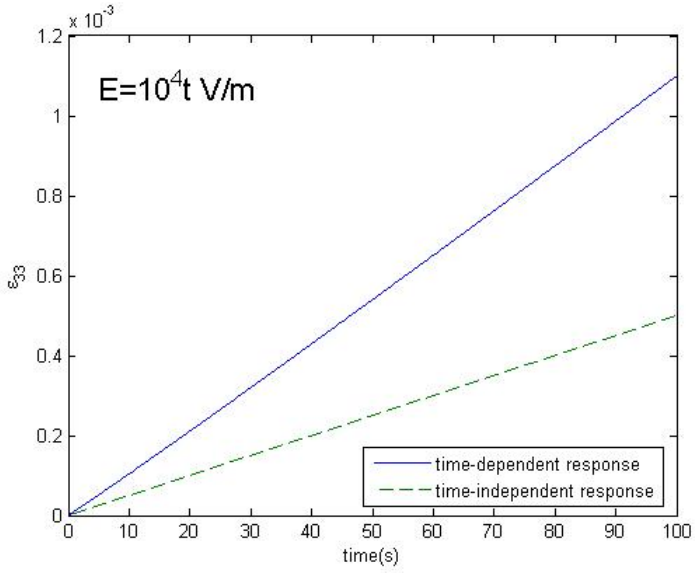

Fig. 2.24 Strain response under time-dependent electrical field

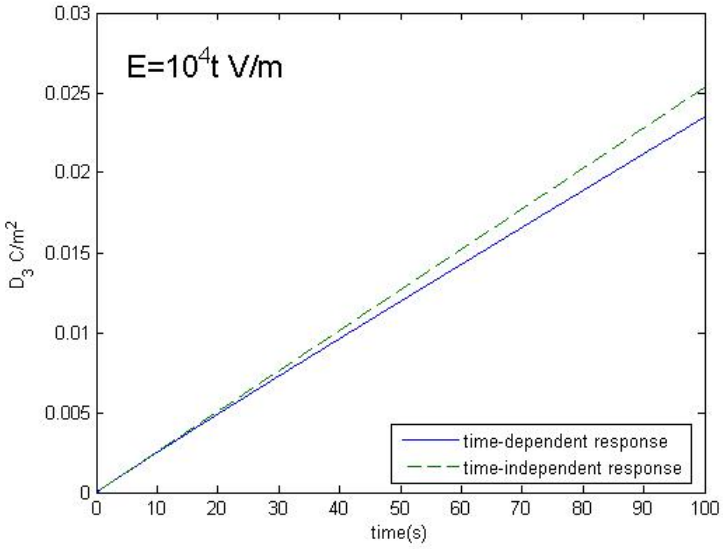

Fig. 2.25 Electrical displacement response under time-dependent electrical field

Case 5: Responses due to constant stress and time-dependent electrical field $\sigma_{33} = \sigma_o = 50\text{MPa}, E_3 = \alpha t = 10^4 t\ \text{V/m}$

The mechanical and electrical responses are given in Eq. (2.82). Fig. 2.26 shows the strain response having the time-dependent compliance and time-dependent piezoelectric constant under constant stress and ramp electric field. The response is much more pronounced that the one obtained with constant properties. We show that the time-dependent properties significantly affect the strains. Figure 2.27 shows the electrical displacement response under a constant stress and ramp electrical field. It is seen that under the combined electro-mechanical loading, the time-dependent responses show more pronounced response.

$$\varepsilon_{33}(t) = S^E_{3333}(t)\sigma_o + \alpha \int_0^t d_{333}(t-s)ds$$

$$D_3(t) = d_{333}(t)\sigma_o + \alpha \int_0^t \kappa^\sigma_{33}(t-s)\, ds \tag{2.82}$$

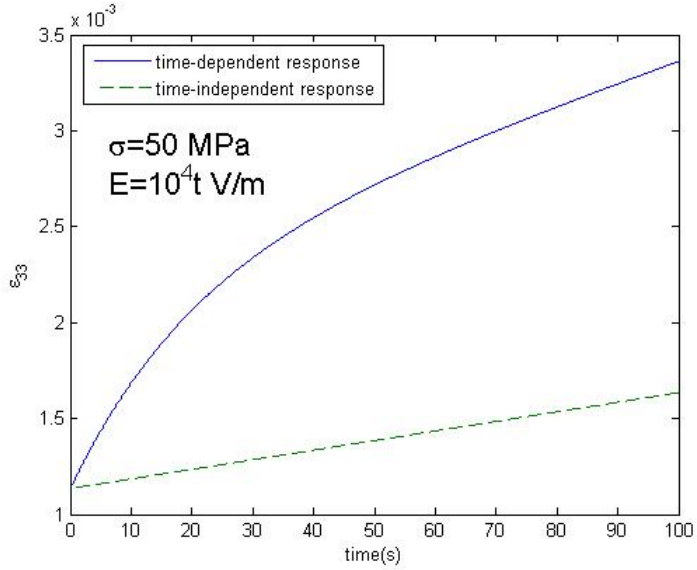

Fig. 2.26 Strain response under constant stress and time-dependent electrical field

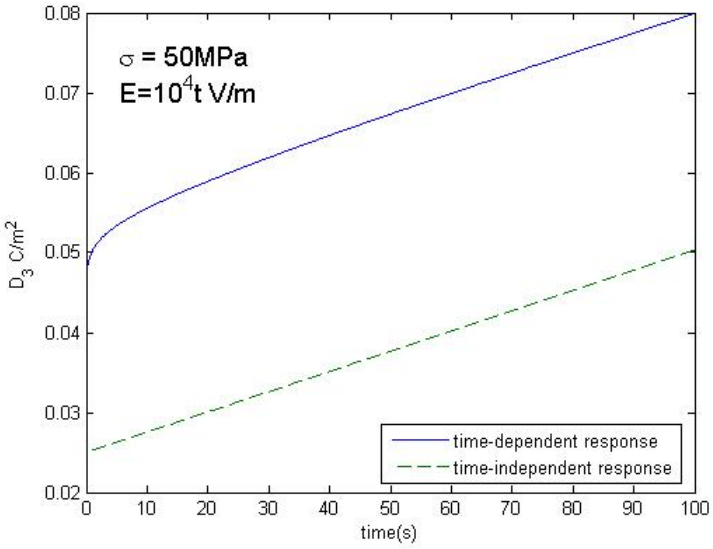

Fig. 2.27 Electrical displacement response under constant stress and time-dependent electrical field

Case 6: Response due to time-dependent stress and time-dependent electrical field

$\sigma_{33} = \beta t = 0.5t\ \text{MPa}, E_3 = \alpha t = 10^4 t\ \text{V/m}$

The mechanical and electrical responses are shown in Eq. (2.83). Figure 2.28 shows the strain response having time-dependent compliance and time-dependent piezoelectric constant under ramp stress and electrical field. Figure 2.29 shows the electrical displacement response having time-dependent piezoelectric constant and permittivity subject to the ramp stress and electrical field. It is seen that when the time-dependent effects are considered, response of materials could be differ significantly compared to when constant properties are considered.

$$\varepsilon_{33}(t) = \beta \int_0^t S^E_{3333}(t-s)ds + \alpha \int_0^t d_{333}(t-s)ds$$

$$D_3(t) = \beta \int_0^t d_{333}(t-s)ds + \alpha \int_0^t \kappa^\sigma_{33}(t-s)\,ds \tag{2.83}$$

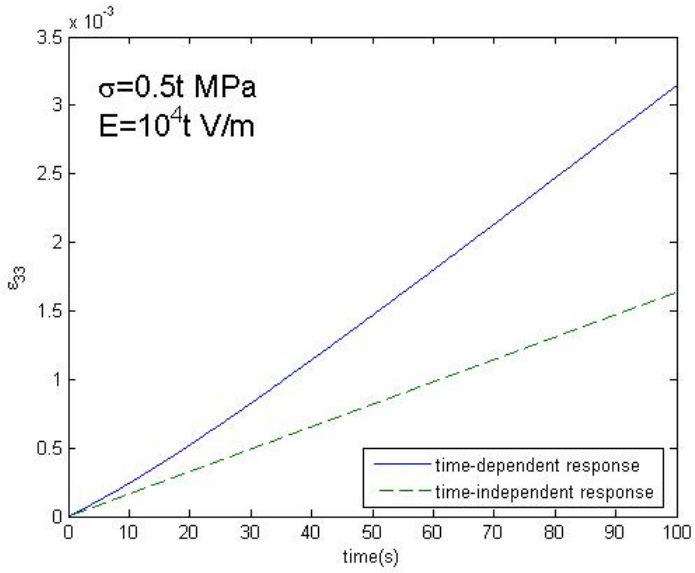

Fig. 2.28 Strain response under time-dependent stress and time-dependent electrical field

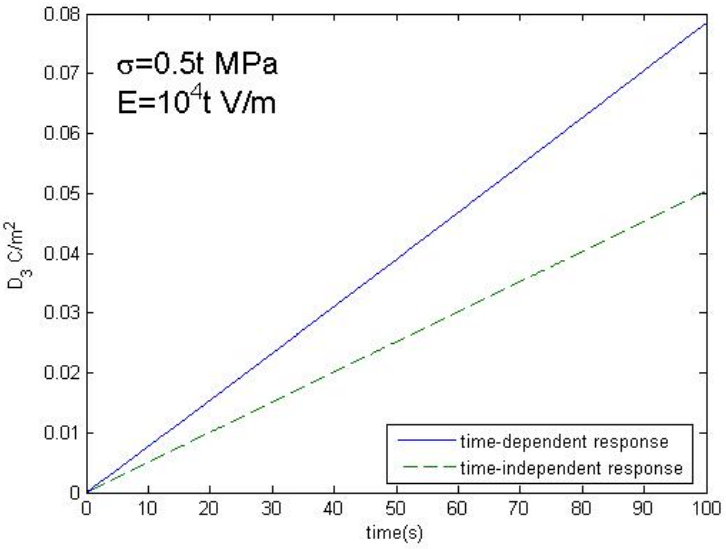

Fig. 2.29 Electrical displacement response under time-dependent stress

and time-dependent electrical field

CHAPTER III
MICROMECHANICAL MODELS FOR PIEZOCOMPOSITES

This chapter determines effective electro-mechanical and piezoelectric responses of piezoelectric fiber composites (PFCs) using micromechanical models. Microstructures of active fiber composites (AFCs) and macro fiber composites (MFCs) are modeled using finite element (FE). To reduce complexity in generating the microstructures of the AFC and MFC, the existence of the interdigitated electrode fingers placed on the top and bottom surfaces is ignored and an electric field is assumed uniformly distributed along the fiber longitudinal axis. Available micromechanical models and experimental data in the literatures are used to validate the presented micromechanical models. The effect of viscoelastic matrix, which is pronounced at elevated temperatures, on the overall performance of PFCs is also examined.

3.1 CHARACTERISTICS OF PFC

Piezoelectric ceramics have high electro-mechanical properties compared to those of piezoelectric polymers, but their brittle characteristic makes them easy to break and less flexible. PFC made of PZT fibers dispersed in epoxy matrix improves the flexibility of transducers and enhances the resistance to brittle failure. The existence of polymer matrix prevents catastrophic failure due to fiber breakage and forms pliable piezocomposites, which makes PFC suitable for large scale actuation. Figure 3.1 shows the flexibility of PFC.

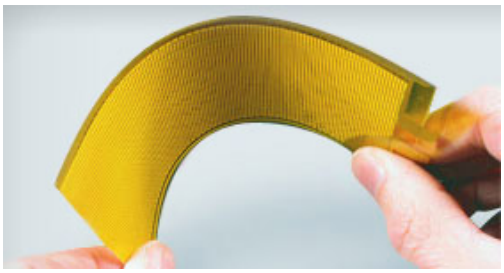

Fig. 3.1 Flexibility of PFC(Materials Systems Inc.)

The microstructure of PFC consists of interdigitated electrode (IDE), epoxy matrix and piezoceramic fibers. The IDE is printed on a Kapton substrate which is placed on the top and bottom surfaces of the PFC. The PZT fibers are aligned and embedded in epoxy matrix. The IDEs are used to induce electric field that runs through the longitudinal fiber axis. The space between the fiber sheet and IDEs are filled with epoxy which bonds the fibers and IDEs and prevents crack propagation in the ceramic fibers. This study deals with two kinds of PFCs, which are AFC and MFC. The microstructure of AFC is schematically shown in Fig. 3.2. The microstructure of MFC is illustrated in Fig. 3.3.

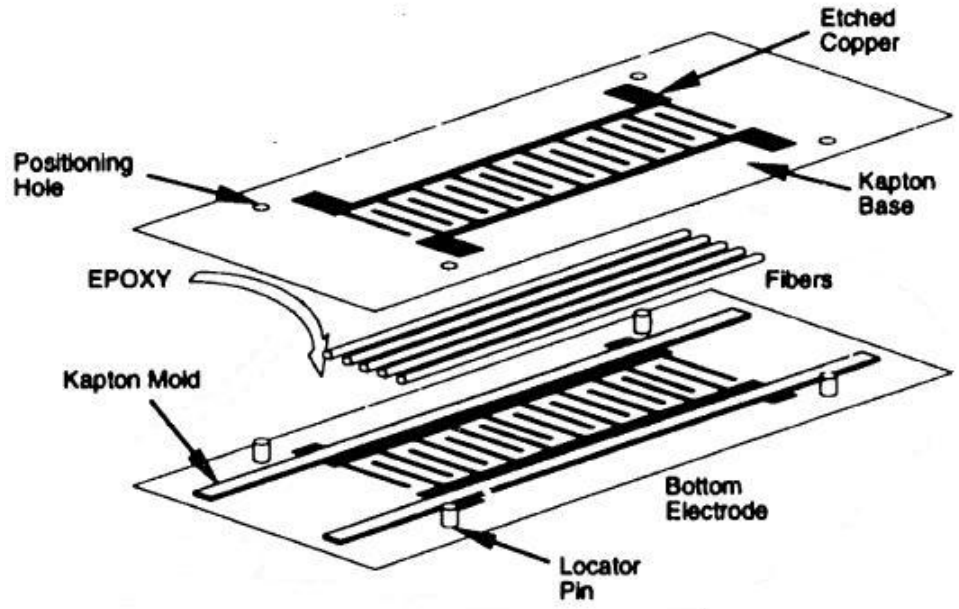

Fig. 3.2 Structure of active fiber composite[2]

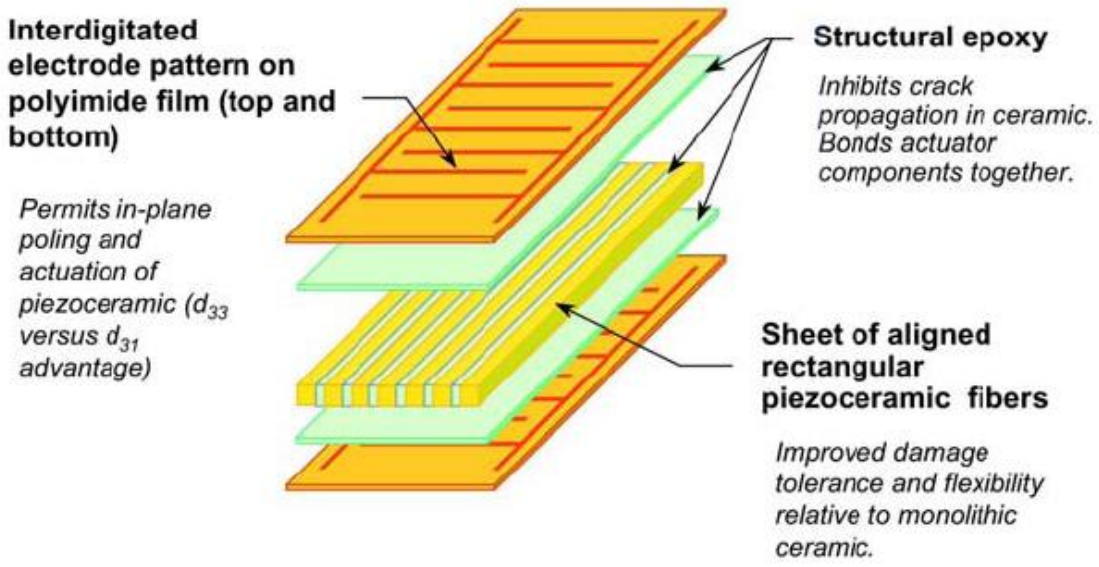

Fig. 3.3 Structure of macro fiber composite (Smart Material Corp.)

The microstructures of AFC and MFC are similar except in the shape and type of the fibers. The MFC uses fibers with a rectangular cross-section and AFC uses fibers with a circular cross-section. Various PZT fibers have been used for both AFC and MFC. Increasing fiber volume fractions in the piezo composites leads to better actuation and higher overall properties. MFC can have higher volume fractions than the AFC due to the restriction in the fiber cross-section. For example in a unit area of a square cross-section, the largest area that a circular cross-section can be superposed inside the square cross-section is 0.785. The fiber volume content of MFC could reach up to 0.824[9]. Although it is possible to create MFC with higher fiber contents than 0.824, less amount of epoxy matrix decreases the bonding between the fiber and matrix constituents. Figure 3.4(a) and 3.4(b) illustrate the representations of AFC and MFC.

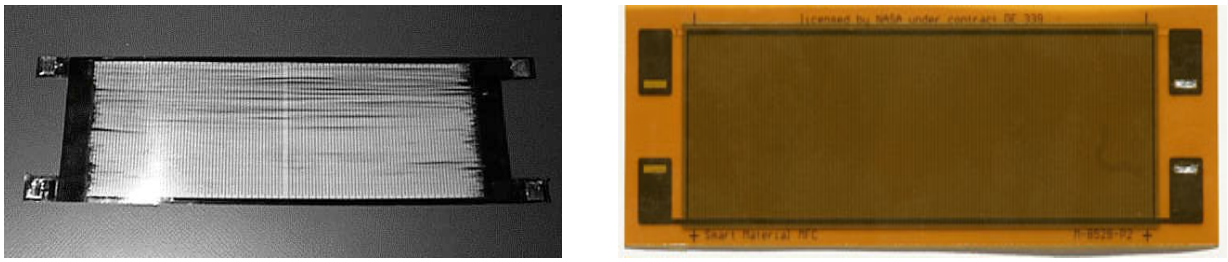

(a) (b)

Fig. 3.4 (a) Photo of AFC (CeraNova Corp.) (b) Photo of MFC (Smart Material Corp.)

3.2 MICROMECHANICAL MODELS OF PFC MICROSTRUCTURES

Micromechanical models for AFC and MFC are generated using FE. Two unit-cell models are considered. The first unit-cell model consists of a single fiber of a square or circular cross-section surrounded by epoxy matrix. The second unit-cell model consists of five fibers embedded in epoxy. We ignore the existence of the Kapton substrate and electrodes as the size of the Kapton substrate and electrodes are small compared to the size of the epoxy and fiber. The average diameter of PZT fibers in the AFC is 0.25mm. The thickness of Kapton substrate is 0.0254mm and the thickness of copper electrode is less than 0.0196mm [4]. We assume that the electric field is distributed uniformly along the longitudinal fiber axis. Different sizes of fibers constitute different fiber area (or volume fractions). In this study, AFC and MFC having 20%, 40% and 60% fiber contents are generated by varying the fiber dimensions. Figure 3.5 shows schematic representations of unit-cell models of AFC and MFC having a single fiber and Table 3.1 reports the sizes of fibers for the three volume contents. Where R represents the radius of the AFC fiber and L represents the side length of the MFC fiber.

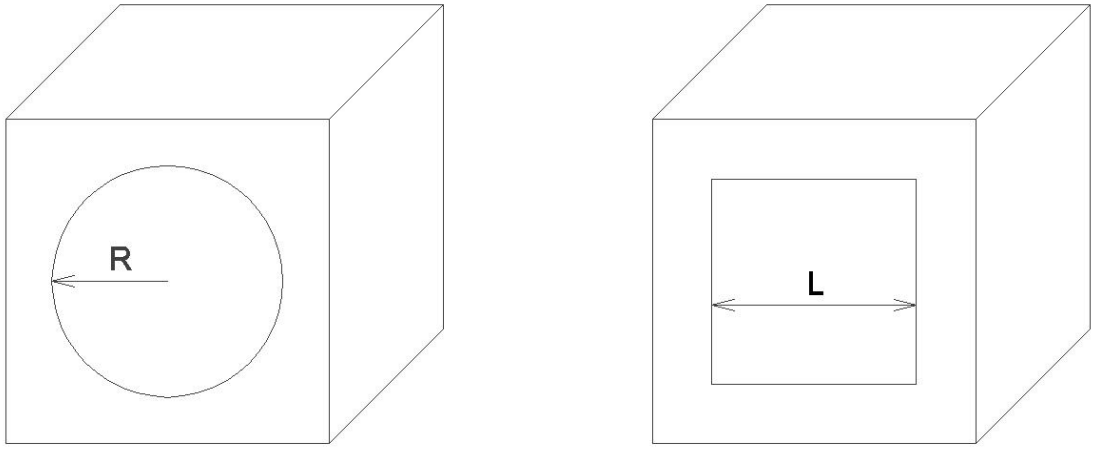

Fig. 3.5 Micromechanical models with a single fiber

Table 3.1 The fiber sizes of micromechanical models

Type/volume fractions	60	40	20
AFC	R=0.437	R=0.357	R=0.252
MFC	L=0.775	L=0.632	L=0.447

In addition, multi-fiber models are generated. We create unit-cells with multiple fibers and compare the effective responses of the micromechanical models with one and five fibers. We generate the multiple fiber unit-cell models for composite with 40% fiber volume fraction, which are shown in Fig. 3.6.

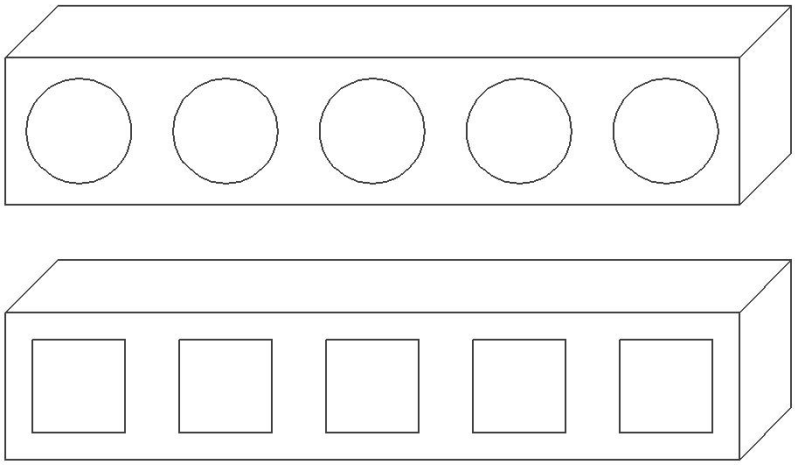

Fig. 3.6 Five fiber micromechanical model (vf=40%)

The micromechanical models are generated using ABAQUS FE software. Three-dimensional solid element, C3D8E, is used. The single fiber model has 10000 elements and 5 fibers model has 50000 elements. The AFC and MFC FE unit-cell models are presented in Figs. 3.7 - 3.10.

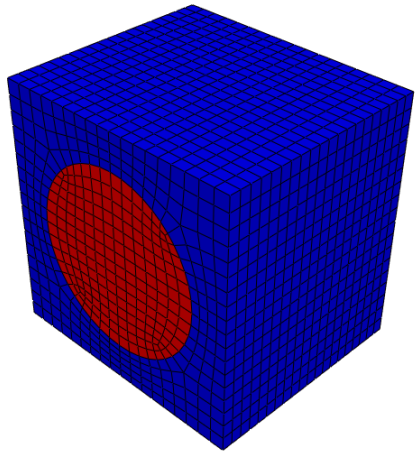

Fig. 3.7 Finite element model of AFC

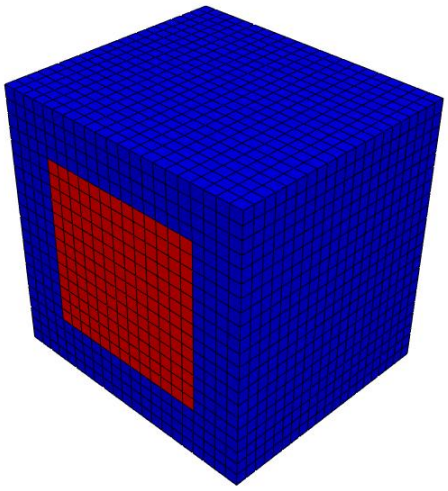

Fig. 3.8 Finite element model of MFC

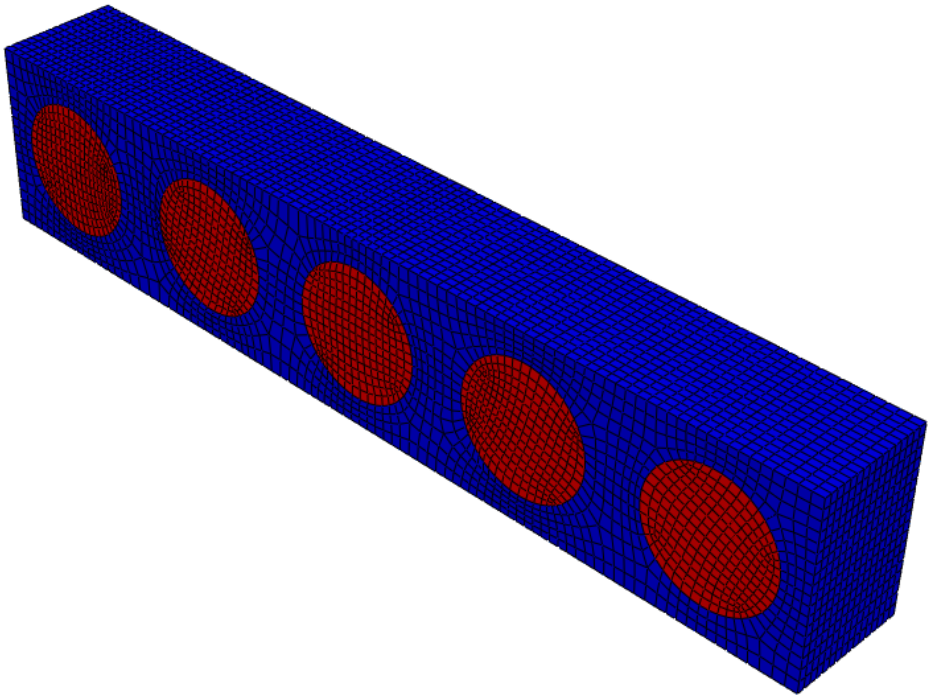

Fig. 3.9 5 fibers finite element model of AFC

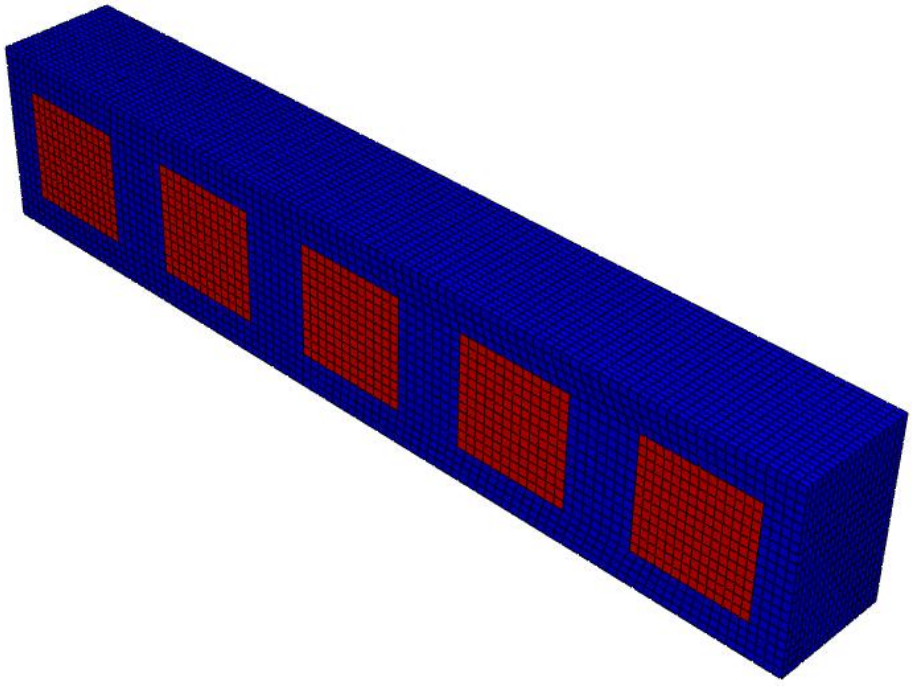

Fig. 3.10 5 fibers finite element model of AFC

To determine effective properties of the AFC and MFC, we prescribe different boundary conditions. Figure 3.11 illustrates a cubic element with surface boundaries 1 - 6. The surfaces 1, 2, 3 denote surfaces with a unit outward normal in the positive x_1,x_2 and x_3 directions, respectively. The surfaces 4, 5, 6 indicate surfaces with a unit outward normals in the negative x_1, x_2, and x_3 directions, respectively. Different boundary conditions are prescribed to determine the effective electro-mechanical and piezoelectric constants, which are summarized in Table 3.2. Variable $U_1=0$ represents the displacement component in x_1 direction, $\sigma_{11}=\sigma_o$ represents the stress applied to a surface, whose unit outward normal in x_1 direction with a traction component in x_1-direction. $C=Q$ represents the applied charge Q.

To characterize the moduli Y_{11} and Y_{33}, we apply constant stresses $\sigma_{11}=\sigma_o$ and $\sigma_{33}=\sigma_o$, respectively. The strain responses ε_{11} and ε_{33} are monitored and the elastic moduli are determined by:

$$Y_{11} = \frac{\sigma_{11}}{\varepsilon_{11}}, Y_{22} = Y_{11}$$

$$Y_{33} = \frac{\sigma_{33}}{\varepsilon_{33}} \tag{3.1}$$

The Poisson's ratios are calculated as:

$$\nu_{13} = -\frac{\varepsilon_{33}}{\varepsilon_{11}} \text{ due to } \sigma_{11}$$

$$\nu_{12} = -\frac{\varepsilon_{22}}{\varepsilon_{11}} \text{ due to } \sigma_{11}$$

$$\nu_{23} = -\frac{\varepsilon_{33}}{\varepsilon_{22}} \text{ due to } \sigma_{22} = \sigma_{11} \tag{3.2}$$

For characterizing the shear moduli G_{12} and G_{13}, we apply constant stresses $\sigma_{12}=\sigma_o$ and $\sigma_{13}=\sigma_o$, respectively. We calculate the shear strains γ_{11} and γ_{33} and determine the shear moduli as:

$$G_{12} = \frac{\sigma_{12}}{\gamma_{12}}$$

$$G_{31} = \frac{\sigma_{31}}{\gamma_{31}}$$

$$G_{23} = G_{31} \tag{3.3}$$

For determining the piezoelectric constants, we use piezoelectric relation in Eq. 2.15 and the compliance matrix in Eq. 3.4. The elastic moduli and Poisson's ratio in the compliance matrix are given in Eqs. (3.1)-(3.3). The compliance matrix is the inverse of the stiffness matrix (Eq. 3.5). We apply $\sigma_{31}=\sigma_o$ and surface charge Q for calculating e_{113}. We apply $\sigma_{11}=\sigma_o$ and surface charge Q for determining e_{311}. Then we apply $\sigma_{33}=\sigma_o$ and surface charge Q for obtaining e_{333}. The detailed calculation is presented in Eq. 3.6.

$$[S] = \begin{bmatrix} \frac{1}{Y_{11}} & \frac{-V_{21}}{Y_{22}} & \frac{-V_{31}}{Y_{33}} & 0 & 0 & 0 \\ \frac{-V_{12}}{Y_{11}} & \frac{1}{Y_{22}} & \frac{-V_{32}}{Y_{33}} & 0 & 0 & 0 \\ \frac{-V_{13}}{Y_{11}} & \frac{-V_{23}}{Y_{22}} & \frac{1}{Y_{33}} & 0 & 0 & 0 \\ 0 & 0 & 0 & \frac{1}{2G_{23}} & 0 & 0 \\ 0 & 0 & 0 & 0 & \frac{1}{2G_{31}} & 0 \\ 0 & 0 & 0 & 0 & 0 & \frac{1}{2G_{12}} \end{bmatrix} \tag{3.4}$$

$$[C] = [S]^{-1} \tag{3.5}$$

$$e_{311} = \frac{C^E_{1111}\varepsilon_{11} + C^E_{1122}\varepsilon_{22} + C^E_{1133}\varepsilon_{33} - \sigma_{11}}{E_3}, e_{322} = e_{311}$$

$$e_{333} = \frac{C^E_{3311}\varepsilon_{11} + C^E_{3322}\varepsilon_{22} + C^E_{3333}\varepsilon_{33} - \sigma_{33}}{E_3}$$

$$e_{113} = e_{131} = e_{223} = e_{232} = \frac{C^E_{1313}\varepsilon_{13} - \sigma_{13}}{E_1} \tag{3.6}$$

For characterizing the dielectric constants, we only apply surface charge on x_1 and x_3 direction, respectively. The dielectric constants are determined from:

$$\kappa^\sigma_{11} = \frac{D_1}{E_1}, \kappa^\sigma_{22} = \kappa^\sigma_{11}$$

$$\kappa^\sigma_{33} = \frac{D_3}{E_3} \tag{3.7}$$

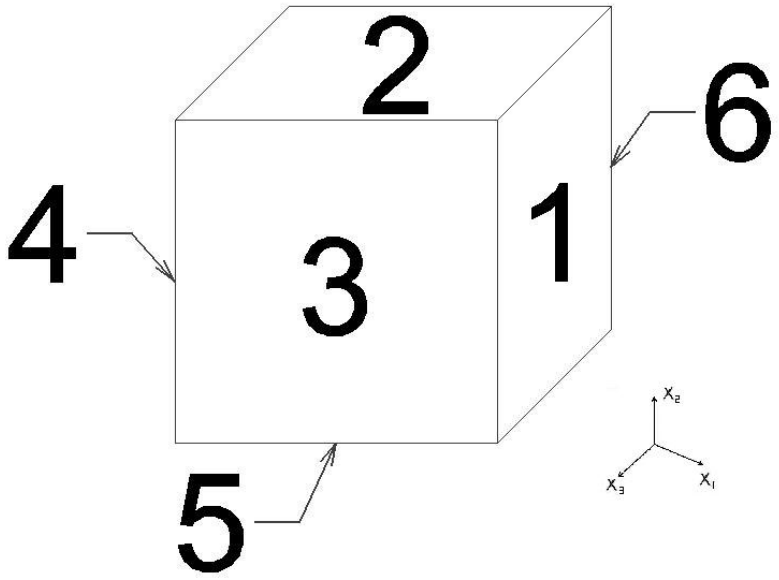

Fig. 3.11 Surface numbers of boundary conditions

Table 3.2 Boundary conditions to determine effective properties

Property/surface	1	2	3	4	5	6
$Y_{11}=Y_{22}$	$\sigma_{11}=\sigma_o$			$U_1=0$	$U_2=0$	$U_3=0$
Y_{33}			$\sigma_{33}=\sigma_o$	$U_1=0$	$U_2=0$	$U_3=0$
$G_{23}=G_{31}$	$U_2=0$ $U_3=0$	$U_2=0$ $U_3=0$	$\sigma_{31}=\sigma_o$ $U_2=0$ $U_3=0$	$U_2=0$ $U_3=0$	$U_1=0$ $U_2=0$ $U_3=0$	$U_2=0$ $U_3=0$
G_{12}	$\sigma_{12}=\sigma_o$ $U_2=0$ $U_3=0$	$U_2=0$ $U_3=0$	$U_2=0$ $U_3=0$	$U_2=0$ $U_3=0$	$U_2=0$ $U_3=0$	$U_1=0$ $U_2=0$ $U_3=0$
$e_{113}=e_{131}$ $=e_{223}=e_{232}$	$C=Q$ $U_2=0$ $U_3=0$	$U_2=0$ $U_3=0$	$\sigma_{31}=\sigma_o$ $U_2=0$ $U_3=0$	$C=-Q$ $U_2=0$ $U_3=0$	$U_2=0$ $U_3=0$	$U_1=0$ $U_2=0$ $U_3=0$
$e_{311}=e_{322}$	$\sigma_{11}=\sigma_o$		$C=Q$	$U_1=0$	$U_2=0$	$C=-Q$ $U_3=0$
e_{333}			$\sigma_{33}=\sigma_o$ $C=Q$	$U_1=0$	$U_2=0$	$C=-Q$ $U_3=0$
κ_{11}/κ_o	$C=Q$ $U_2=0$ $U_3=0$	$U_2=0$ $U_3=0$	$U_2=0$ $U_3=0$	$C=-Q$ $U_2=0$ $U_3=0$	$U_2=0$ $U_3=0$	$U_1=0$ $U_2=0$ $U_3=0$
κ_{33}/κ_o			$C=Q$	$U_1=0$	$U_2=0$	$C=-Q$ $U_3=0$

3.3 EFFECTIVE ELECTRO-MECHANICAL PROPERTIES OF AFC AND MFC

We now verify the micromechanical models by comparing the calculated effective material properties with the ones obtained from the analytical results and experimental data available in the literatures. We use analytical solutions in Odegard [16] and experimental data reported by Nelson [3]. Odegard studied piezocomposites having PZT-7A fibers and LaRC-SI matrix. The properties of the constituents at room temperature are given in Table 3.3 and Table 3.4. The longitudinal fibers are placed in the x_3-direction. The piezocomposites reported by Nelson et al. [3] consist of PZT-5A fibers manufactured by Sol-Gel process and epoxy. The reported properties of the PZT-5A fibers are given in Table 3.5. All other electro-mechanical properties for the PZT-5A are taken from a general PZT-5A ceramics which are given in Table 3.6. Table 3.7 presents the properties of the epoxy matrix.

Table 3.3 Properties of PZT-7A

C^E_{1111}(GPa)	C^E_{1122}	C^E_{1133}	C^E_{2222}	C^E_{2233}	C^E_{3333}	C^E_{2323}	C^E_{3131}	C^E_{1212}
148.0	76.2	74.2	148.0	74.2	131.0	25.4	25.4	35.9
e_{113}(C/m^2)	e_{311}	e_{322}	e_{333}	$\kappa^{\varepsilon}_{11}/\kappa_o$	$\kappa^{\varepsilon}_{22}/\kappa_o$	$\kappa^{\varepsilon}_{33}/\kappa_o$		
9.2	-2.1	-2.1	9.5	460	460	235		

(κ_o=8.854187816*10^{-12}F/m)

Table 3.4 Properties of LaRC-SI

C_{1111}(GPa)	C_{1122}	C_{1133}	C_{2222}	C_{2233}	C_{3333}	C_{2323}	C_{3131}	C_{1212}
8.1	5.4	5.4	8.1	5.4	8.1	1.4	1.4	1.4
e_{113}(C/m^2)	e_{311}	e_{322}	e_{333}	$\kappa^{\varepsilon}_{11}/\kappa_o$	$\kappa^{\varepsilon}_{22}/\kappa_o$	$\kappa^{\varepsilon}_{33}/\kappa_o$		
0.0	0.0	0.0	0.0	2.8	2.8	2.8		

Table 3.5 Properties of PZT-5A by Sol-Gel process

d_{333}(10^{-12}CN^{-1})	d_{311}	k_{33}	$\kappa^{\sigma}_{33}/\kappa_o$	S^{E}_{3333}(10^{-12}Pa^{-1})	S^{D}_{3333}(10^{-12}Pa^{-1})
263	-102	0.61	1350	15.3	9.7

Table 3.6 Properties of PZT-5A

C^{E}_{1111}(GPa)	C^{E}_{1122}	C^{E}_{1133}	C^{E}_{3333}	C^{E}_{3232}
120	75.2	75.1	111	21
e_{113}(C/m^2)	e_{311}	e_{333}	$\kappa^{\sigma}_{11}/\kappa_o$	$\kappa^{\sigma}_{33}/\kappa_o$
12.3	-5.2	15.8	1700	1730

Table 3.7 Properties of epoxy

S_{1111}(10^{-12}Pa^{-1})	S_{1122}	κ_{11}/κ_o
357	-136	5

3.3.1 RESPONSES OF PZT-7A / LARC-SI COMPOSITES

Odegard [16] derived a micromechanical model to predict electro-mechanical behaviors of piezo-composites, which are presented in Eq. (3.8). Where $\mathbf{Y}$ is the electromechanical modulus, c_r is the volume fraction of phase r, N is the number of phase, $\mathbf{A}_r$ is the concentration tensor of phase r, $\mathbf{S}_r$ is the constraint tensor of phase r which is analogous to the Eshelby tensor used in determining elastic properties of the composite materials, $\mathbf{Y}_0$ is the electroelastic moduli of the reference medium, and r=1 is the matrix phase. These equations are used to calculate the mechanical and electrical properties of piezoelectric composites.

$$\mathbf{Y} = \mathbf{Y}_1 + \sum_{r=2}^{N} c_r(\mathbf{Y}_r - \mathbf{Y}_1)\mathbf{A}_r$$

$$\mathbf{A}_r = [\mathbf{I} + \mathbf{S}_r\mathbf{Y}_0^{-1}(\mathbf{Y}_r - \mathbf{Y}_0)]^{-1}$$

$$Y_{iJMn} = \begin{cases} C_{ijmn}, & J, M = 1,2,3, \\ e_{nij}, & J = 1,2,3;\ M = 4, \\ e_{imn}, & J = 4; M = 1,2,3, \\ -\kappa_{in}, & J, M = 4, \end{cases}$$

$$Y^0_{iJKl} = Y^1_{iJKl}\frac{1+\sum_{r=2}^{N}\eta^r_{iJKl}c_r}{1-\sum_{r=2}^{N}\eta^r_{iJKl}c_r}, \text{ where } \eta^r_{iJKl} = \frac{Y^r_{iJKl}-Y^1_{iJKl}}{Y^r_{iJKl}+Y^1_{iJKl}} \quad (3.8)$$

Odegard[16] also generated FE models of a representative volume element (RVE) of fiber reinforced piezocomposites and compared the responses of the micro-mechanical and RVE-FE models. The RVE model consists of a hexagonal packing arrangement of fibers dispersed in polymers, as illustrated in Fig. 3.12. To determine the effective

mechanical and electrical properties of the RVE models, an internal energy is first calculated (Eq. 3.9). Where V is the volume of the RVE; C_{ijkl}, κ_{ij} and e_{ijk} are the scalar components of the stiffness, permittivity and piezoelectric constants. Variables ε_{ij}^{o} and E_{j}^{o} are the applied strain and electrical field.

$$U_e = \frac{V}{2} C_{ijkl} \varepsilon_{ij}^{o} \varepsilon_{kl}^{o}$$

$$U_d = \frac{V}{2} \kappa_{ij} E_i^{o} E_j^{o}$$

$$U_{em} = \frac{V}{2} e_{ijk} \varepsilon_{jk}^{o} E_i^{o} \tag{3.9}$$

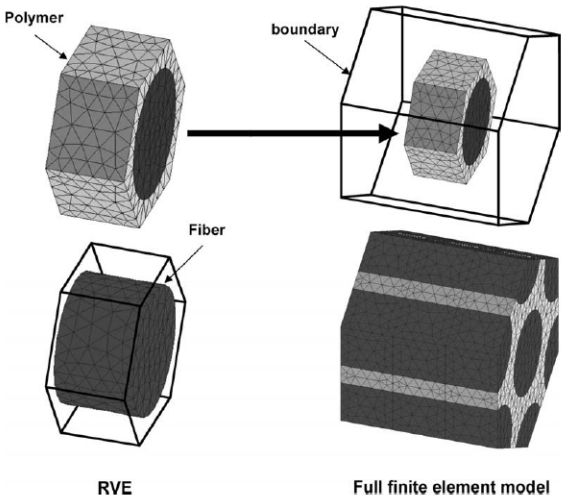

Fig. 3.12 RVE model

We compare the effective properties of the Odegard micro-mechanical model, the RVE value, and the micromechanical models of the AFC and MFC for composites having 20, 40, and 60% fiber contents, which are given in Table 3.8 - Table 3.11. We

calculated errors between the properties determined from the AFC model and the ones from the Odegard and RVE models. Table 3.8 to Table 3.11 show the effective properties of AFC and MFC at different fiber volume fractions.

Table 3.8 presents the results of a single fiber micromechanical model for AFC and MFC at volume fraction 60%. It is seen that the properties in the axial fiber direction (x_3-direction) are comparable for all models. However, the transverse and shear properties show some mismatches. Comparing with the Odegard model, the value of $Y_{11}=Y_{22}$ from the AFC is 15% higher than Odegard model, and the values for $G_{23}=G_{13}$, G_{12} and κ_{11}/κ_o are 30% lower than the Odegard model. The properties of Y_{33}, e_{333} andκ_{33}/κ_o are comparable with the Odegard model. Comparing with the RVE model, we find that $Y_{11}=Y_{22}$ and G_{12} of the AFC are 60 % higher than the RVE model, κ_{11}/κ_o is 30% higher than the RVE model while Y_{33}, e_{333} andκ_{33}/κ_o are compatible with the RVE model. The mismatches in the transverse and shear properties are attributed to the shape and microstructural arrangement of fibers. When loaded in the transverse fiber direction, contact between fibers could result in localized stresses between the fibers, which cannot be captured by the AFC and MFC models having a single fiber. The effect of the localized stresses on the overall transverse and shear properties are more pronounced for composites with high fiber contents, as shown in Table 3.8. As volume content decreases, the errors also decrease (Tables 3.9-3.10).

Table 3.9 presents the responses at volume fraction 40%. Good comparisons are observed for properties in the axial fiber directions. Similarly, transverse and shear properties show some discrepancies, as discussed above. Comparing with Odegard

model, we could find that the values of G_{23}=G_{13} from the AFC is 16% lower than the Odegard model, G_{12} is 24% lower than the Odegard model, and Y_{11}=$Y_{22,}$ Y_{33}, e_{333}, κ_{11}/κ_o andκ_{33}/κ_o are less than 10% difference with the Odegard model. Comparing with the RVE model, we find that Y_{11}=Y_{22} is 41% higher than the RVE model, G_{12} is 58 % higher than the RVE model, and κ_{11}/κ_o is 45% higher than the RVE model.

Table 3.10 presents responses for composites with volume fraction 20%. Similar observations as the composites with 60 and 40% fiber contents are shown. However, the percentage errors of the properties in the transverse fiber and shear directions decrease. This is due to the decrease in the fiber area, increasing spacing between the fibers and reducing the stress concentration and contact between fibers. Comparing with the Odegard model, we find that the G_{23}=G_{13} is 11% higher than the Odegard model, G_{12} is 20% lower than the Odegard model, and Y_{11}=$Y_{22,}$ Y_{33}, e_{333}, κ_{11}/κ_o andκ_{33}/κ_o are compatible with the Odegard model. Comparing with the RVE model, we could find that Y_{11}=Y_{22} is 14% higher than the RVE model, G_{12} is 21 % higher than the RVE model, and κ_{11}/κ_o is 17% higher than the RVE model.

Table 3.11 presents the effective properties of AFC and MFC having five fibers at volume fraction 40%. Similar results as the single fiber models are observed as discussed above. Comparing Table 3.11 to Table 3.9, we find that the shear moduli, G_{23}=G_{31} and G_{12} of the single fiber model and five fibers model show significant differences. It is due to the prescribed boundary conditions. The single fiber model does not capture shearing between fibers as in the five-fiber model. It makes the single fiber model stiffer compared to the five-fiber model.

Comparing the MFC and AFC models, we find that most properties of the two composite models are similar. However, the transverse moduli $Y_{11}=Y_{22}$ of the MFC and AFC show some discrepancies, which is due to the shape of the fibers. The AFC uses a circular shape fiber and the MFC uses a rectangular shape of fiber. The circular fiber results in smooth variations in the local stresses near the fiber-matrix interphases, minimizing stresses discontinuities. While a rectangular fiber results in sudden jump or discontinuities in stresses at the interphase due to the transverse loading. Because of this reason, the overall AFC has less stiffness in the transverse direction than the MFC. The MFC has higher modulus in the transverse direction than the AFC. The Von Mises stress contour of AFC and MFC due to prescribed σ_{11} is presented in Fig. 3.13.

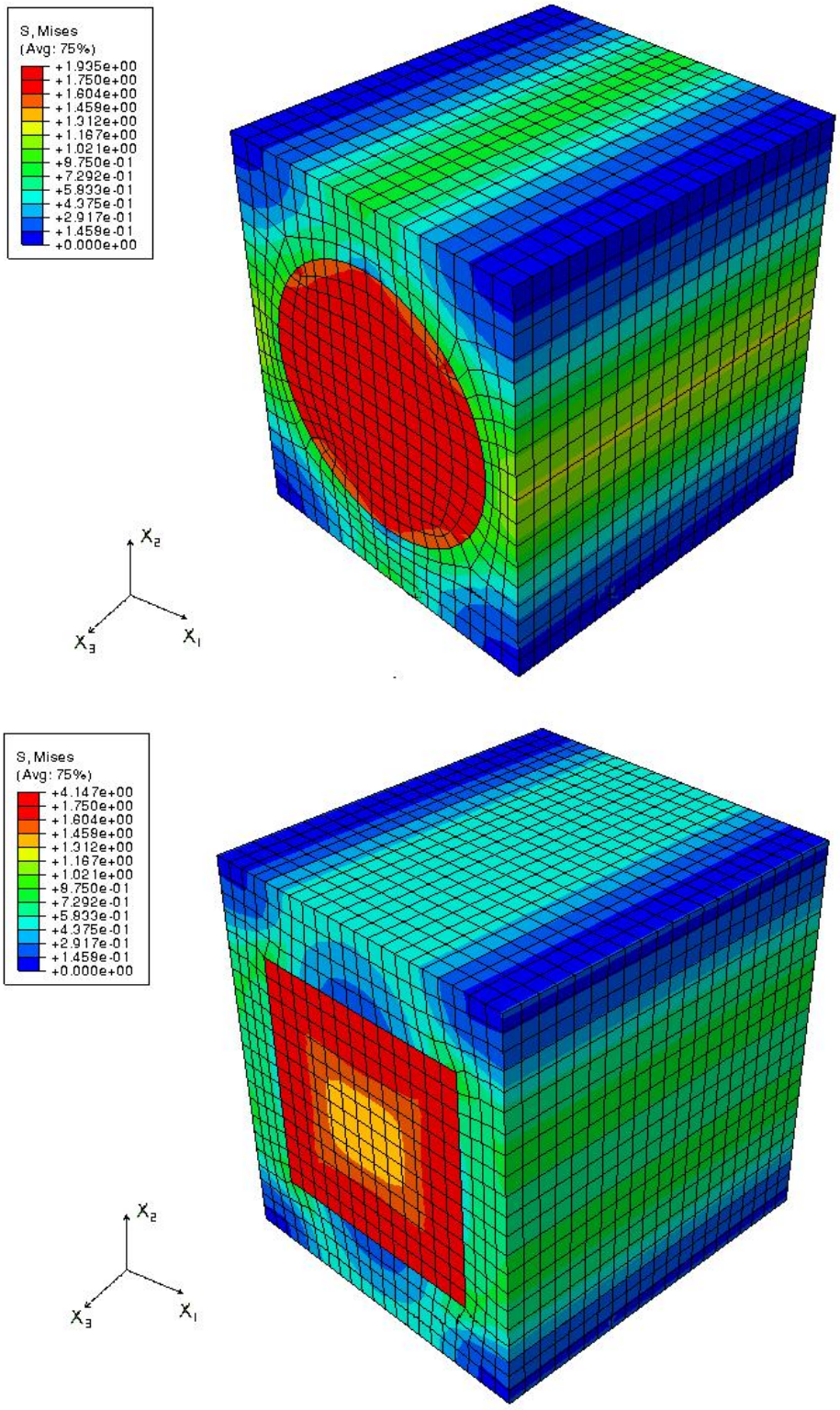

Fig. 3.13 Von Mises Stress Contour due to σ_{11}

Table 3.8 Results of Volume fraction 60

	Odegard Model	AFC model	Error with Odegard value%	RVE Value	Error with RVE value %	MFC Model
Volume fraction%	60			60		60
$Y_{11}=Y_{22}$	17.307	19.736	-14.03	12.103	-63.07	20.186
Y_{33}	50.711	50.994	-0.56	50.106	-1.77	50.942
$G_{23}=G_{13}$	9.181	6.139	33.13	6.213	1.19	5.889
G_{12}	8.207	5.86	30.49	3.617	-57.72	5.77
e_{113}	N/A	0.0914	N/A	N/A	N/A	0.09323
$e_{311}=e_{322}$	N/A	-0.222	N/A	N/A	N/A	-0.217
e_{333}	6.38	6.423	-0.67	6.16	-4.3	6.425
κ_{11}/κ_o	15.89	11.478	27.76	8.7	-31.9	12.89
κ_{33}/κ_o	144.96	142.181	1.9	142.8	0.43	143.55

Table 3.9 Results of Volume fraction 40

	Odegard Model	AFC model	Error with Odegard model%	RVE Value	Error with RVE value %	MFC model
Volume fraction%	40			40		40
$Y_{11}=Y_{22}$	10.045	10.413	-3.66	7.383	-41.04	11.704
Y_{33}	35.098	35.125	-0.08	34.493	-1.83	35.236
$G_{23}=G_{13}$	4.961	4.151	16.33	3.802	-9.18	4.12
G_{12}	4.498	3.444	23.43	2.179	-58.05	3.352
e_{113}	N/A	0.03815	N/A	N/A	N/A	0.0348
$e_{311}=e_{322}$	N/A	-0.112	N/A	N/A	N/A	-0.1014

Table 3.9 Continued

	Odegard Model	AFC model	Error with Odegard model%	RVE Value	Error with RVE value %	MFC model
Volume fraction%	40			40		40
e_{333}	4.29	4.296	-0.14	4.14	-3.77	4.306
κ_{11}/κ_o	8.14	7.549	7.26	5.2	-45.17	6.513
κ_{33}/κ_o	97.29	95.73	1.6	95.9	0.17	95.639

Table 3.10 Results of Volume fraction 20

	Odegard Model	AFC model	Error with Odegard model%	RVE Value	Error with RVE value %	MFC model
Volume fraction%	20			20		20
$Y_{11}=Y_{22}$	6.293	6.223	1.11	5.446	-14.27	6.725
Y_{33}	19.365	19.414	-0.25	18.881	-2.82	19.505
$G_{23}=G_{13}$	2.597	2.301	11.4	2.318	0.73	2.317
G_{12}	2.411	1.918	20.45	1.577	-21.62	1.911
e_{113}	N/A	0.0123	N/A	N/A	N/A	0.0131
$e_{311}=e_{322}$	N/A	-0.037	N/A	N/A	N/A	-0.0376
e_{333}	2.16	2.15	0.46	2.11	-1.9	2.162
κ_{11}/κ_o	4.65	4.565	1.82	3.9	-17.05	4.25
κ_{33}/κ_o	50.38	49.25	2.24	49.5	0.51	49.21

Table 3.11 Results of 5 fibers model

	Odegard Model	AFC model	Error with Odegard model%	RVE Value	Error with RVE value %	MFC model
Volume fraction%	40			40		40
$Y_{11}=Y_{22}$	10.045	10.434	-3.87	7.383	-41.32	11.784
Y_{33}	35.098	35.137	-0.11	34.493	-1.87	35.236
$G_{23}=G_{31}$	4.961	4.002	19.33	3.802	-5.26	4.013
G_{12}	4.498	2.701	39.95	2.179	-23.96	2.627
e_{113}	N/A	0.041	N/A	N/A	N/A	0.03553
$e_{311}=e_{322}$	N/A	-0.0861	N/A	N/A	N/A	-0.0765
e_{333}	4.29	4.304	-4.83	4.16	-3.5	4.315
κ_{11}/κ_o	8.14	8.64	-6.14	5.2	-66.2	6.627
κ_{33}/κ_o	97.29	95.08	2.27	95.9	0.86	99.952

We also compare the effective properties of the AFC and MFC models with other micromechanical models, i.e., Mori-Tanaka and Self-Consistent. Responses of the transverse moduli $Y_{11}=Y_{22}$ of various fiber contents are presented in Fig. 3.14. The predicted values of the AFC and MFC models are between the Self-Consistent and Odegard models. The longitudinal modulus E_{33} is presented in Fig. 3.15. Responses for all micromechanical models agree closely for the entire fiber volume fractions.

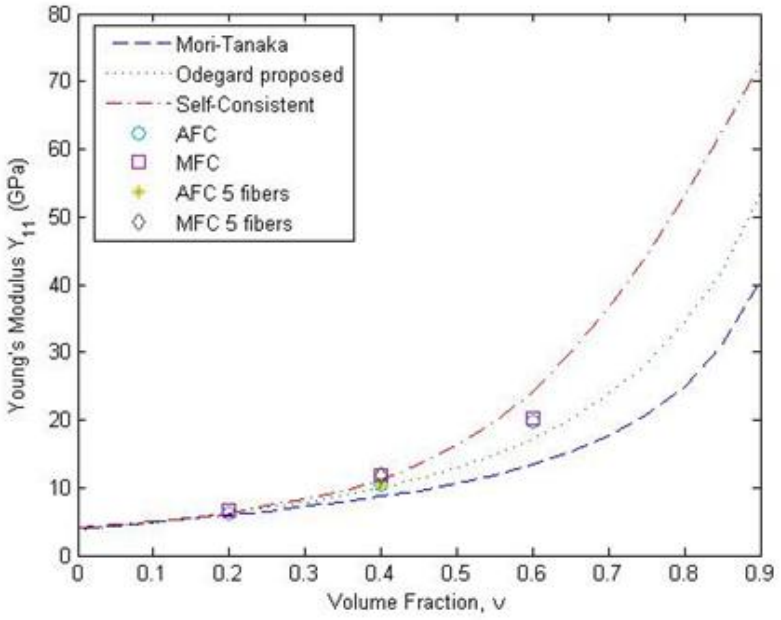

Fig. 3.14 Effective elastic modulus Y_{11}

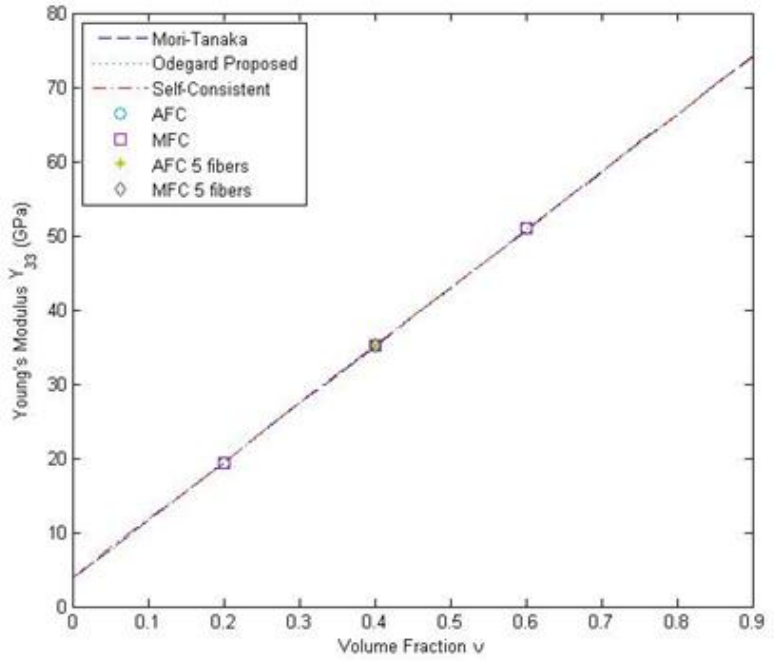

Fig. 3.15 Effective elastic modulus Y_{33}

Figure 3.16 presents the effective shear moduli G_{23}=G_{13}. In Fig. 3.16, we find that the AFC and MFC models are closer to the Mori-Tanaka model. The Self-Consistent model over predicts the longitudinal shear modulus for composites with fiber contents greater than 0.2. Figure 3.17 presents shear modulus G_{12}. The AFC and MFC models show lower values than other micromechanical models and are closer to the Mori-Tanaka model. The Self-Consistent model over predicts the transverse shear modulus for composites with fiber contents greater than 0.2.

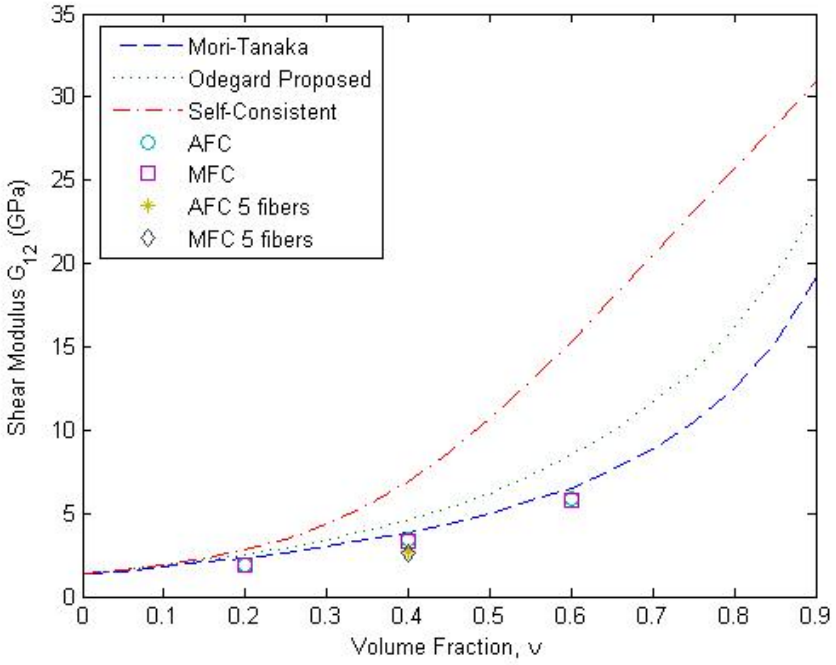

Fig. 3.16 Effective shear modulus G_{12}

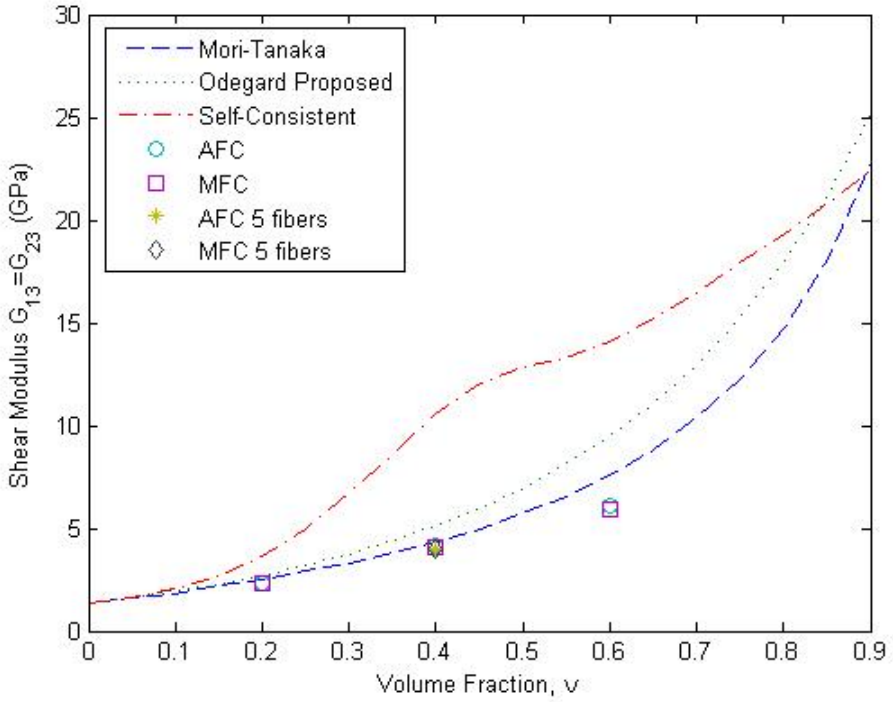

Fig. 3.17 Effective shear modulus $G_{13}=G_{23}$

Figure 3.18 presents the prediction of the piezoelectric constant e_{311}. We observe that the AFC and MFC models agree with the Odegard and Mori-Tanaka models. The Self-Consistent model under predicts the piezoelectric constant e_{311} for composites with fiber content greater than 0.4. Figure 3.19 shows responses of e_{333} for all models. All models show good agreement. Figure 3.20 shows responses of e_{113}. The AFC and MFC models, the Odegard, and Mori-Tanaka models agree for the fiber volume fractions. The Self Consistent model over-predicts the piezoelectric constant e_{113} for composites with fiber content greater than 0.3.

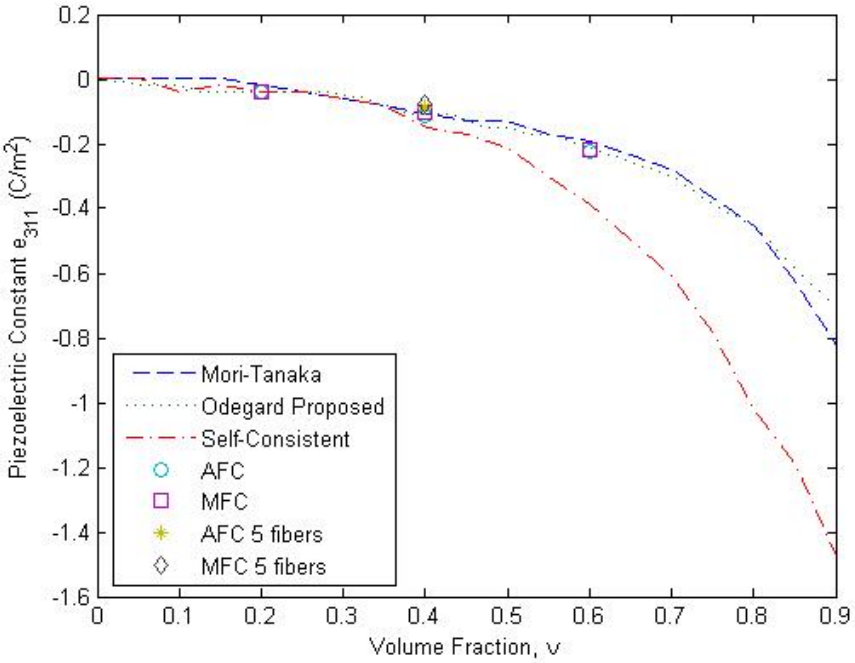

Fig. 3.18 Effective piezoelectric constant e_{311}

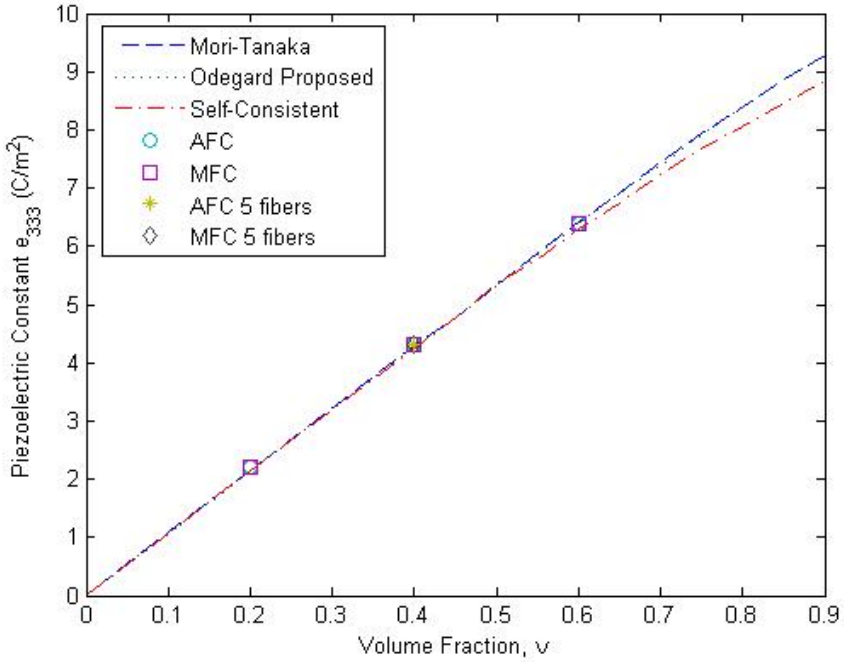

Fig. 3.19 Effective piezoelectric constant e_{333}

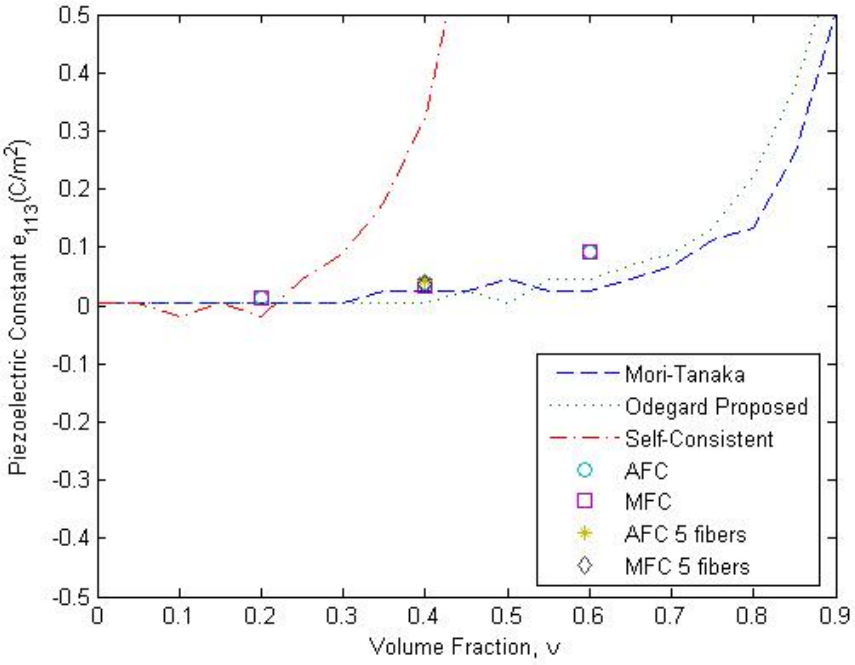

Fig. 3.20 Effective piezoelectric constant e_{113}

Figure 3.21 presents the transverse dielectric constant κ_{11}/κ_o. Responses from the AFC and MFC models agree with the Mori-Tanaka and Odegard models for the entire range of fiber volume fractions. The Self Consistent model over-predicts the transverse dielectric constant for composites with fiber contents greater than 0.4. Figure 3.22 presents the axial dielectric constant κ_{33}/κ_o. The results show that all micromechanical models agree well.

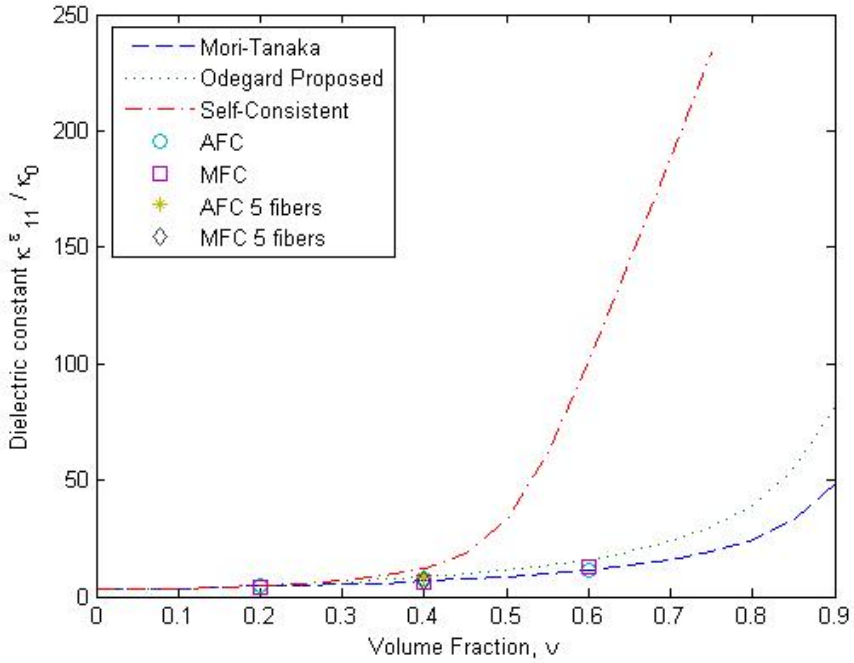

Fig. 3.21 Effective dielectric constant $\kappa^{\varepsilon}_{11}/\kappa_o$

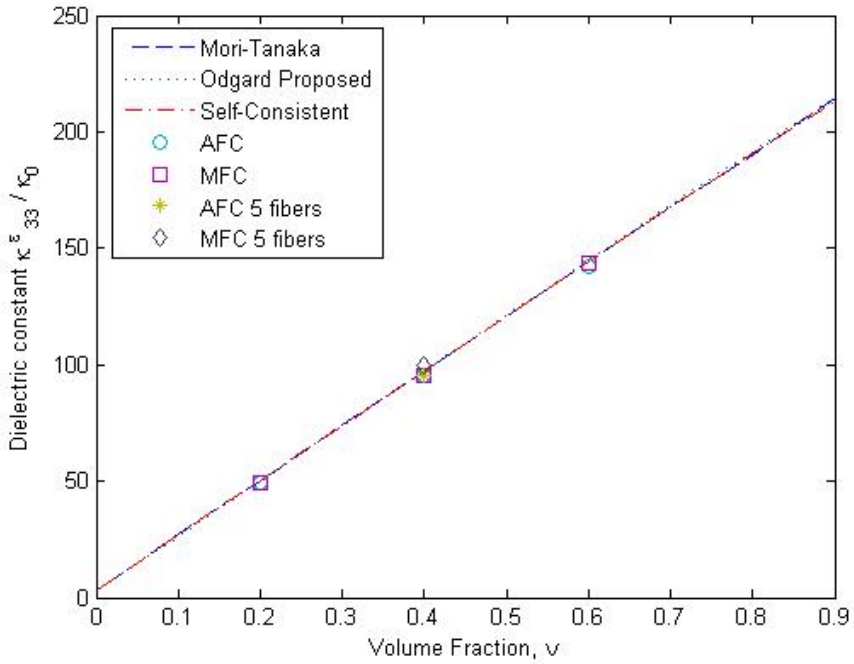

Fig. 3.22 Effective dielectric constant$\kappa^{\varepsilon}_{33}/\kappa_o$

It is seen that for the electro-mechanical and piezoelectric properties along the longitudinal fiber direction, all micromechanical models are in good agreement. This indicates that the effective properties for long unidirectional fiber composites along the longitudinal fiber axis are independent on the shape, size, and arrangement of the fibers in the matrix medium, but they mainly depend on the fiber volume contents and constituent properties. All properties in the transverse fiber directions predicted by the different micromechanical models are in good agreement for composites with lower fiber volume contents, i.e., less than 40% fiber contents. At higher fiber volume contents, some mismatches are observed. This might be due to an existence of localized field variables, i.e., stress, electric field, in the matrix constituents between the fiber spacing when the composites are loaded in the transverse fiber directions. As fiber contents increase, the spacing between the fibers decreases, resulting in higher localized field variables, whose magnitudes and distributions strongly depend on the shape, size, and arrangements of the fibers. Observing the shear properties, all micromechanical models show some mismatches even at low fiber contents (less than 20%). This condition is expected, since performance of heterogeneous materials subject to shear boundary conditions is strongly influenced by microstructural arrangements of the constituents.

3.3.2 RESPONSE OF PZT-5A / EPOXY

The effective properties of PZT-5A/epoxy composites generated using the presented micromechanical models are compared to experimental data of Nelson et al. [3]. Responses of the AFC and MFC models are given in Tables 3.12 and 3.13,

respectively. The coupling coefficient k_{33} between the properties measured at short-circuit and open-circuit is given as:

$$k_{33}^2 = \frac{d_{333} d_{333}}{S_{3333}^E \kappa_{33}^\sigma}$$

$$S_{3333}^D = (1 - k_{33}^2) S_{3333}^E \tag{3.10}$$

Where k_{33} is the coupling coefficient, S_{3333}^D is the compliance measured at constant electrical displacement, S_{3333}^E is the compliance measured at constant electrical field.

Figures 3.23 to 3.28 compare the effective responses from the AFC and MFC micromodels and the experimental data. Figure 3.23 presents the response of the axial compliance S^E_{3333}. The prediction results agree with the experimental data. Figure 3.24 presents responses of the piezoelectric constant d_{311}, which shows good agreement with the experimental data. Figure 3.25 presents responses of the piezoelectric constant d_{333}. It is seen that the AFC and MFC predictions are close to the experimental data. Figure 3.26 presents response of the axial dielectric constant κ_{33}/κ_o. It is seen that the AFC and MFC predictions are close to the experimental data. Figure 3.27 presents responses of the coupling coefficient k_{33}. Figure 3.28 presents responses of the axial compliance S^D_{3333}. The AFC and MFC models agree with the experimental data for the volume fractions.

Table 3.12 AFC modeling results

Type	AFC			
Fiber Volume fraction%	20	40	40(5 fiber)	60
$S^E_{3333}(10^{-12}Pa^{-1})$	66.1	36.1	36.1	24.8
$d_{311}(10^{-12}CN^{-1})$	-85.7	-94.6	-94.5	-98.3
$d_{333}(10^{-12}CN^{-1})$	225.9	247.8	247.6	256.1
κ_{33}/κ_o	284.7	581.6	581.6	879.5
k_{33}	0.55	0.57	0.57	0.58
$S^D_{3333}(10^{-12}Pa^{-1})$	46.1	24.4	24.4	16.5

Table 3.13 MFC modeling results

Type	MFC			
Fiber Volume fraction	20	40	40(5 fiber)	60
$S^E_{3333}(10^{-12}Pa^{-1})$	65.7	36	36	24.8
$d_{311}(10^{-12}CN^{-1})$	-85.8	-94.6	-94.6	-98.2
$d_{333}(10^{-12}CN^{-1})$	226.1	247.9	247.8	255.6
κ_{33}/κ_o	284.7	581.9	581.9	876.9
k_{33}	0.56	0.58	0.58	0.58
$S^D_{3333}(10^{-12}Pa^{-1})$	45.1	23.9	23.9	16.5

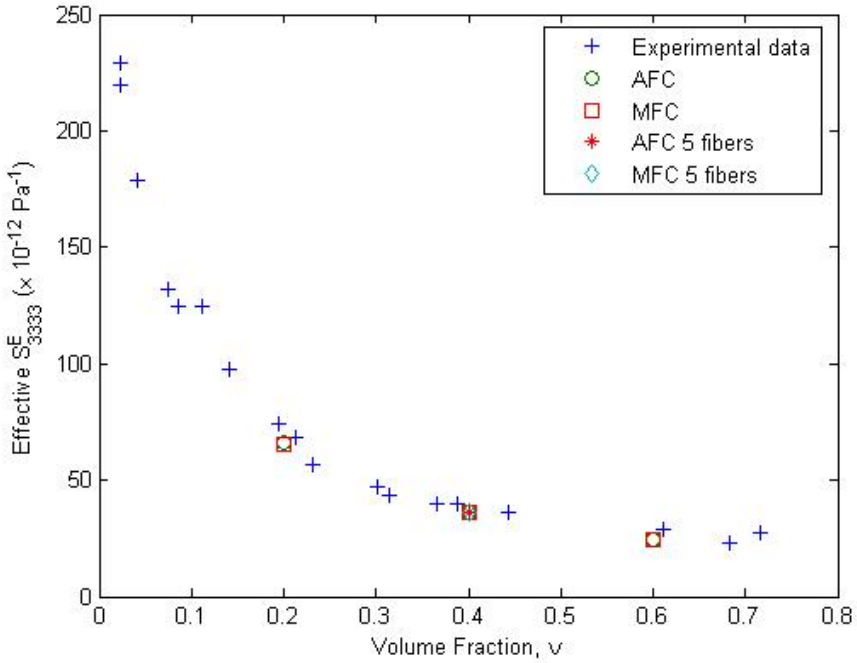

Fig. 3.23 Effective compliance S^E_{3333}

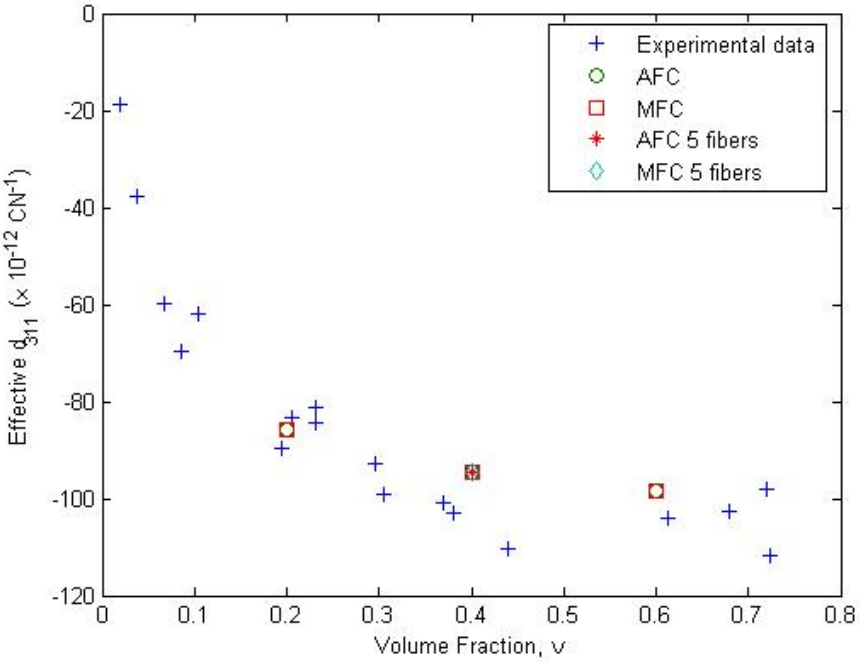

Fig. 3.24 Effective piezoelectric constant d_{311}

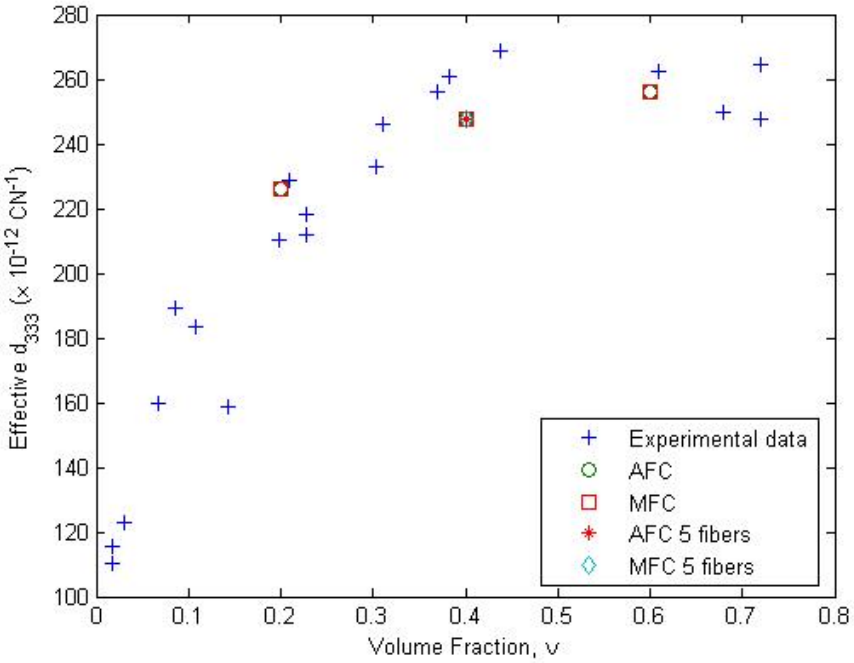

Fig. 3.25 Effective piezoelectric constant d_{333}

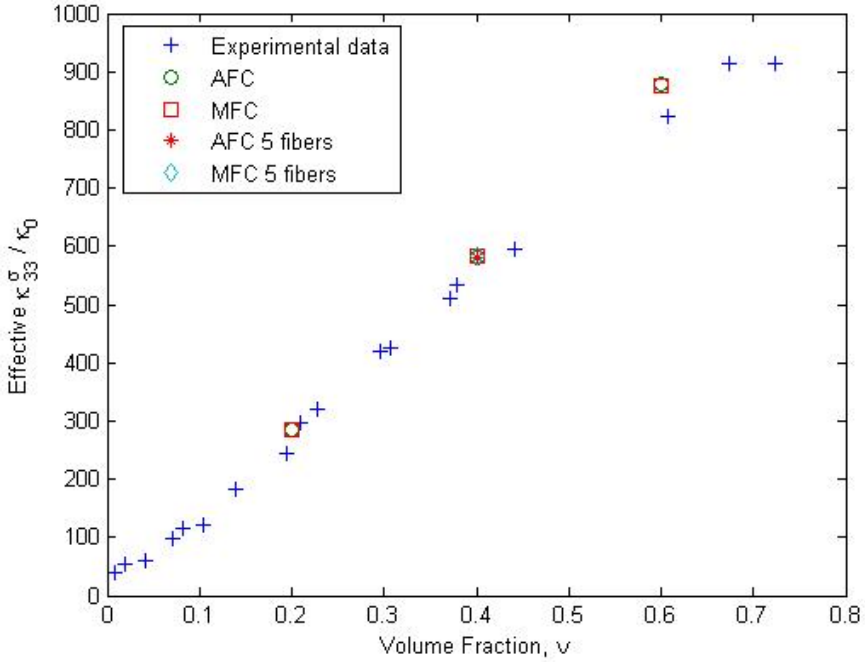

Fig. 3.26 Effective dielectric constant $\kappa^{\sigma}_{33}/\kappa_o$

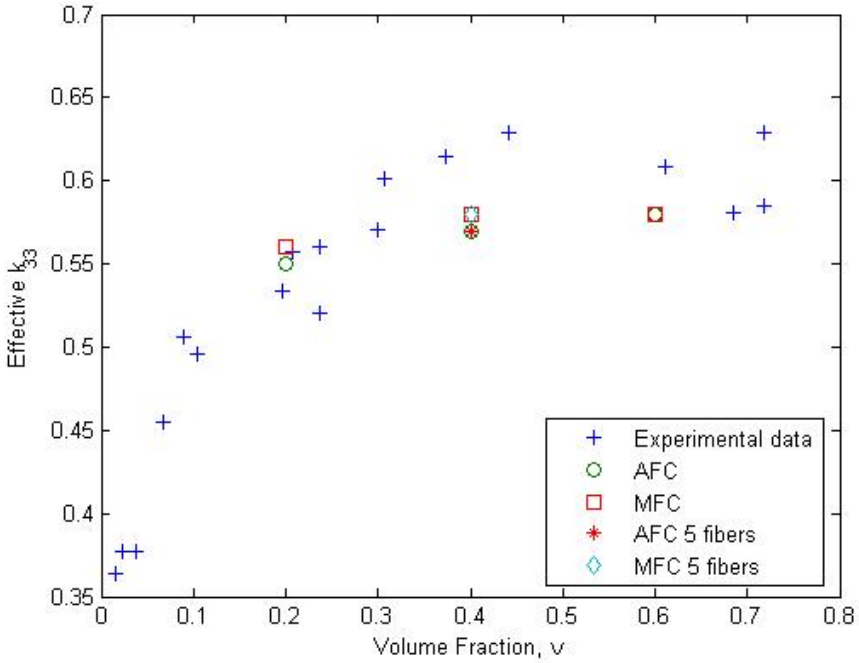

Fig. 3.27 Effective coupling coefficient k_{33}

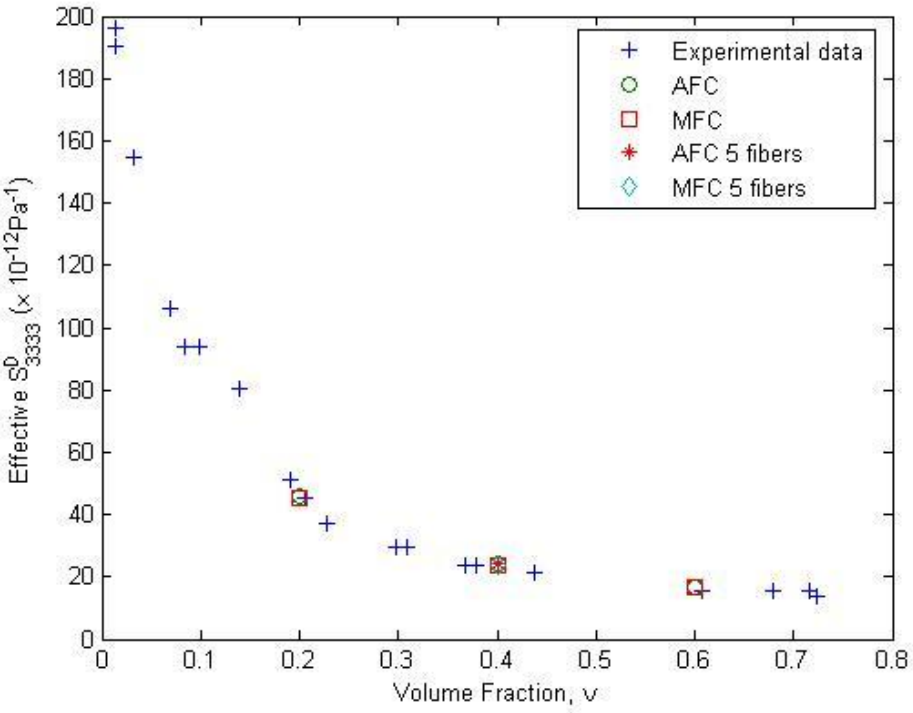

Fig. 3.28 Effective compliance S^D_{3333}

3.4 EFFECTS OF VISCOELASTIC MATRIX AT ELEVATED TEMPERATURES ON THE EFFECTIVE PROPERTIES OF AFC AND MFC

PFC is a piezo composite consisting of piezoelectric fibers and epoxy matrix. Piezoelectric ceramic has high stiffness and shows mild creep at room temperature, while at elevated temperatures ceramics could experience significant time-dependent behaviors. Fett and Thun [29] conducted creep tests on unpoled and poled PZT ceramics at room temperature under different stresses. Non-negligible creep strains are observed and the creep responses are more pronounced at higher stresses. Heiling and Hardtl [23] showed that the electric and piezoelectric responses of PZT materials change with time under constant stresses. PFCs are often utilized for applications under high mechanical and electrical stimuli. The driving voltage of PFCs can take up to +1500 V. Under such condition, significant amount of heat could be generated increasing the temperatures of the PFCs. At elevated temperatures, materials, especially polymers, show significant time-dependent behaviors. To better understand responses of PFCs at high applied stress-and voltage and elevated temperatures, we investigate and discuss the time-dependent behavior of PFC. It is noted that the time-dependent effect is often significant at elevated temperature and its behavior at room temperature is usually neglected.

We use the micromechanical models of AFC and MFC with viscoelastic properties for the matrix. We apply constant stress and charge to observe the variations of the effective compliance, piezoelectric constants and permittivity with time. The studied AFC and MFC have PZT fibers and LaRC-SI matrix constituents. Viscoelastic data for

LaRC-SI at 213℃ to 223℃ are obtained from Nicholson et al[31]. Temperature 218℃ is taken as the reference temperature.

3.4.1 PROPERTIES OF LARC-SI

Nicholson et al.[31] used Kolrausch – Williams - Watts (KWW) model to express the time-dependent compliance of LaRC-SI at different temperatures. The KWW model is expressed as:

$$S(t) = Soe^{\left(\frac{t}{\tau}\right)^{\beta}} \tag{3.11}$$

Table 3.14 presents material parameters in the KWW model at various temperatures.

Table 3.14 Viscoelastic parameter of LaRC-SI[31]

$\bar{M}_w$(g/mol)	T_{test}(℃)	ΔT(℃)	S_O(GPa^{-1})	τ(s)	β
24290	213	25	0.375	8.51E+0.5	0.375
	218	20	0.371	3.21E+0.5	0.411
	223	15	0.313	1.52E+0.5	0.403

Where So is the initial compliance, t is the current time, τ is the retardation time, β is the parameter, which influences the shape of the creep compliance, $\bar{M}_w$ is the average of the molecular weight, T_{test} is the testing temperature and ΔT is the difference between the

testing temperature and glass transition temperature. At the reference temperature 218℃, the time-dependent compliance is:

$$S(t) = Soe^{\left(\frac{t}{\tau}\right)^{\beta}} = 0.371e^{\left(\frac{t}{32100}\right)^{0.411}} \tag{3.12}$$

User subroutine USDFLD is used to incorporate the time-dependent properties in the C3D8E element in the FE micromechanical models. In order to determine the relaxation modulus of LaRC-SI from the compliance data, Laplace transform is used and the relation between compliance and modulus in the Laplace domain for a linear viscoelastic material is given as:

$$S(s)Y(s) = \frac{1}{s^2} \tag{3.13}$$

A polynomial function is then used to represent the time-dependent compliance in Eq. (3.12) and the Laplace transform is performed on the polynomial function, which are:

Polynomial Fit

$$S(t) = -(2.07E-012)t^2 + (2.329E-006)t + 0.468 \tag{3.14}$$

Laplace Transform

$$S(s) = \frac{-4.139E-012}{s^3} + \frac{2.329E-006}{s^2} + \frac{0.468}{s} \tag{3.15}$$

The relaxation modulus is now given as:

$$Y(t) = 1.752\mathrm{e}^{-6.362\mathrm{E}-006\mathrm{t}} + 0.383\mathrm{e}^{1.389\mathrm{E}-006\mathrm{t}} \tag{3.16}$$

The exponential and polynomial functions for the compliance are shown in Fig. 3.29. The plot of the relaxation modulus Eq. 3.16 is given in Fig. 3.30.

We first use a one-element model to verify the implementation of the time-dependent modulus calculated from the above equations in the FE model. A cubic FE model is generated using a solid element C3D8E as shown in Fig. 3.31. User subroutine, USDFLD is used to incorporate the relaxation modulus. USDFLD is a subroutine that allows users to define properties at a material point as functions of time or any other field variables. Here, we define the elastic modulus of LaRC-SI that changes with time. We apply a constant stress and a constant strain to observe the creep and relaxation responses, respectively. The results are presented as follows.

We first apply a constant stress in the x_1 direction. The strain responses from the FE model are presented in Fig. 3.32. Next, we prescribe a constant strain and the relaxation responses are shown in Fig. 3.33. Responses from the FE models are compared to the analytical expressions in Eqs. 3.12, 3.14 and 3.16. Creep responses from the three functions are given in Fig. 3.34. The error function between the creep compliance (Fig. 3.35) obtained from the FE analysis and analytical solution is defined as:

$$Error = \frac{FEM - compared\ function}{compared\ function} \times 100\% \tag{3.17}$$

Next, we compare the relaxation moduli obtained from the polynomial function and FEM result in Fig. 3.36. The error function is calculated and presented in Fig 3.37.

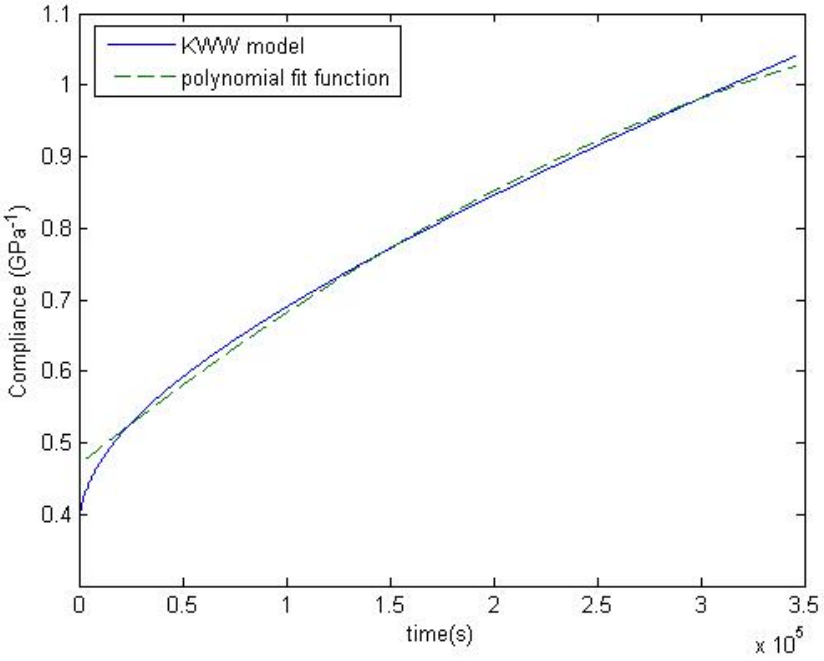

Fig. 3.29 Creep compliance for LaRC-SI

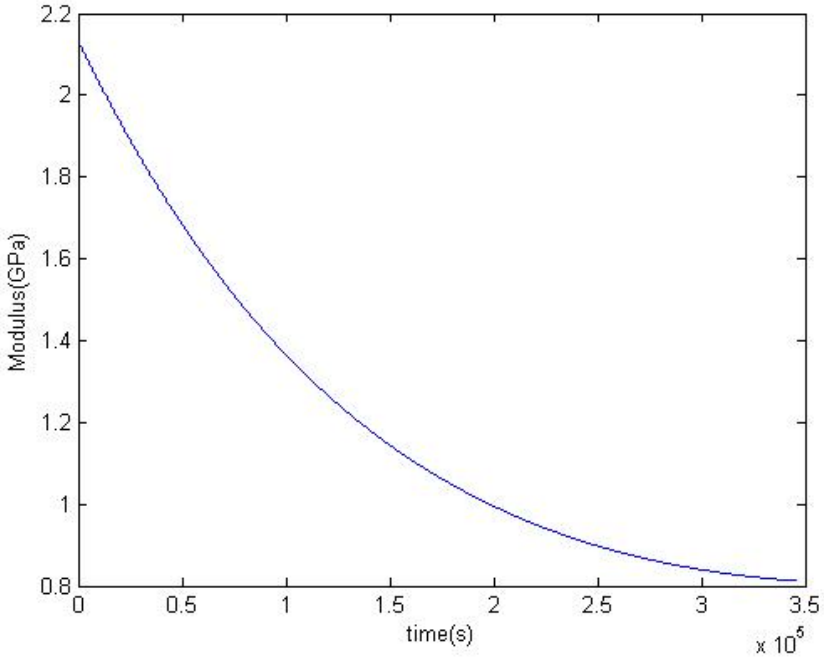

Fig. 3.30 Relaxation modulus for LaRC-SI

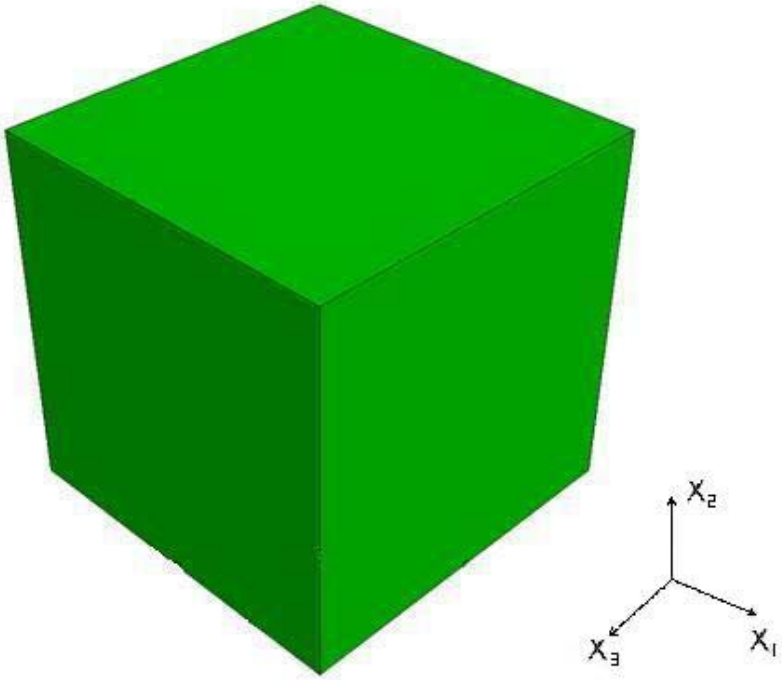

Fig. 3.31 ABAQUS finite element model.

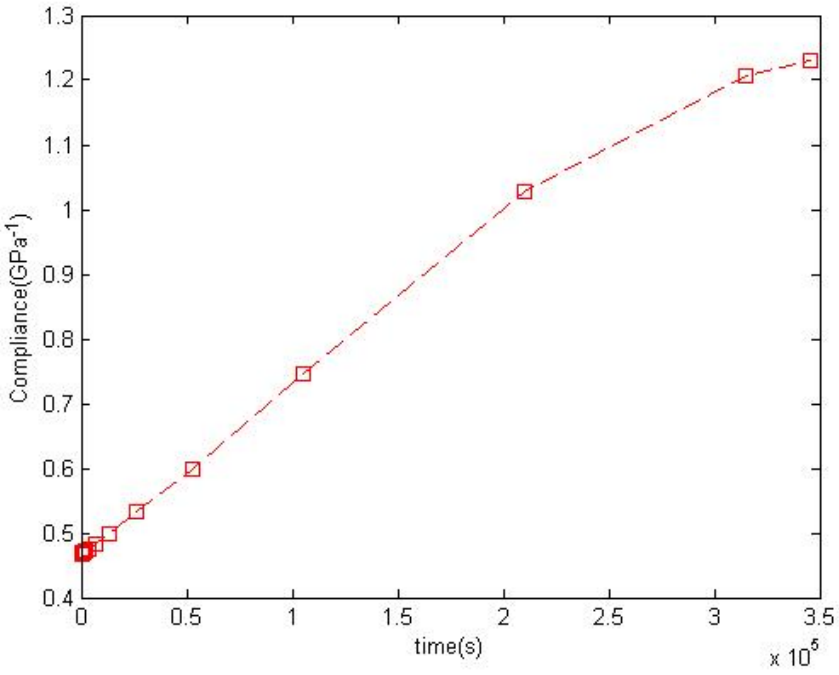

Fig. 3.32 Creep compliance from the FE analysis

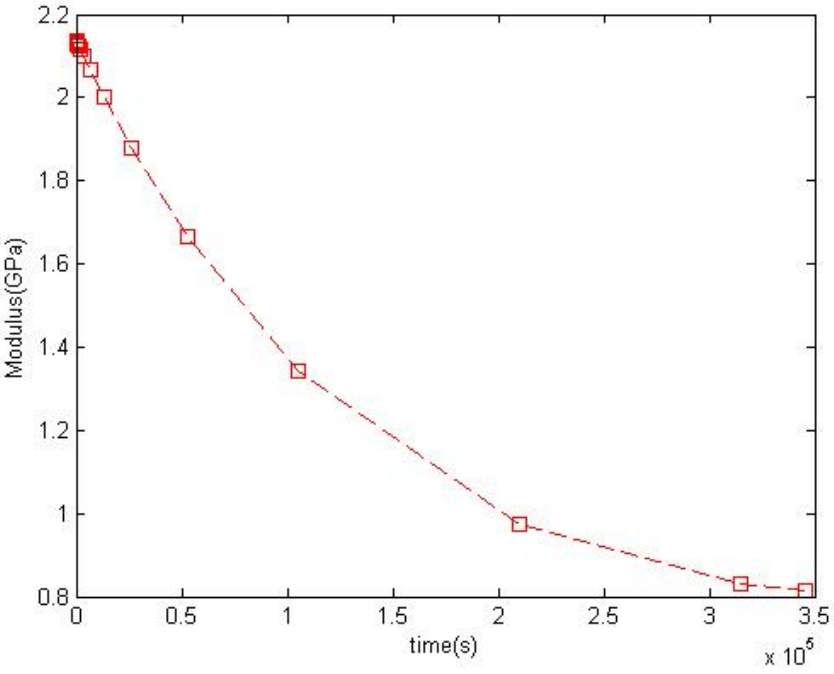

Fig. 3.33 Relaxation modulus from FE analysis

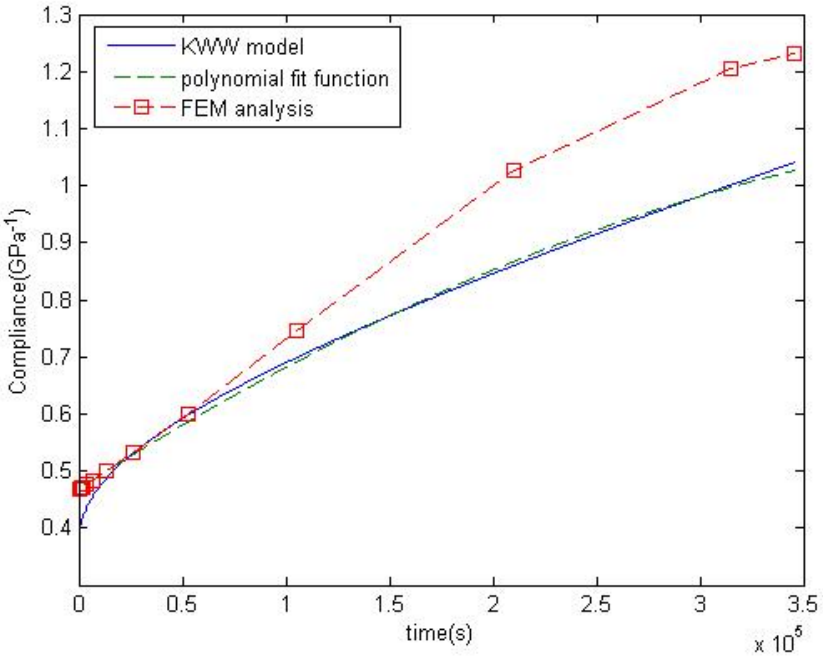

Fig. 3.34 Comparing creep result

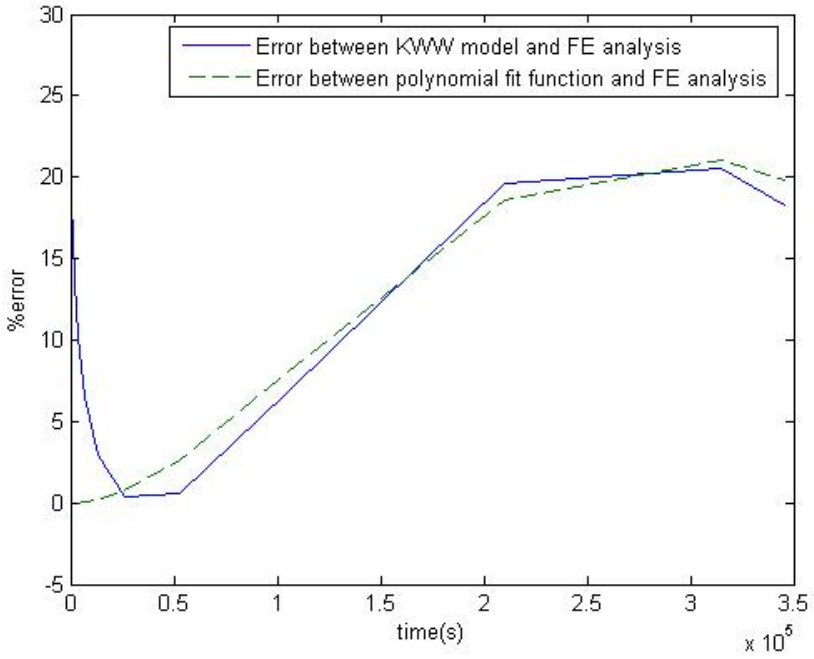

Fig. 3.35 Error function of creep

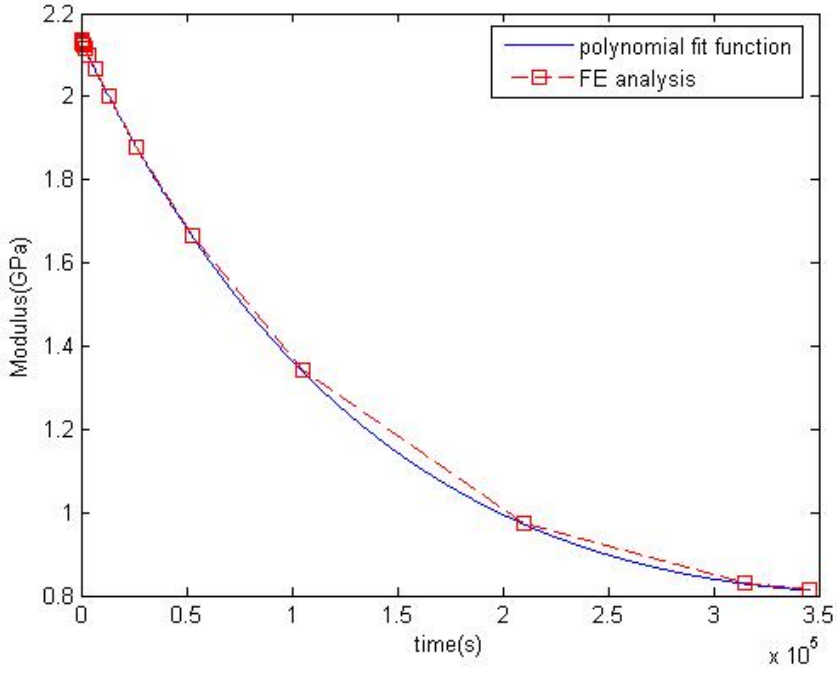

Fig. 3.36 Comparing relaxation result

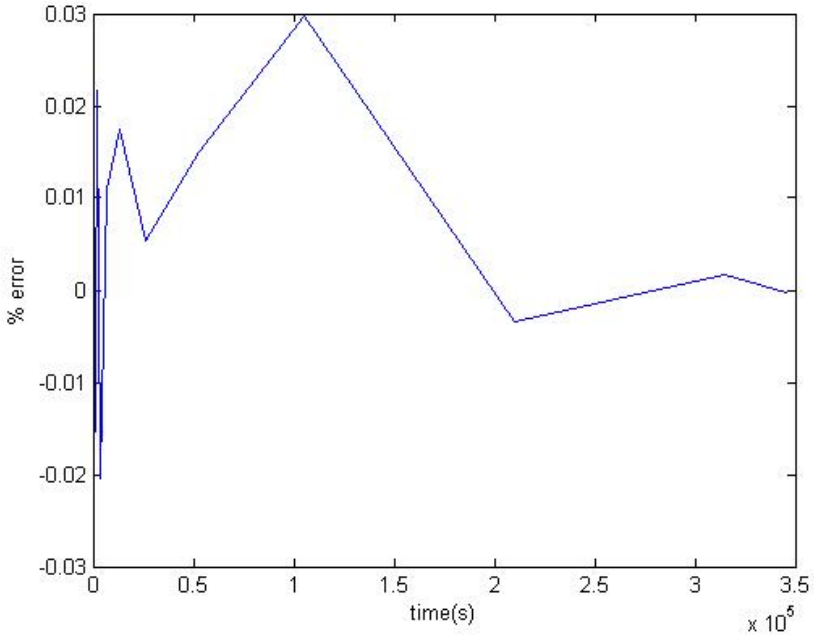

Fig. 3.37 Error function of relaxation

Figure 3.35 presents the error between the KWW model and FE analysis and the error between the polynomial function and the FE analysis of the creep compliance. We found that the error is within 10% from the initial time up to 15000s and the error increases to 20% after 25000s. Figure 3.37 presents the error between the polynomial function and the FE analysis for the relaxation modulus, which show less than 0.03% error. The significant mismatches in the compliance from the FE analysis are due to the time-dependent properties that are given for the modulus via the USFLD subroutine. In determining the compliance, the FE analyses take value of $\frac{1}{Y(t)}$, which is not the correct time-dependent compliance for viscoelastic materials. The relation between the compliance and modulus for linear viscoelastic material is given in Eq. 3.13. This is why the FE analysis results in error prediction of the compliance.

From above discussion, the USFLD subroutine in FE analysis is valid for analyzing relaxation responses, but not for the creep responses. One way to solve this problem is using UMAT subroutine to incorporate material properties in the FE analysis. However, the element C3D8E that we used in the FE models does not support the UMAT subroutine. One could develop a user defined element (UEL) in the FE model to overcome this issue. However, the development of UEL is beyond the scope of this study.

3.4.2 PROPERTIES OF PZT-7A

Since the viscoelastic properties of LaRC-SI are available at elevated temperatures, the properties of PZT-7A should be obtained at those elevated temperatures. However, only limited properties of PZT-7A are available at high temperatures which are the dielectric constant $\frac{\kappa_{33}^{\sigma}}{\kappa_o}$, and piezoelectric constant d_{311}. The rest of the mechanical and electrical properties of PZT-7A are available at room temperature. In order to perform time-dependent analyses of AFC and MFC, two assumptions are made for the remaining electro-mechanical properties of the PZT-7A. The first assumption is taking all other properties reported at room temperature as constant values and only $\frac{\kappa_{33}^{\sigma}}{\kappa_o}$ and d_{311} vary with temperatures. For the second assumption, we take the mechanical properties (Young's modulus and shear modulus) as reported at room temperature but the remaining piezoelectric constants and dielectric

constants are temperature dependent that are proportional to those of $\frac{\kappa_{33}^{\sigma}}{\kappa_o}$ and d_{311} values.

Assumption 1

We assume only the permittivity $\frac{\kappa_{33}^{\sigma}}{\kappa_o}$ and piezoelectric constant d_{311} vary with temperatures. Other properties remain unchanged. We use e_{311}, e_{322}, e_{333}, e_{113}, $\frac{\kappa_{33}^{\epsilon}}{\kappa_o}$ and $\frac{\kappa_{11}^{\epsilon}}{\kappa_o}$ in our FE model, which is suitable for the relaxation behaviors. We first relate the piezoelectric and dielectric properties $\frac{\kappa_{33}^{\sigma}}{\kappa_o}$ and d_{311} into the properties at a proper temperature. At 218℃, $d_{311} = -130.5 \times 10^{-12} C/N$ and $\frac{\kappa_{33}^{\sigma}}{\kappa_o} = 1463.1$. The other properties of fibers are constant (Eqs. 3.18-3.19). In FE ABAQUS software, we choose type S piezoelectricity to perform the analysis. We transfer the above piezoelectric and dielectric properties into e_{ijk} and $\frac{\kappa_{ij}^{\varepsilon}}{\kappa_o}$. We use relations in Eq. 3.19 and Eq. 3.20 to determine e_{ijk} and $\frac{\kappa_{ij}^{\varepsilon}}{\kappa_o}$, which are given in Eq. 3.22 and Eq. 3.23. The piezoelectric and dielectric properties at room and elevated temperatures are compared in Tables 3.15 and 3.16.

$$d\left(\frac{C}{N}\right) = \begin{bmatrix} 0 & 0 & 0 & 0 & 362 & 0 \\ 0 & 0 & 0 & 362 & 0 & 0 \\ \mathbf{-130.5} & \mathbf{-130.5} & 150 & 0 & 0 & 0 \end{bmatrix} \times 10^{-12} \quad (3.18)$$

$$\frac{\kappa^{\sigma}}{\kappa_o} = \begin{bmatrix} 840 & 0 & 0 \\ 0 & 840 & 0 \\ 0 & 0 & \mathbf{1463.1} \end{bmatrix} \quad (3.19)$$

$$e = d_{imn} C^E_{mnjk} \tag{3.20}$$

$$\kappa^{\epsilon}_{ij} = \kappa^{\sigma}_{ij} - d_{imn} C^E_{mnkl} d_{jkl} = \kappa^{\sigma}_{11} - d_{113} C^E_{1313} d_{113}$$

$$\kappa^{\epsilon}_{ij} = \kappa^{\sigma}_{ij} - d_{imn} C^E_{mnkl} d_{jkl} = \kappa^{\sigma}_{33} - d_{311} C^E_{1111} d_{311} - d_{311} C^E_{1122} d_{322} - d_{311} C^E_{1133} d_{333} - d_{322} C^E_{2211} d_{311} - d_{322} C^E_{2222} d_{322} - d_{322} C^E_{2233} d_{333} - d_{333} C^E_{3311} d_{311} - d_{333} C^E_{3322} d_{322} - d_{333} C^E_{3333} d_{333} \tag{3.21}$$

$$e_{ijk} = \begin{bmatrix} 0 & 0 & 0 & 0 & 9.2 & 0 \\ 0 & 0 & 0 & 9.2 & 0 & 0 \\ -18.1281 & -18.1281 & 0.2838 & 0 & 0 & 0 \end{bmatrix} \tag{3.22}$$

$$\frac{\kappa^{\epsilon}}{\kappa_o} = \begin{bmatrix} 460 & 0 & 0 \\ 0 & 460 & 0 \\ 0 & 0 & \mathbf{923.9} \end{bmatrix} \tag{3.23}$$

Table 3.15 Comparing piezoelectric constant in assumption1

	$e_{311}\left(\frac{C}{m^2}\right)$	$e_{322}\left(\frac{C}{m^2}\right)$	$e_{333}\left(\frac{C}{m^2}\right)$	$e_{113}\left(\frac{C}{m^2}\right)$
Room Temp	-2.1	-2.1	9.5	9.2
High Temp	-18.1	-18.1	0.3	9.2

Table 3.16 Comparing dielectric constant in assumption1

	$\frac{\kappa_{11}^{\epsilon}}{\kappa_o}$	$\frac{\kappa_{22}^{\epsilon}}{\kappa_o}$	$\frac{\kappa_{33}^{\epsilon}}{\kappa_o}$
Room Temp	460	460	235
High Temp	460	460	923.9

Assumption 2

The permittivity $\frac{\kappa_{33}^{\sigma}}{\kappa_o}$ and piezoelectric constant d_{311} change with temperatures and all other properties vary with temperatures in the same way as the permittivity $\frac{\kappa_{33}^{\sigma}}{\kappa_o}$ and piezoelectric constant d_{311}. We use the relations in Eq. 3.20 and Eq. 3.21 to determine e_{ijk} and $\frac{\kappa_{ij}^{\varepsilon}}{\kappa_o}$, which are presented in Eq. 3.24 and Eq. 3.25. We compare their values in Table 3.17 and Table 3.18.

$$e_{ijk} = \begin{bmatrix} 0 & 0 & 0 & 0 & 20 & 0 \\ 0 & 0 & 0 & 20 & 0 & 0 \\ -5.1 & -5.1 & 23.4 & 0 & 0 & 0 \end{bmatrix} \tag{3.24}$$

$$\frac{\kappa^{\epsilon}}{\kappa_o} = \begin{bmatrix} 1113.4 & 0 & 0 \\ 0 & 1113.4 & 0 \\ 0 & 0 & 453 \end{bmatrix} \tag{3.25}$$

Table 3.17 Comparing piezoelectric constant in assumption2

	$e_{311}\left(\frac{C}{m^2}\right)$	$e_{322}\left(\frac{C}{m^2}\right)$	$e_{333}\left(\frac{C}{m^2}\right)$	$e_{113}\left(\frac{C}{m^2}\right)$
Room Temp	-2.1	-2.1	9.5	9.2
High Temp	-5.1	-5.1	23.4	20

Table 3.18 Comparing dielectric constant in assumption2

	$\frac{\kappa_{11}^{\epsilon}}{\kappa_o}$	$\frac{\kappa_{22}^{\epsilon}}{\kappa_o}$	$\frac{\kappa_{33}^{\epsilon}}{\kappa_o}$
Room Temp	460	460	235
High Temp	1113.4	1113.4	453

3.4.3 TIME-DEPENDENT ELECTRO-MECHANICAL RESPONSES OF AFC AND MFC

Results from the assumption 1

We present the time-dependent responses of AFC and MFC with fiber volume fractions of 20%, 40% and 60%. Figure 3.38 illustrates the creep compliance in the transverse direction. Composites with smaller fiber volume fractions exhibit more pronounced creep than the ones with higher fiber contents. This is due to the higher stresses in the epoxy that increase the overall creep behavior. Moreover, the AFC models creep 10% higher than the MFC model for fiber volume fractions 20% and 40%. This is due to the round shape of fiber that results in a more flexible system allowing more shear deformation in the matrix. The rectangular fibers provide higher resistant to the

transverse loading. Responses also show that the five-fiber models agree with the single fiber models. Figure 3.39 presents the creep compliance in the axial fiber direction. For composites with volume fractions 40% and 60%, insignificant creep is shown because most of the stress is carried by the PZT fibers.

Figure 3.40 presents the time-dependent shear compliance S_{2323}. We find a similar condition as in Fig 3.39 that the models at fiber volume fraction 40% and 60% show insignificant creep. The five-fiber models agree with the single fiber models. Moreover, we find that the AFC model creep more than the MFC model at 20% fiber volume fraction which is due to the shape of the fiber. Figure 3.41 presents the shear creep compliance S_{1212}. More pronounced creep behaviors are observed in all composites.

Figure 3.42 presents time-dependent responses for piezoelectric constant d_{311}. Piezoelectric constant relaxes more in composites at low fiber volume fractions than those at high fiber volume fractions. Figure 3.43 presents creep in piezoelectric constant d_{333}, which show significant creep at 20% fiber content. Responses of the AFC and MFC with single and five fiber models are also in agreement. Figure 3.44 presents creep in the piezoelectric constant d_{113}. We find that piezoelectric constant d_{113} in MFC model is higher than that of the AFC model at 60% fiber volume fraction. Moreover, d_{113} value in the five-fiber AFC model is higher than the ones of MFC at fiber volume fraction 40%. Similar conditions are exhibited in the transverse dielectric constants κ_{11}/κ_o (Fig. 3.44). In relations Eq. 3.6 and Eq. 3.7, we extract d_{113} and κ_{11}/κ_o by assuming a constant electrical field. In table 3.2, we know that the behaviors of these models are shear behaviors. The shear behavior results in non-uniform distribution of the electric field as illustrated in Fig

3.47. We determine the average electric field by summing all electric field at integration points in the FE micromechanical models.

Fig. 3.45 presents response of the transverse dielectric constants κ_{11}/κ_o. We find that the dielectrics constant is unaffected by the viscoelastic matrix. Figure 3.46 presents responses of axial dielectric constants κ_{33}/κ_o.

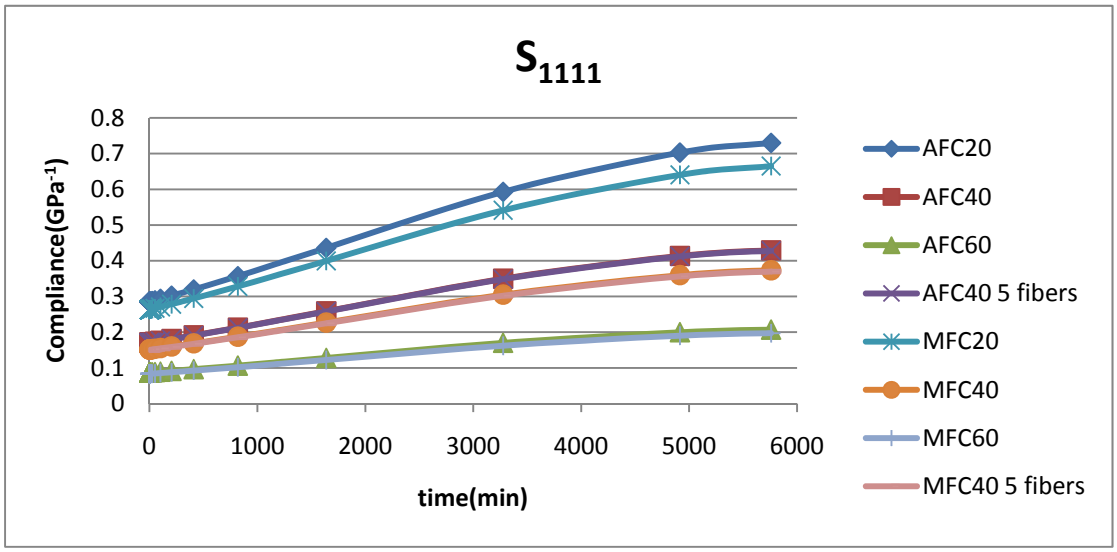

Fig. 3.38 Effective compliance in transverse direction S_{1111} in assumption 1

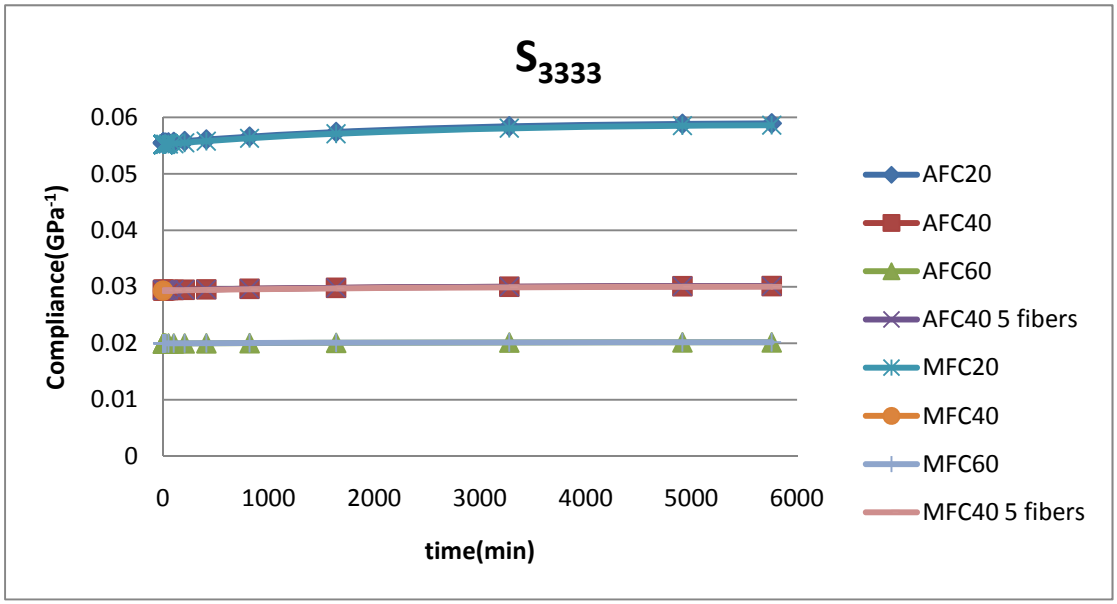

Fig. 3.39 Effective compliance in axial fiber direction S_{3333} in assumption 1

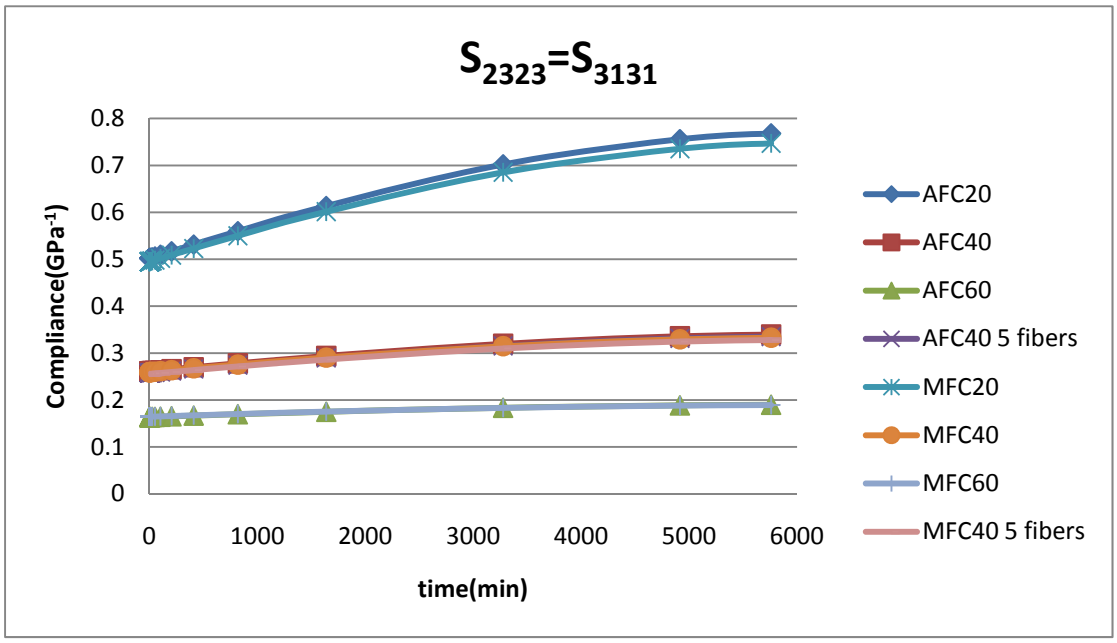

Fig. 3.40 Effective shear compliance S_{2323} in assumption 1

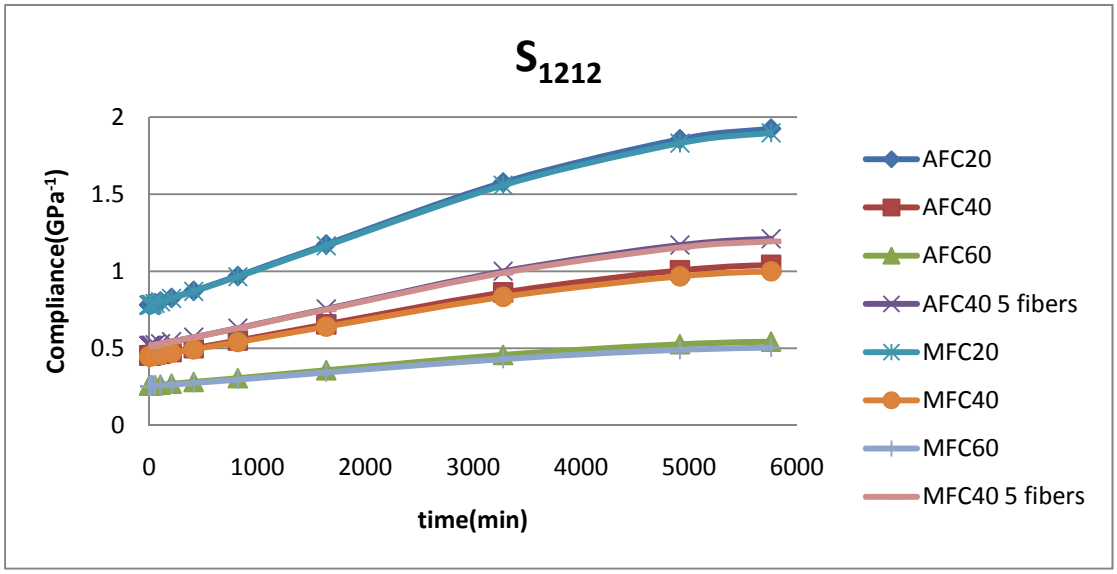

Fig. 3.41 Effective shear compliance S_{1212} in assumption 1

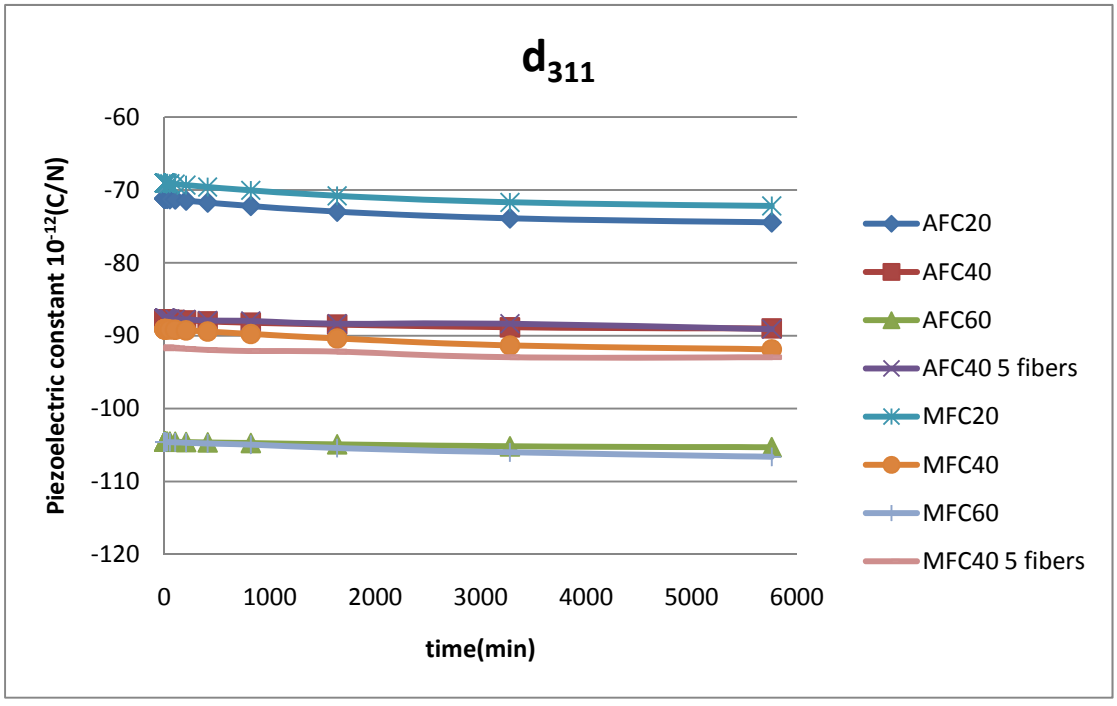

Fig. 3.42 Effective piezoelectric constant d_{311} in assumption 1

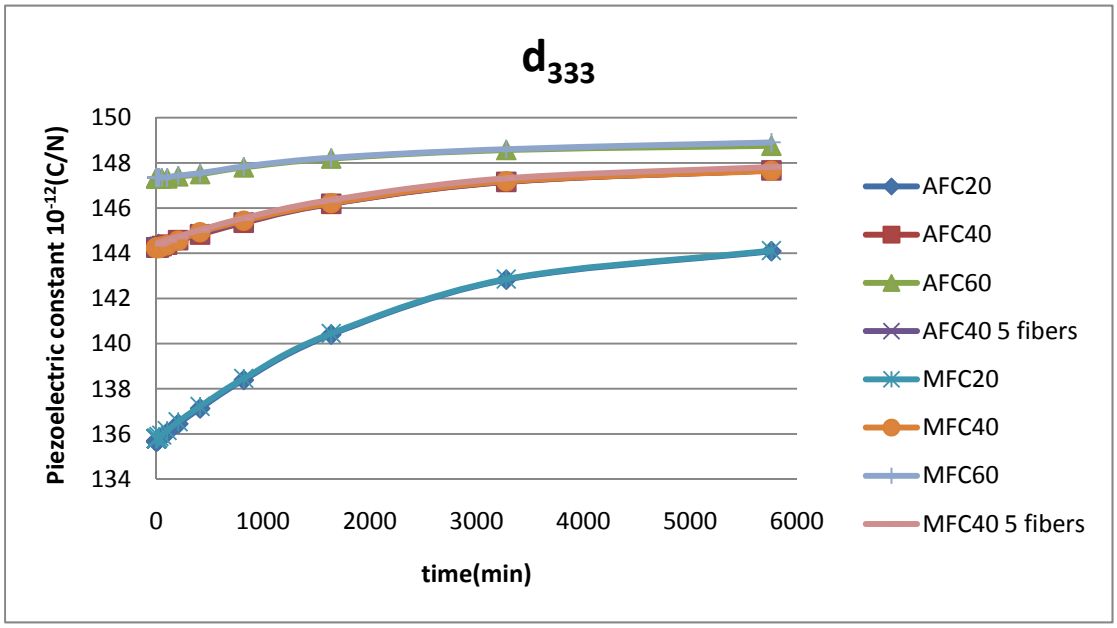

Fig. 3.43 Effective piezoelectric constant d_{333} in assumption 1

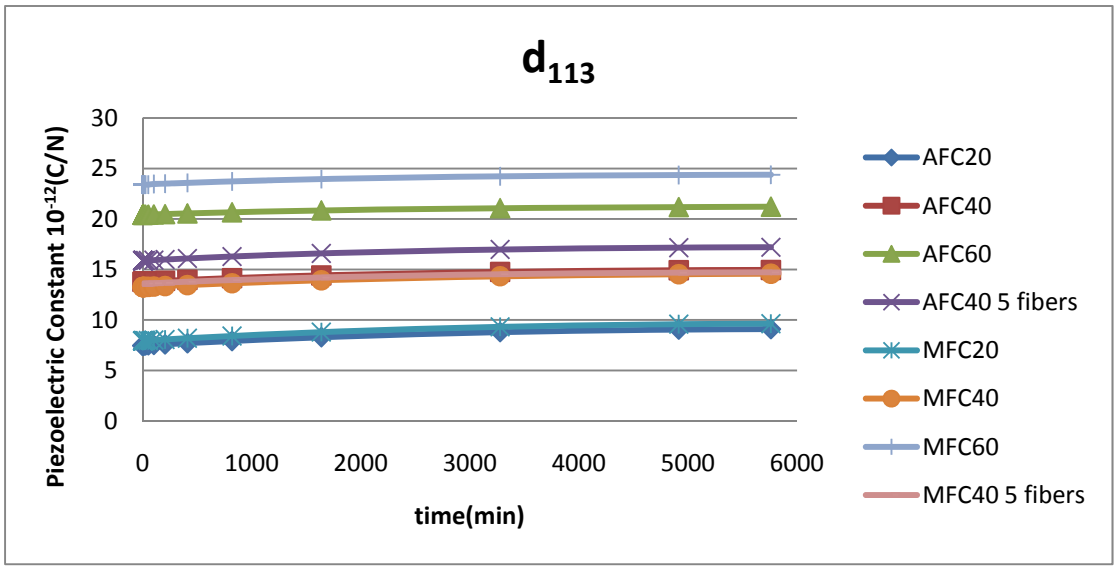

Fig. 3.44 Effective piezoelectric constant d_{113} in assumption 1

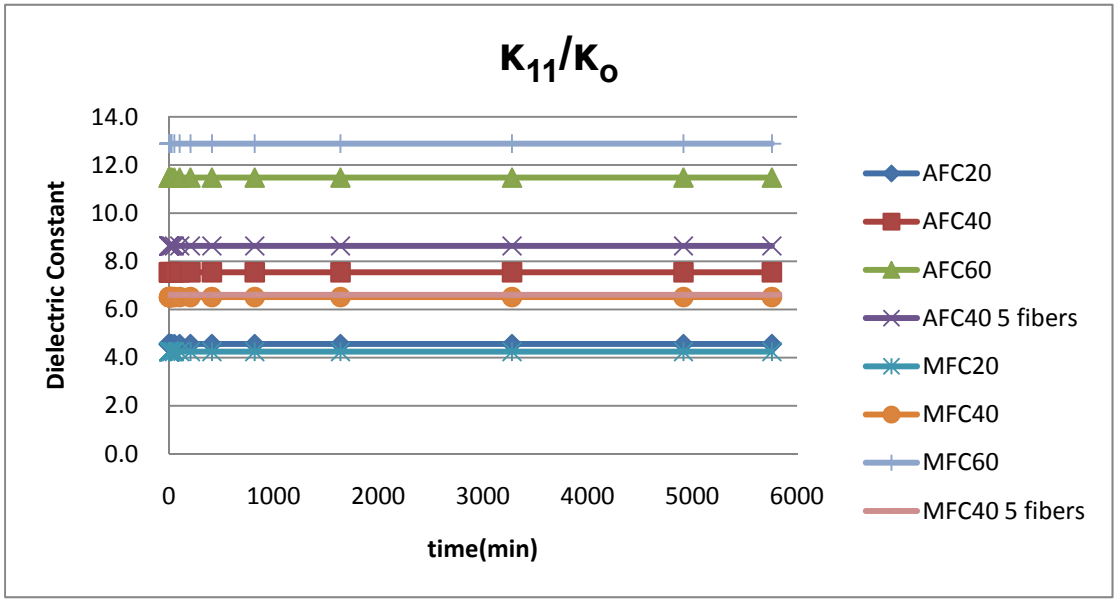

Fig. 3.45 Effective relative permittivity in transverse direction κ_{11}/κ_o in assumption 1

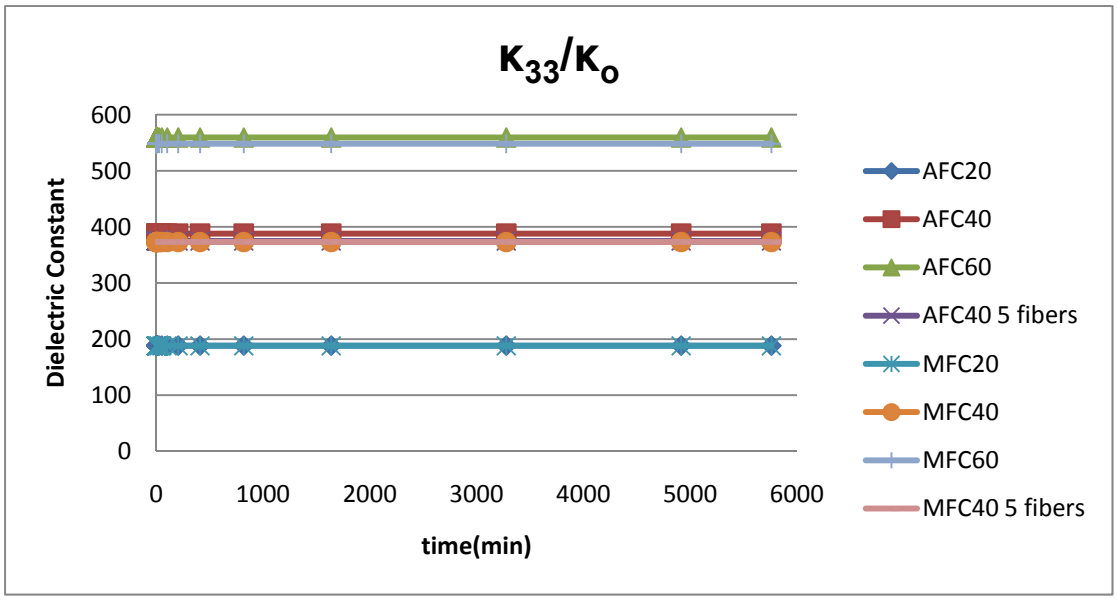

Fig. 3.46 Effective relative permittivity in axial fiber direction κ_{33}/κ_o in assumption 1

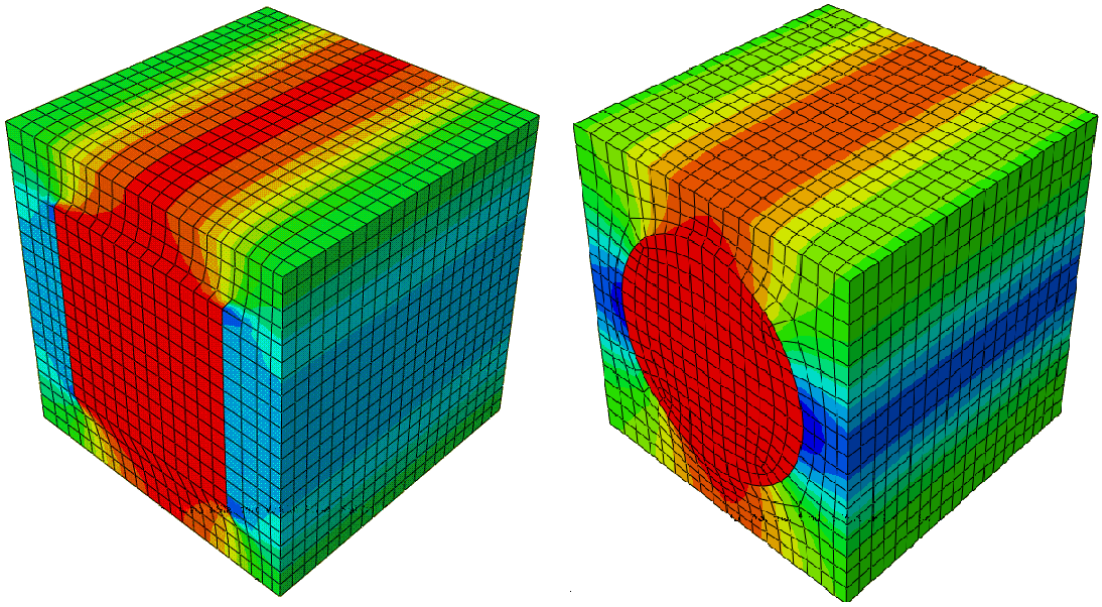

Fig. 3.47 The electrical field in FE model in d_{113} boundary conditions

Results from the assumption 2

Figure 3.48 presents the transverse compliance S_{1111}. Figure 3.49 presents the longitudinal compliance S_{3333}. Similar observations as in the assumption 1 are seen. Fig. 3.50 presents the shear compliance S_{3131}=S_{2323}. The creeps in composites at 20% fiber volume fractions are more significant than those at 40% and 60% fiber volume fractions. Fig. 3.51 presents the shear compliance S_{1212}. Comparing the compliances in the assumption 2 with the compliances in the assumption 1, we find that the value of the compliances, S_{1111}, S_{3333}, S_{3131}, and S_{1212} remain unchanged. It is due to the elastic properties that we applied in both assumptions are constant. The mechanical properties of PZT-7A at high temperature is not available and PZT ceramic has high stiffness so we neglect the temperature dependent elastic properties for the PZT-7A.

Figures 3.52 and 3.53 present piezoelectric constant d_{311} and d_{333}, respectively. The piezoelectric constant in composites at low fiber volume fractions changes more significantly than those at high fiber volume fraction. Fig. 3.54 presents piezoelectric constant d_{113}. Comparing the piezoelectric constants in both assumptions, we find that the value of d_{311} and d_{333} in the assumption 2 are larger than the values in the assumption 1, and the value of d_{113} in the assumption 2 are similar to that in the assumption 1. In the assumption 2, all of the piezoelectric constants increase proportionally to the piezoelectric constant d_{311}, which show significant increase in the effective piezoelectric constants of the AFC and MFC. However, the values of piezoelectric constant d_{113} in the two assumptions are almost the same. Similar observations are shown in Fig. 3.20, 3.45 and 3.55 for the dielectric constant κ_{11}/κ_o.

Fig. 3.55 presents the transverse dielectric constant κ_{11}/κ_o, which is almost constant during the time-dependent analysis. Fig. 3.56 presents longitudinal dielectric constant κ_{33}/κ_o. Comparing the dielectric constants in both assumptions, the value of κ_{33}/κ_o in the assumption 2 are smaller than the value in the assumption 1, and the value of κ_{11}/κ_o in the assumption 2 are the same as the value in the assumption 1.

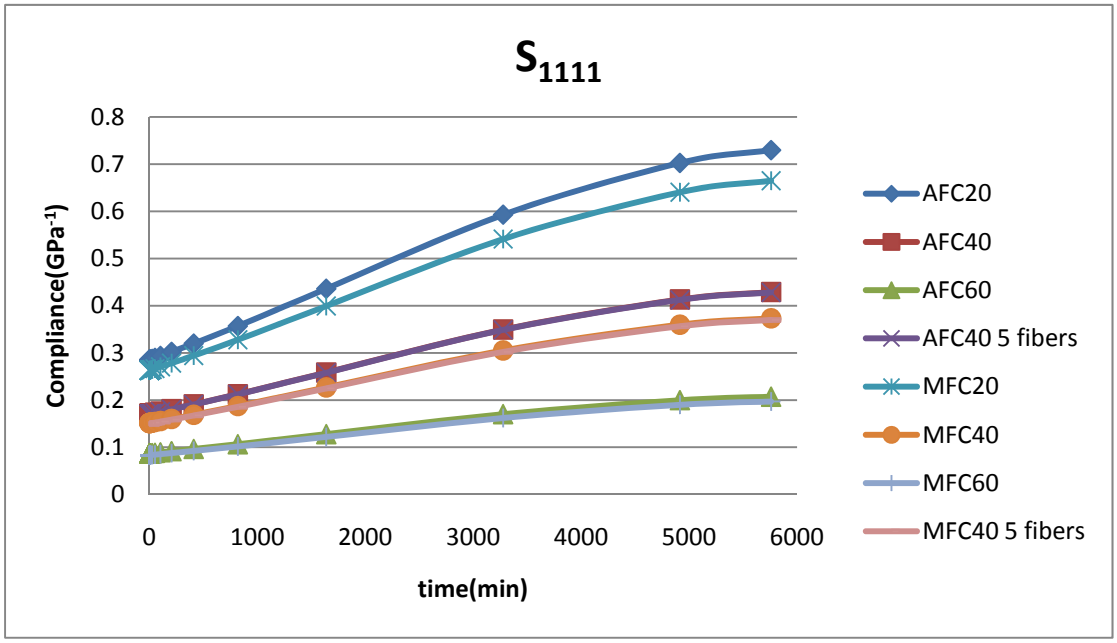

Fig. 3.48 Effective compliance in transverse direction S_{1111} in assumption 2

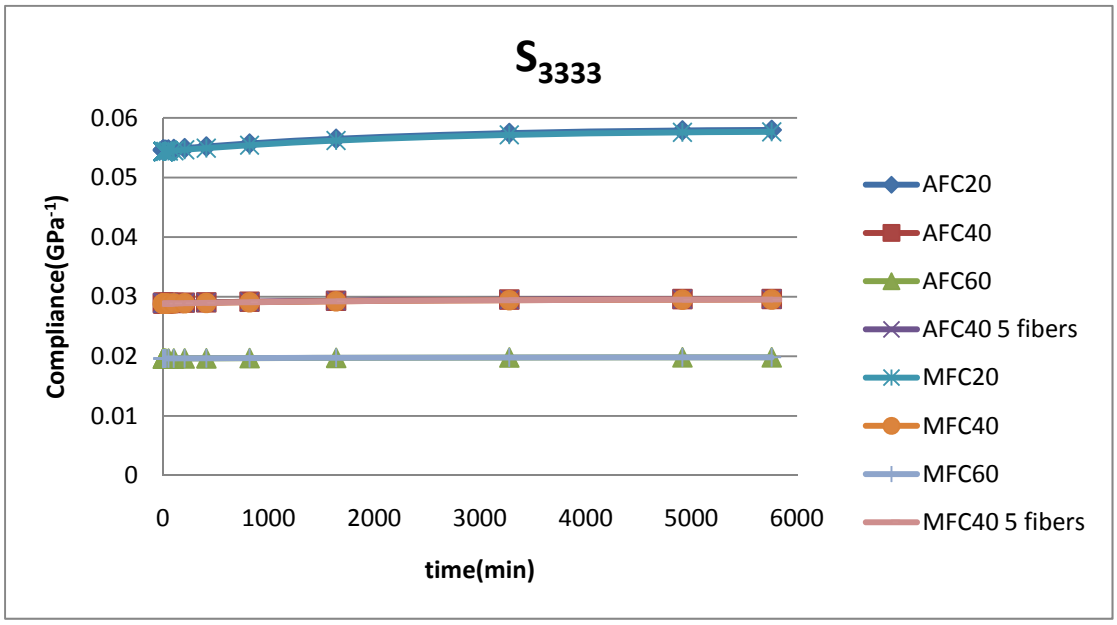

Fig. 3.49 Effective compliance in axial fiber direction S_{3333} in assumption 2

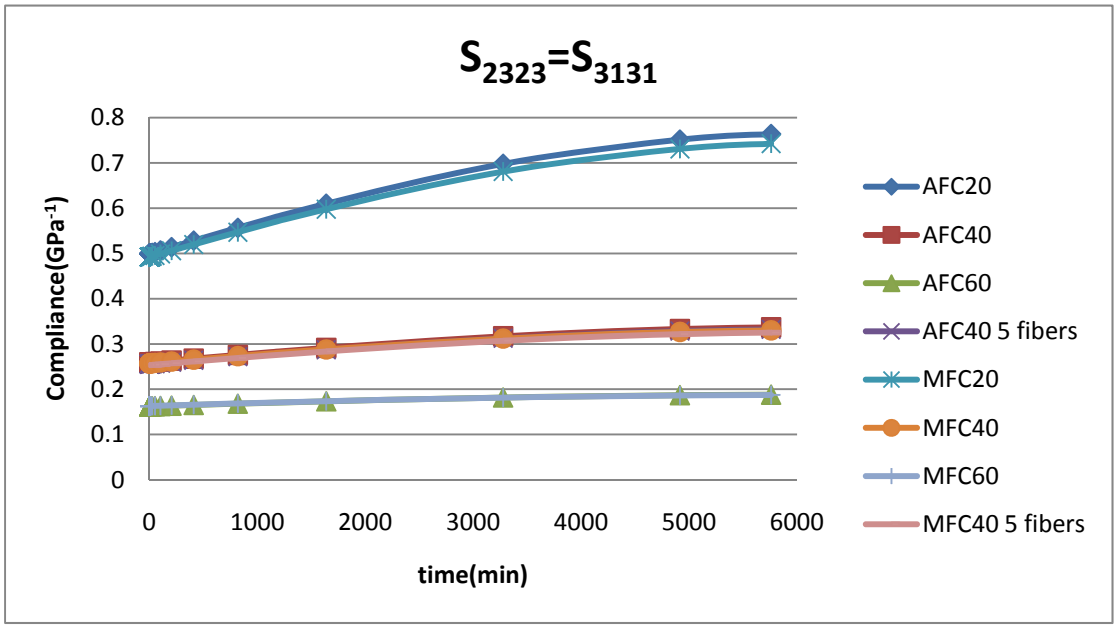

Fig. 3.50 Effective shear compliance S_{2323} in assumption 2

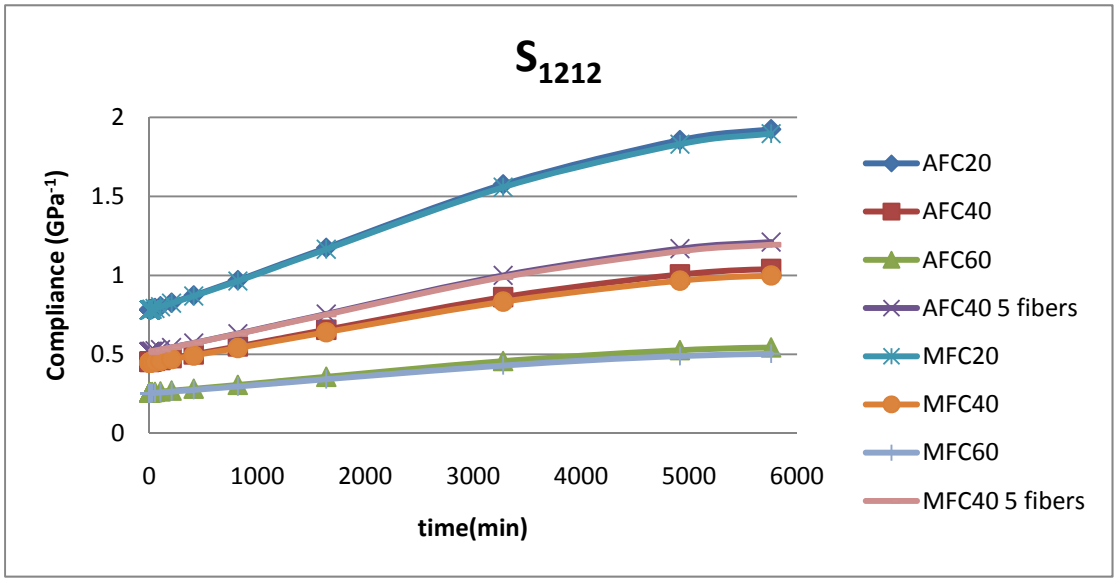

Fig. 3.51 Effective shear compliance S_{1212} in assumption 2

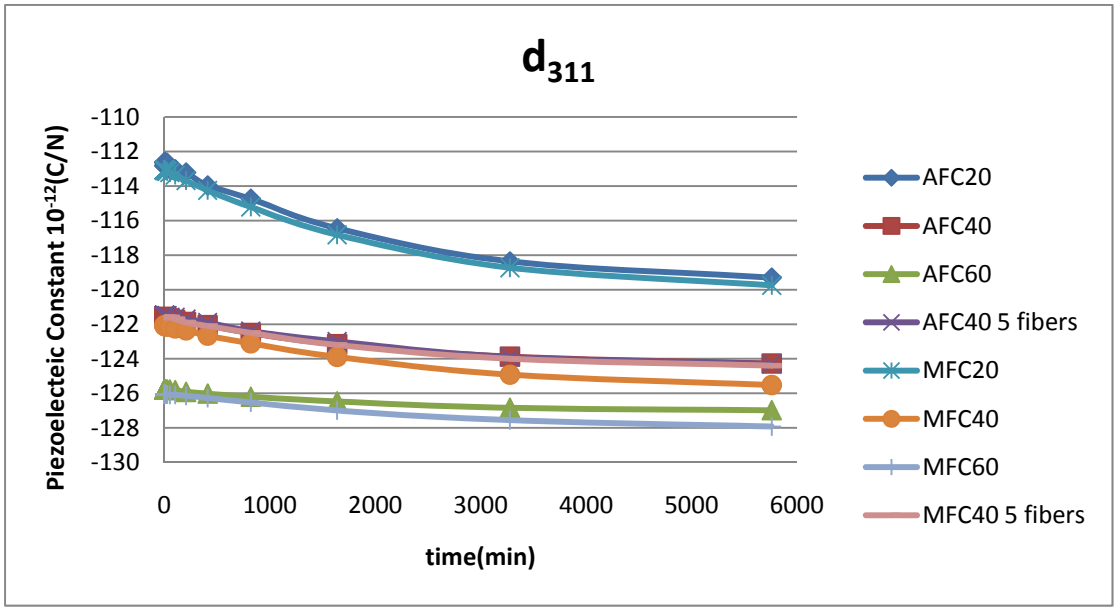

Fig. 3.52 Effective piezoelectric constant d_{311} in assumption 2

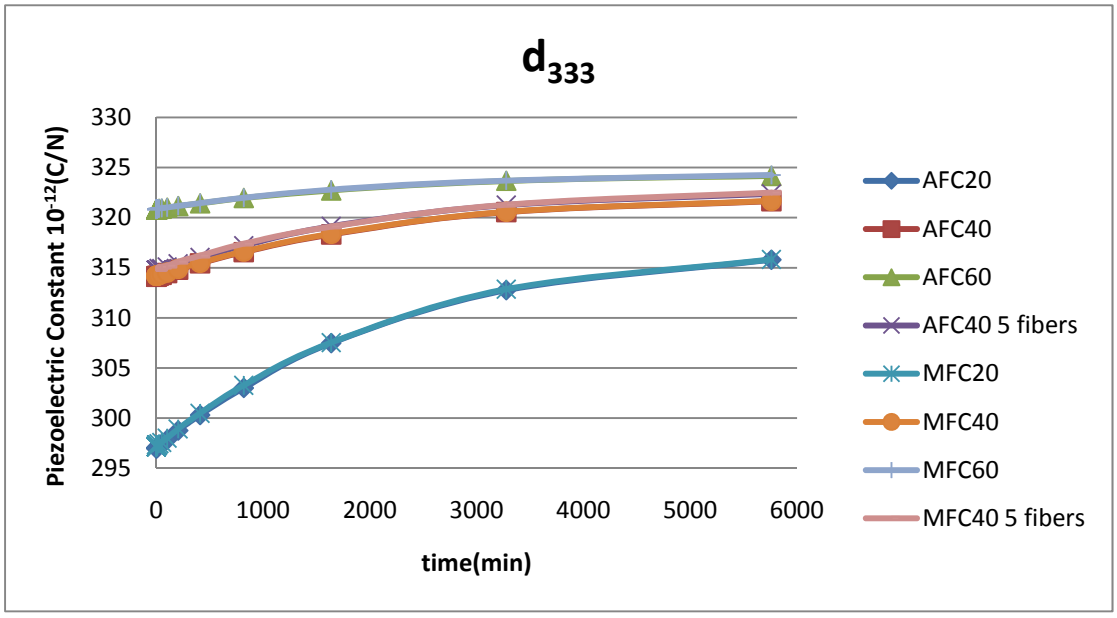

Fig. 3.53 Effective piezoelectric constant d_{333} in assumption 2

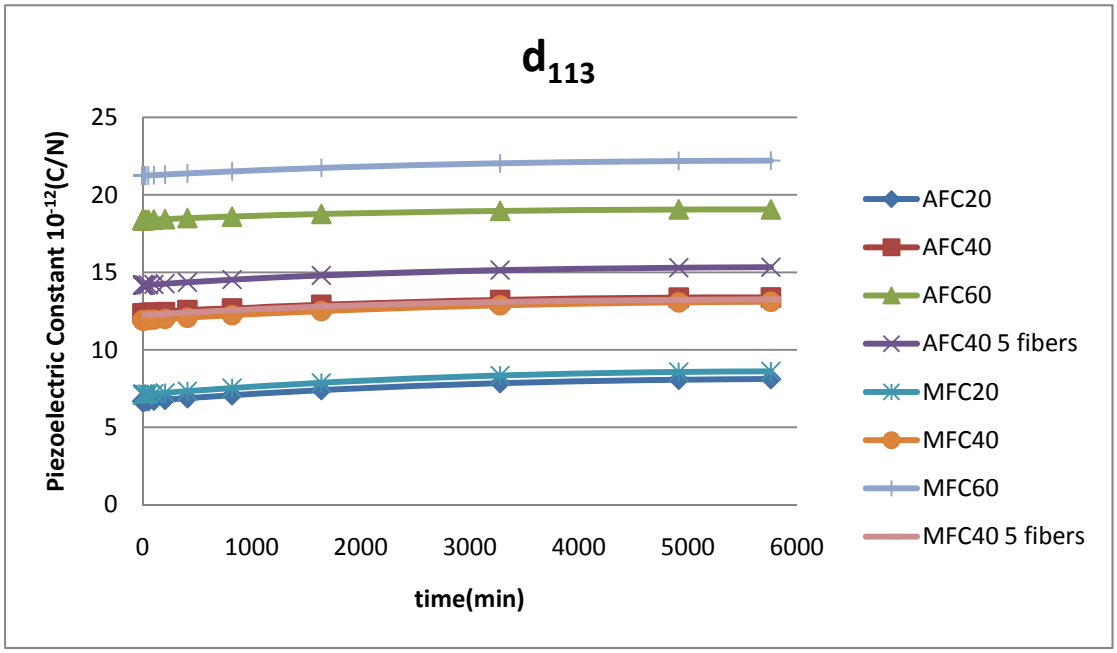

Fig. 3.54 Effective piezoelectric constant d_{113} in assumption 2

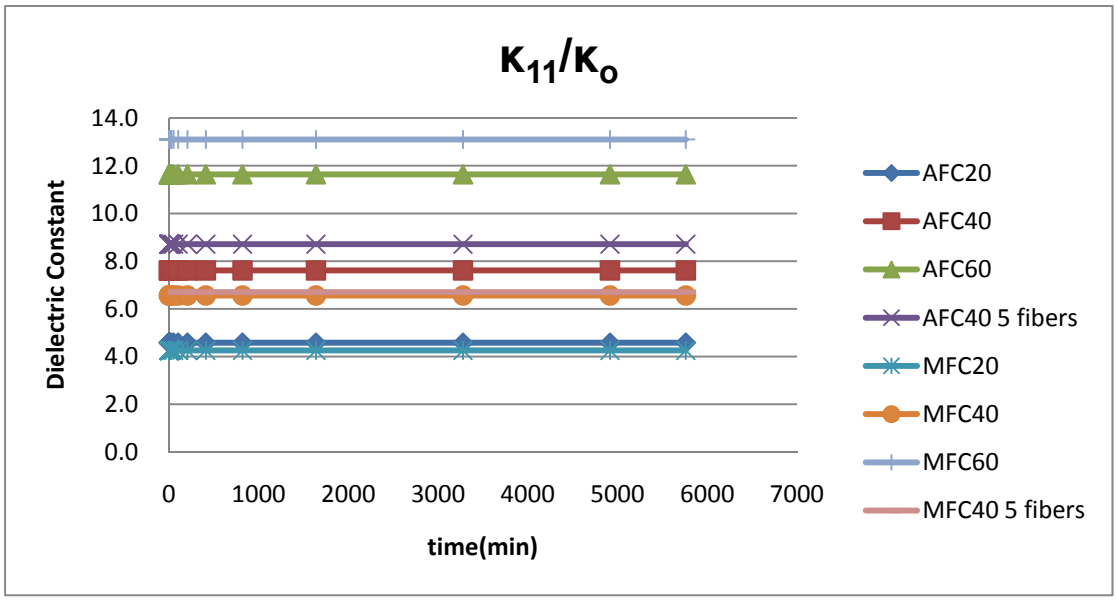

Fig. 3.55 Effective relative permittivity in transverse direction κ_{11}/κ_o in assumption2

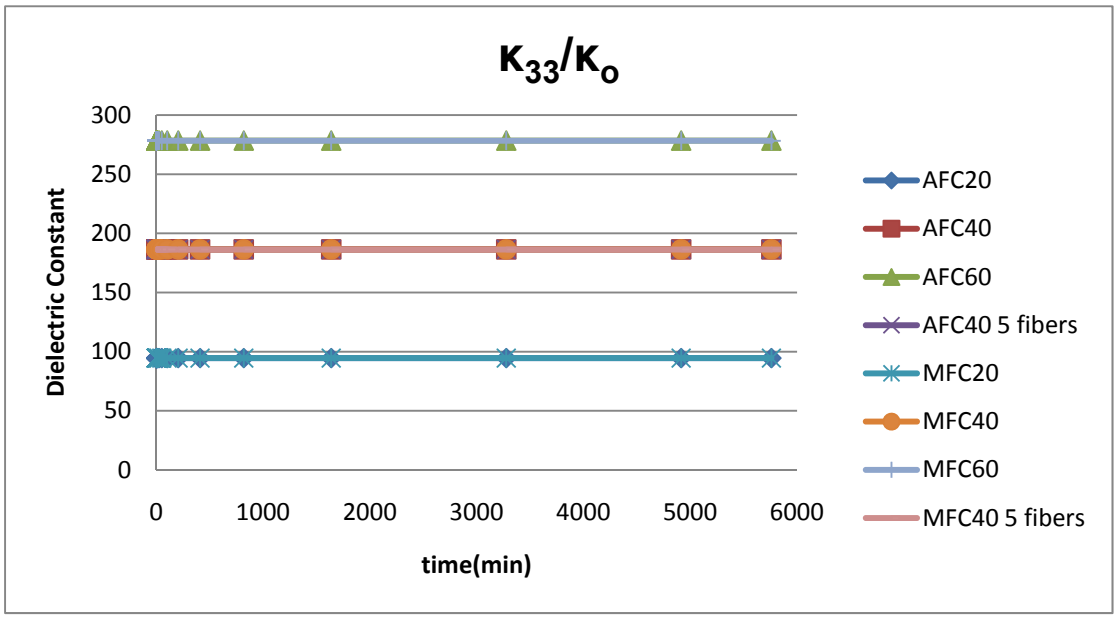

Fig. 3.56 Effective relative permittivity in axial fiber direction κ_{33}/κ_o in assumption 2

For above results, we use type S piezoelectricity to perform the simulation. We now use the type E piezoelectricity to characterize the piezoelectric constant d_{333} for composites with 40% fiber volume fraction. The differences between the type S and the type E are in the input material properties and piezoelectric functions. The input piezoelectric constant of the type S is e_{ijk} and the electro-mechanical functions are given in Eq. 2.15 and Eq. 2.16. The input piezoelectric constant of the type E is d_{ijk} and the piezoelectric functions are given in Eq. 2.13 and Eq. 2.14. Both AFC and MFC models are examined. The results are presented in Fig. 3.57 and 3.58. Comparing these results with Fig. 3.43 and Fig. 3.53, we find that the results are compatible.

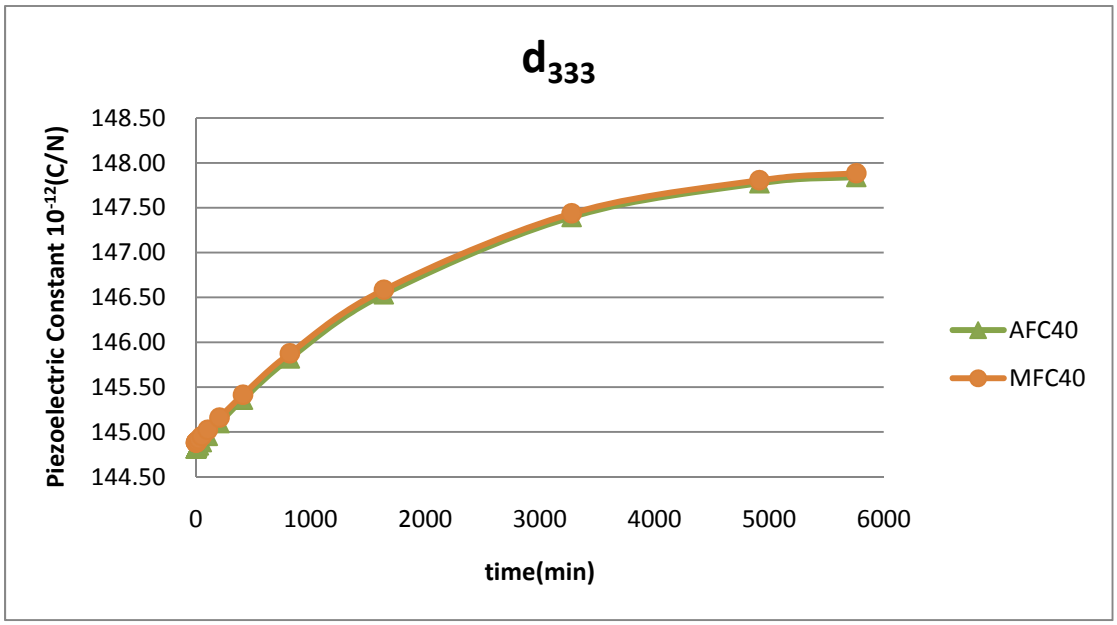

Fig. 3.57 Effective Piezoelectric constant d_{333} for checking assumption1

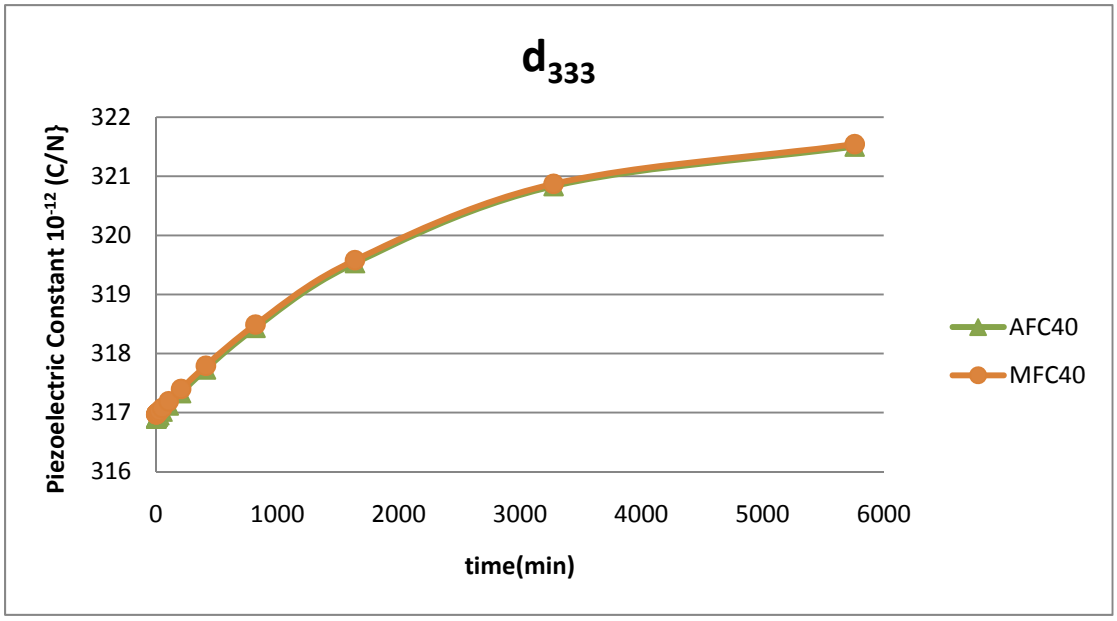

Fig. 3.58 Effective Piezoelectric constant d_{333} for checking assumption 2

Form Chapter II, we know that the piezoelectric ceramics could also experience time-dependent compliance and piezoelectric constant. Here, we assume the elastic modulus and piezoelectric constant of PZT change with time and examine the responses of the effective compliance S_{3333} and d_{333}. The input properties of ABAQUS are Y_{33} and e_{333}. In Chapter II, the compliance creeps 100% so we assume the modulus E_{33} relaxes 50%. The piezoelectric constant is reported in Chapter II. The time-dependent modulus and piezoelectric constant for the PZT-7A are given in Eq. 3.26. The responses of S_{3333} and d_{333} are presented in Fig. 3.59 and Fig. 3.60. It is seen that more pronounced time-dependent responses are observed.

$$Y_{33} = 81.886(0.5 + 0.5e^{-0.00002t})$$

$$e_{333} = 23.4 + 23.4t^{0.0498} \tag{3.26}$$

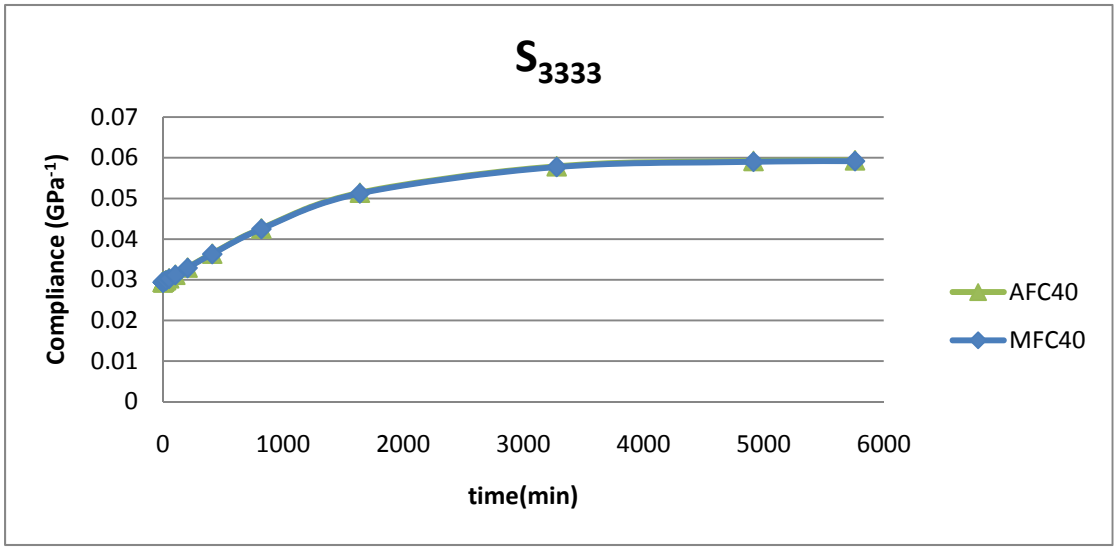

Fig. 3.59 Effective compliance S_{3333}

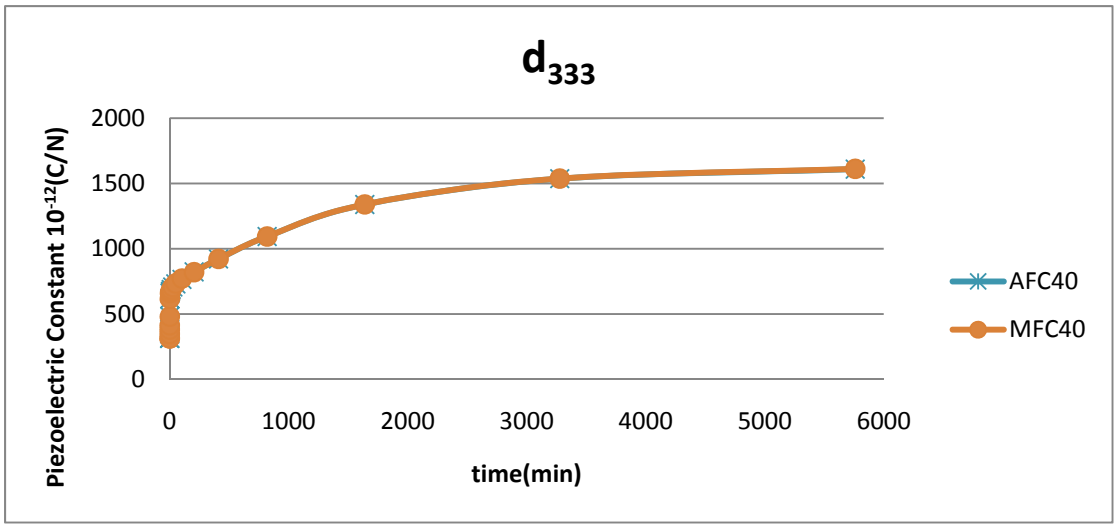

Fig. 3.60 Effective Piezoelectric constant d_{333}

CHAPTER IV
CONCLUSIONS AND FURTHER RESEARCH

4.1 DISCUSSIONS

From this study, we investigated the time-dependent and long-term responses of piezoelectric fiber composites due to the existence of viscoelastic matrix. PFCs are generally used as sensors and actuators that can be exposed to various loading conditions, i.e., statics and dynamics, and several time scales, i.e., short- and long terms and different frequencies. For example, as actuators for controlling vibrations in the host structures (Fig. 4.1 depicts a sinusoidal displacement of the host structure), an electric charge can be applied to the PFCs to suppress the vibrations by generating a counter displacement (Fig. 4.2). When the time-dependent effect of the PFC is negligible, we can apply an oscillation charge with the same frequency as the vibrating host structures to suppress the vibration. However, when the PFCs show pronounced time-dependent effects due to the viscoelastic matrix applying charge with the same frequency as the host structure may result in expected performance only at early time but as time progress, the time-dependence in the electro mechanical responses of the PFC lead to different output frequencies. This might lead to false counter displacement (Fig. 4.3), which is due to the phase-lag characteristic of the viscoelastic PFCs. Only when steady state (equilibrium/ related) condition is achieved in the PFC, the output displacement and the input charge have the same frequency. Thus, when a constant frequency is applied to PFCs to suppress oscillation displacement in the host structure, the pronounced time-dependent effect on the PFCs can amplify the displacement (Fig. 4.4) at later time. In practice, the PFCs

might need to operate for duration longer than 2 hours (e.g. controlling vibrations in helicopter blades or other components). Under these conditions, the PFC will be constantly loaded for a long period generating heat and raising the temperatures. The viscoelastic behaviors will become pronounced in PFC and the time-dependent effect will affect the control performance. Thus, knowing long-term performance of the PFCs could significantly improve the control performance. The existence of time-dependent (viscoelastic) effect in the PFCs makes the responses of the PFCs sensitive to rate of loading.

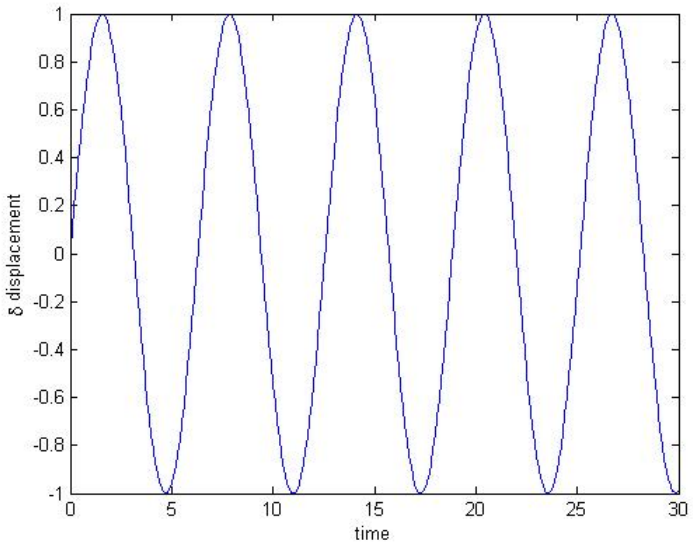

Fig. 4.1 Displacement history of a host structure

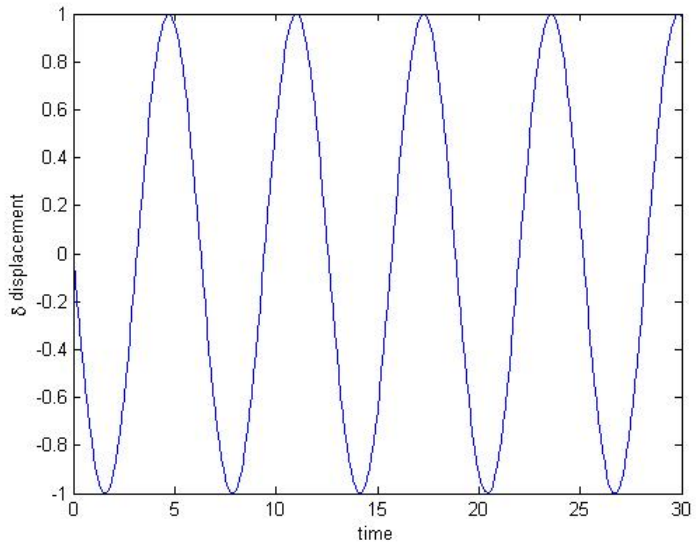

Fig. 4.2 Counter displacement to minimize vibration in the host structure

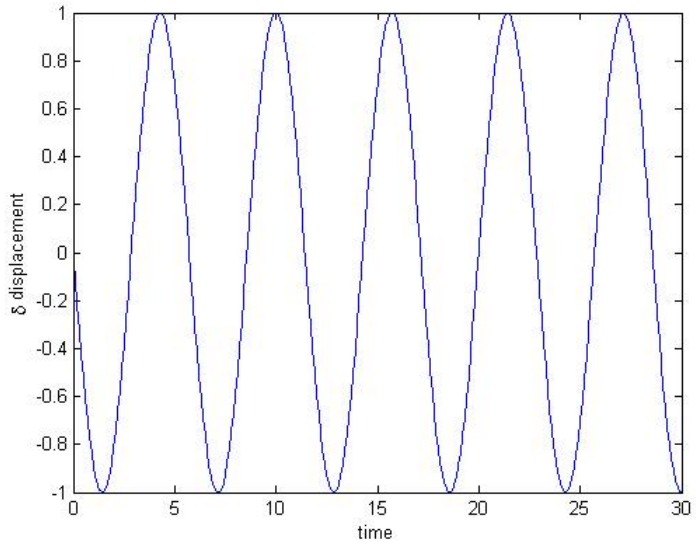

Fig. 4.3 The phase lagging response in the actuator

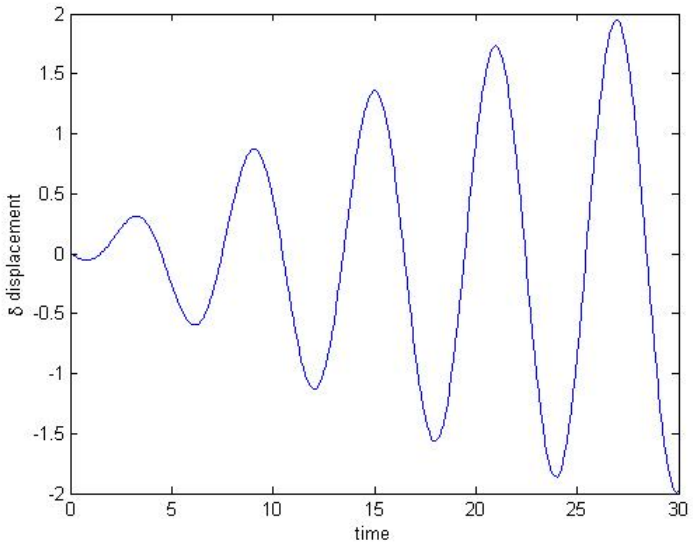

Fig. 4.4 Time-dependent result of suppression

Moreover, integrating the PFCs to the host structures would subject the PFCs under constant stress. Generally, we use adhesive to bond the PFCs to the host structure that could lead to high stress concentrations near the interphase. Take a cantilever beam having 4 PFCs (Fig. 4.5). Fig 4.6 presented the beam under bending that the localized stresses occur at interphase regions as identified by circles in Fig. 4.6. The time-dependent effects in the PFCs could lead to continuous deformation, accelerating debonding or detachment of the PFCs from the host structures. Having information on the long-term behaviors of the PFCs would improve the maintenance of the smart structure

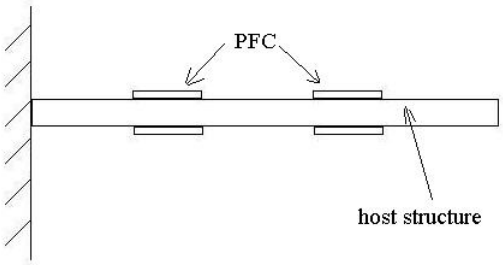

Fig. 4.5 Cantilever beam attached 4 PFCs

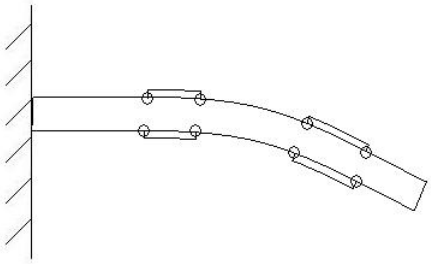

Fig. 4.6 Cantilever beam under loading

4.2 CONCLUSIONS

This study analyzes the time-dependent responses of PFCs. PFC is a piezoelectric fiber composite consisting of piezoelectric fibers, epoxy matrix, electrodes and kapton layers. There are two types of PFCs: AFC and MFC. The difference between the AFC and MFC is in the shapes and types of fibers. AFC uses circular cross-section fibers and MFC uses rectangular cross-section fibers. The epoxy matrix in the PFC could have significant viscoelastic characteristics, especially at elevated temperatures, affecting overall responses of PFCs. We established micromechanical models for PFCs using FE. We made several assumptions in generating the micromechanical models. The electrodes

and kapton layers are ignored since the sizes of the electrodes and kapton layers are much smaller than those of the epoxy regions and piezoelectric fibers. Thus, the electric fields are assumed uniformly distributed throughout the fiber longitudinal axis. We assumed that fibers are uniformly distributed in the matrix medium. Micromechanical models having one fiber placed at the center of the matrix medium are generated for the AFC and MFC. In addition, we also generated micromechanical models with five fibers placed in the matrix medium.

Linearized constitutive models for piezoelectric materials that include time-dependent effects have been formulated. A general time-integral function is applied for the mechanical, electrical, and piezoelectric constants. Relaxation functions are chosen for the modulus and dielectric constant, while creep function is used for the piezoelectric constant. Parametric studies have been performed by applying different histories of stress and electric fields. It has been observed that the time-dependent effect could significantly influence overall performance of piezoelectric materials especially when histories of loadings are applied for sufficiently longer period.

The micromechanical models are generated using FE software, “ABAQUS” with an electrical element C3D8E. Three different fiber volume fractions have been considered to predict the electro-mechanical and piezoelectric properties of the AFC and MFC. Predictions were compared with the analytical solutions and experimental data, which were available in the literature. Comparing to the analytical results, our predictions are compatible in the elastic modulus, piezoelectric constants and dielectric constants along the fiber longitudinal axis. Some mismatches are observed in the transverse and

shear properties especially at high fiber contents. Thus, it is concluded that properties in the longitudinal fiber directions depend only on the compositions and properties of the constituents, while the transverse and shear properties depend also on the microstructural arrangements. Predictions of the AFC and MFC models are comparable to the available experimental data. The five fiber model shows lower shear modulus than the single fiber model because in the five fibers model shearing between fibers can be incorporated increasing deformation in the PFCs. The MFC model shows higher transverse modulus E_{11} than the AFC because the rectangular fibers show higher resistant to local deformation in the matrix close to the interphase regions than in the circular fibers.

PFCs are often utilized for applications at high mechanical loading and electric field. Under such conditions, significant amount of heat could be generated increasing temperatures. At elevated temperatures, materials could experience significant time-dependent behaviors. The effects of viscoelectric matrix on the overall properties of PFCs have been studied using the FE micromechanical models. PFCs which have larger fiber volume fractions show less significant time-dependent behaviors. It is also seen that the transverse and shear properties exhibited more pronounced time-dependent responses compared to the longitudinal (axial) properties.

4.3 FURTHER RESEARCH

The current study can be extended as follows:

1) FE micromodels can be refined to also include the electrode fingers and kapton layers, allowing to study the effects of electrode spacing and nonuniform distribution of the electric fields on the overall performance of PFCs.
2) The predictions of the time-dependent electro-mechanical properties need to be compared to experimental data. Thus, we need to perform time-dependent electro-mechanical test, at elevated temperatures, on the PFCs.
3) To enhance, the capability of the FE models in predicting creep compliance, which is the limitation of the USFLD, user element (UEL) subroutine can be developed.

REFERENCES

[1] Fukada E, History and Recent Progress in Piezoelectric Polymers, IEEE Transactions on Ultrasonics, Ferroelectrics, and Frequency Control; 2000, 47(6), p. 1277-1290

[2] Bent AA, Active Fiber Composites for structural actuation, Ph. D dissertation M.I.T., Cambridge, M A, 1994

[3] Nelsion LJ, Bowen CR, Stevens R, Cain M, Stewart M, Modelling and measurement of piezoelectric fibers and interdigitated electrodes for the optimization of piezofibre composites, Proc. of SPIE; 2003, 5053, p. 556-567

[4] Wickramasinghe KV and Hagood NW, Material characterization of active fiber composites for integral twist-actuated rotor blade application, Smart Mater. Struct.; 2004,13, p. 1155–1165

[5] Wickramasinghe KV and Hagood NW, Durability Characterization of Active Fiber Composite Actuators for Helicopter Rotor Blade Applications, Journal Of Aircraft; 2004, 41(4), p. 931-937

[6] Melnykowycz1 M, Kornmann X, Huber C, Barbezat M and Brunner AJ, Performance of integrated active fiber composites in fiber reinforced epoxy laminates, Smart Mater. Struct.; 2006, 15, p. 204–212

[7] Williams RB, Inman DJ and Wilkie WK, Temperature-Dependent Thermoelastic Properties For Macro Fiber Composite Actuators, Journal of Thermal Stresses; 2004, 27, p. 903-915

[8] Azzouz MS, Mei C, Bevan JS, and Ro JJ, Finite Element Modeling of MFC/AFC Actuators and Performance of MFC, Journal of Intelligent Material Systems and Structures; 2001, 12(9), p. 601-612

[9] Sodano HA, Macro-Fiber Composites for Sensing, Actuation and Power Generation, M.S. dissertation, Virginia Polytechnic Institute and State University, Blacksburg, VA

[10] Williams RB, Inman DJ, Schultz MR and Hyer MW, Nonlinear Tensile and Shear Behavior of Macro Fiber Composite Actuators, Journal of Composite Materials; 2003, 38(10), p. 855-869

[11] Williams RB, Inman DJ and Wilkie WK, Nonlinear Response of the Macro Fiber Composite Actuator to Monotonically Increasing Excitation Voltage, Journal of Intelligent Material Systems and Structures; 2006, 17, p.601-608

[12] Dano ML and Jullie`re B, Active control of thermally induced distortion in composite structures using Macro Fiber Composite actuators, Smart Mater. Struct.; 2007,16, p. 2315–2322

[13] Dano ML, Gakwaya M and Jullie`re B, Compensation of Thermally Induced Distortion in Composite Structures using Macro-fiber Composites, Journal of Intelligent Material Systems and Structures;2008, 19, p.225-233

[14] Dunn ML and Taya M, Micromechanics Predictions of the Effective Electroelastic Moduli of Piezoelectric Composites, Int. J. Solids Structures; 1993, 30(2), pp.161-175

[15] Tan P and Tong L, Micro-electromechanics models for piezoelectric -fiber-reinforced composite materials, Composites Science and Technology; 2001, 61, p. 759–769

[16] Odegard GM, Constitutive modeling of piezoelectric polymer composites, Acta Materialia; 2004, 52, p. 5315–5330

[17] Lee J, Boyd IV JG, Lagoudas DC, Effective properties of three-phase electro-magneto-elastic composites, International Journal of Engineering Science; 2005, 43, p. 790–825

[18] Aboudi J, Hysteresis behavior of ferroelectric fiber Composites, Smart Mater. Struct.; 2005, 14, p. 715–726

[19] Lin Y and Sodano HA, Concept and model of a piezoelectric structural fiber for multifunctional composites, Composites Science and Technology;2008, 68, p. 1911–1918

[20] Dunn ML and Wienecke HA, Inclusions and Inhomogeneities in Transversely Isotropic Piezoelectric Solids, lnt. J. Solids Structures; 1997, 34(27), p. 3571-3582

[21] Liu HY, Qin QH, Mai YW, Theoretical model of piezoelectric fibre pull-out, International Journal of Solids and Structures; 2003, 40, p. 5511–5519

[22] Beckert W and Kreher WS, Modelling piezoelectric modules with interdigitated electrode structures, Computational Materials Science; 2003, 26, p. 36–45

[23] Heiling C and Hardil KH, Time Dependence of Mechanical Depolarization in Ferroelectric Ceramics, Proc. ISAF'98;1998, p. 503-506

[24] Damjanovic D, Ferroelectric, dielectric and piezoelectric properties of ferroelectric thin films and ceramics, Rep. Prog. Phys.; 1998, 61, p. 1267–1324

[25] Lines ME and Glass AM, Principles & Applications of Ferroelectrics and Related Materials, Clarendon Press, Oxford; 1979

[26] Wineman AS and Rajagopal KR, Mechanical Response of Polymers: An Introduction, Cambridge University Press; 2000

[27] Manoa JF, Lopesc JL, Silvac RA and Brostowd W, Creep of PVDF monofilament sutures: service performance prediction from short-term tests, Polymer; 2003, 44, p. 4293–4300

[28] Vinogradov AM, Schmidt VH, Tuthill GF and Bohannan GW, Damping and electromechanical energy losses in the piezoelectric polymer PVDF, Mechanics of Materials;2004, 36, p. 1007–1016

[29] Fett T and Thun G, Determination of room-temperature tensile creep of PZT, Journal of material science letters; 1998, 17, p. 1929-1931

[30] Hall DA, Review Nonlinearity in Piezoelectric ceramics, Journal of Materials science; 2001, 36, p. 4575-4601

[31] Nicholson LM, Whitley KS and Gates TS, The role of molecular weight and temperature on the elastic and viscoelastic properties of a glassy thermoplastic polyimide, International Journal of Fatigue; 2002, 24, p. 185–195

VITA

Name	Kuo-An Li
Address	Department of Mechanical Engineering
	c/o Dr. Hanifan Muliana
	Texas A&M University
	College Station, TX 77843-3123
Email Address	andee058@hotmail.com
Education	B. E., Mechanical Engineering
	National Taiwan University, Taipei, Taiwan, 2004
	M. S., Mechanical Engineering
	Texas A&M University, TX, U. S. A., 2009